A SOLID-STATE VERTEX DETECTOR FOR STUDY OF THE PHOTOPRODUCTION OF HEAVY FLAVOURS

by

Steven Bradley Hancock

A thesis submitted for the degree of
Doctor of Philosophy in the University of London
and for the Diploma of Membership of Imperial College

Department of Physics
Imperial College, London
January 1984

ABSTRACT

This thesis describes the development of silicon detectors which are sensitive both to the position of and the energy deposited by incident charged particles. Performance details of various thin silicon devices are presented for several different incident particle types and multiplicities in the kinetic energy range 0.25 to 114 GeV. A study, conducted in parallel, to refine the parametrization and fitting of the ionization energy-loss distribution for a thin silicon absorber is also described.

The culmination of this work has been the design and construction of a silicon active target as part of a solid-state vertex detector intended for use in the NA14 photoproduction experiment at the CERN SPS. Some preliminary results obtained from the active target are presented.

The author has been personally involved in many aspects of the data acquisition hardware for each of the test beam experiments described in this thesis. He has also been responsible for the development of the off-line fitting procedure used both in the analysis of the data from the tests and in the calibration of the NA14 active targets.

CONTENTS

Chapter 1 INTRODUCTION

Chapter 2 A SURVEY OF SOME EXISTING AND PROPOSED EXPERIMENTS EMPLOYING SEMICONDUCTOR DETECTORS

Chapter 3 SEMICONDUCTOR DETECTORS

Chapter 4 DEVELOPMENT OF A POSITION-SENSITIVE SILICON DETECTOR

Chapter 5 REFINEMENT OF AN IEL FITTING ROUTINE

Chapter 6 THE NA14 ACTIVE TARGET

FIGURES

TABLES

Chapter 1

INTRODUCTION

1.1 Historical Background

The continued discovery throughout the 1950's and 1960's of more and more "elementary" particles belonging to the hadron family cast serious doubt on whether they were indeed elementary entities. In an obvious attempt to derive some order from the chaos, particles with similar properties were organized into smaller groups or "multiplets". Thus, for example, the proton and neutron compose a doublet; both are considered to be manifestations of a single state of matter: the nucleon.

In 1962 a grander order was revealed when such isospin multiplets were combined in supermultiplets according to a scheme proposed independently by Murray Gell-Mann and Yuval Ne'eman. This classification of hadrons into supermultiplets involves a dimensionality of eight and, after an aphorism attributed to Buddha [1], was termed the "eightfold way" [2]. Its mathematical basis is in a branch of group theory invented in the nineteenth century by the Norwegian mathematician Sophus Lie. The Lie group that generates the eightfold way is SU(3). The theory requires that all hadrons belong to families corresponding to representations of the group SU(3). This gave it predictive power in analogy to the way in which Dmitri Ivanovich Mendeleev was able to predict the existence and properties of undiscovered elements from gaps in the Periodic Table, which he had constructed in 1871 to ascribe order to the plethora of atomic states. Indeed, the discovery in 1964 of the negatively-charged omega hyperon [3], the predicted isospin singlet in the baryon decuplet, proved unequivocably the validity of the SU(3) unitary symmetry scheme.

The introduction of the new system led directly to the quark hypothesis of the composite nature of hadrons. In 1964 Gell-Mann [4] and George Zweig [5] independently proposed that the aesthetically satisfying economy of the supermultiplets could be understood if all hadrons were constructed from more fundamental constituents, which Gell-Mann named "quarks" after an enigmatic line from James Joyce's "Finnegans Wake" [6]. The quarks belong to the simplest non-trivial family of the eightfold way, a family of three. By constructing baryons as combinations of three quarks and mesons as quark-antiquark pairs, it was possible to account for all of the hadrons which had been observed at that time in terms of these three different quark types or "flavours". Furthermore, every such allowed combination of quarks yielded a known particle and since, of the many possible representations of SU(3), only the singlet, octet and decuplet representations are reflected in the families of particles found in nature, it could also be inferred that no other assemblage of quarks is allowed.

Direct evidence of the internal structure of hadrons came in 1968 with the measurement of the distribution of high-energy electrons scattered off protons in an experiment performed at the Stanford Linear Accelerator Centre (SLAC). It was found that the electrons were scattered with large momentum transfers more often than could be explained without the existence of discrete scattering centres within the proton [7]. These discrete constituents were named "partons" and it was natural to associate them with the hypothetical quarks. The method of their discovery at SLAC is analogous to the famous Geiger-Marsden experiment, performed in 1911 at the suggestion of Ernest Rutherford, in which the nucleus was resolved inside the atom using fast alpha particles as a probe.

A substantial theoretical argument for the existence of a fourth quark was made in 1970 by Sheldon Lee Glashow, John Iliopoulos and Luciano Maiani [8]. The new, "charmed" quark was proposed in order to explain the observed suppression of certain weak interactions, the so-called strangeness-changing neutral current interactions. In the three-quark model there was no obvious connection between charge transfer and strangeness changing. The addition of a fourth quark in close association with the existing strange quark does not directly impede the interactions which change strangeness without transferring charge. Instead it provides an alternative channel for those interactions, but in such a way that the effects of the two channels cancel. The first evidence for charm emerged in 1974 when Samuel Ting of the Brookhaven National Laboratory [9] and Burton Richter of SLAC [10] simultaneously announced the discovery of the psi meson. The psi has an anomalously long lifetime and was interpreted as a bound state of charm and anti-charm. The existence of a fourth quark was confirmed by the discovery of charmed hadrons in 1976 in the Mark I magnetic detector at the SPEAR electron-positron collider at SLAC [11][12].

There was now an appealing symmetry between the four quark flavours and the two pairs of known leptons. The leptons appear to have many properties in common with those manifested by quarks in deep inelastic phenomena. So much so that the discovery in 1977 of the heavy tau lepton [13] suggested the existence of a further doublet of quarks. The existence of one of these quarks, the so-called "beauty" quark, is believed to have been proven by the discovery in 1977 of the upsilon meson [14], which has been interpreted as a bound state of beauty and anti-beauty. The discovery of the sixth quark is now confidently predicted.

Today, much experimental effort is devoted to the study of the strong interactions of sub-atomic particles. Evidence is growing to support the view that such interactions can be described within the framework of quantum chromodynamics (QCD), a quantum field theory in which hadrons are constructed from a limited number of quark flavours.

1.2 Photon Hard Scattering and the Photoproduction of Charm

Interest in the study of short-distance (large transverse momentum, p_T) phenomena initiated by photons is largely due to the fact that, unlike a hadron, the photon can couple directly in a point-like manner to a quark. Since its energy does not have to be shared amongst constituent quarks, the photon is a more efficient and well-understood probe for investigating the structure of hadrons to test the predictions of QCD. Particular physics motivation for photon studies derives from the photoproduction of heavy flavours. Charm production mechanisms have been the subject of theoretical debate ever since the discovery of the psi meson. The photoproduction of states containing the charmed quark is of especial interest because a description of this mechanism requires a knowledge of the structure of not only the target particle, but also that of the incident photon.

From the currently popular viewpoint the photon has three components. The most fundamental of the lowest order diagrams in which the photon displays a point-like behaviour are shown in figure 1.1. In each of these the photon couples directly to a quark of the target nucleon, leading to a final state containing no beam fragments. Figure 1.1(a) is the purely quantum electrodynamic (QED) process of deep inelastic Compton scattering. The QCD Compton process (see figure 1.1(b)) is identical except that the final state photon is replaced by a gluon, the mediator of the strong force

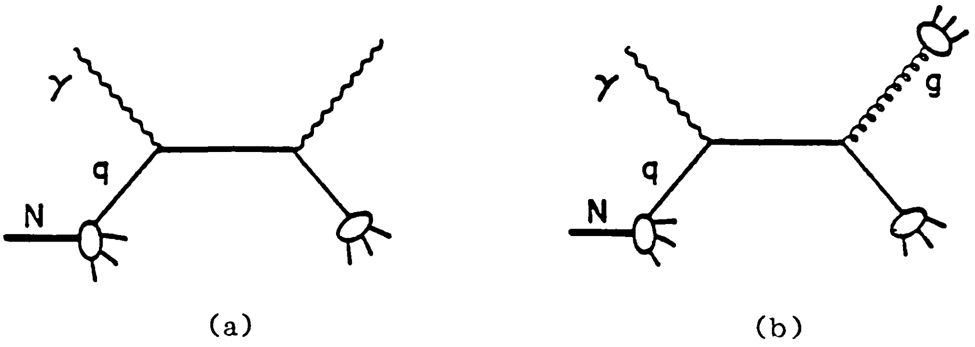

(a) (b)

Figure 1.1

and analogous to the photon of QED. In addition to its point-like component, the photon can materialize - albeit virtually - into a quark-antiquark pair before it interacts. This form of the photon has two components:

(i) An "anomalous" component, where the photon acts as a composite object but with a structure function which is harder than that of an ordinary hadron. In this component the quark-antiquark pair do not interact with each other before the interaction with the target quark (see figure 1.2(a)). It is exactly calculable in QCD [15][16].

(ii) A "VMD" (vector meson dominance) component, where the quark-antiquark pair are bound by multiple gluon exchange (see figure 1.2(b)). The photon thus builds up a form factor and appears as the superposition of vector mesons before it interacts via a consitutent quark.

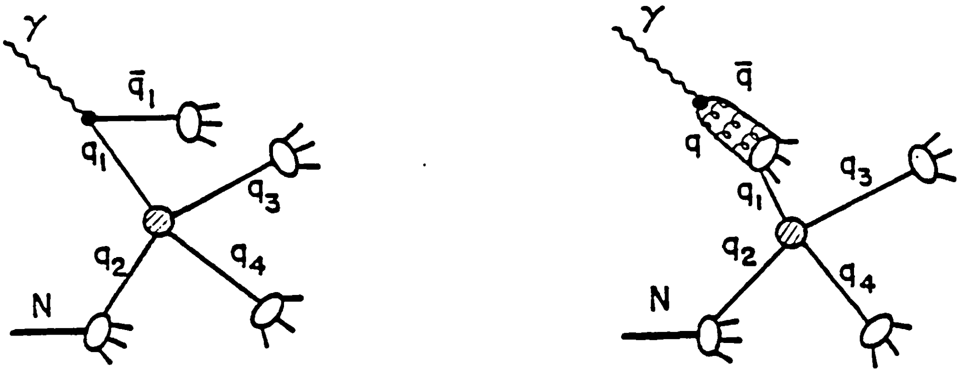

(a) (b)

Figure 1.2

The earliest models for charm photoproduction were based on the vector meson dominance description of the photon [17]. With the emergence of QCD, the dissociation of the photon into a charmed quark-antiquark pair and subsequent interaction with a valence quark of the target to produce a charmed meson was calculated [18]. This quark-quark fusion model (see figure 1.3(a)) is analogous to the basic "Drell-Yan" mechanism and arose out of the success of the parton model in describing the production of dileptons in hadronic collisions [19]. However, to lowest order in the running quark-

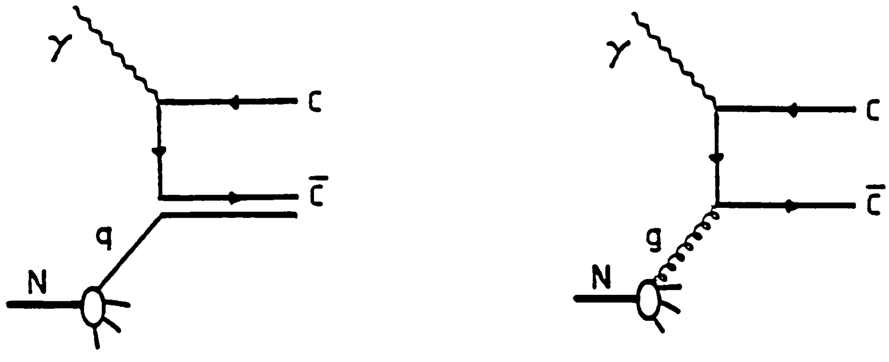

(a) (b)

Figure 1.3

gluon coupling constant, the photoproduction of charm through the "amalgamation" of the incoming photon with a target gluon constitutes the leading diagram (see figure 1.3(b)) and has attracted the most theoretical attention [20][21]. This photon-gluon fusion model is the QCD analogue of the Bethe-Heitler process by which charged lepton pairs are electromagnetically photoproduced in the Coulomb field of a nucleus. It is largely described by the top part of the diagram shown in figure 1.3(b), i.e. by the process $\gamma g \rightarrow c\bar{c}$, and this is closely related to $\gamma\gamma \rightarrow c\bar{c}$ which is calculable in QED.

1.3 The NA14 Spectrometer

The CERN experiment NA14 is run by a collaboration from Athens, CERN, College de France, Ecole Polytechnique, LAL Orsay, Imperial College, Saclay, Southampton, Strasbourg and Warsaw. The aim of the NA14 programme is to explore those properties of real photons which distinguish them from hadrons. The initial emphasis has been on the study of photon hard scattering, the manifestation of the photon's point-like or anomalous coupling which leads to large transverse momenta in the final state, but the programme also includes the study of the photoproduction of heavy flavours. The layout of the NA14 spectrometer is shown in figure 1.4.

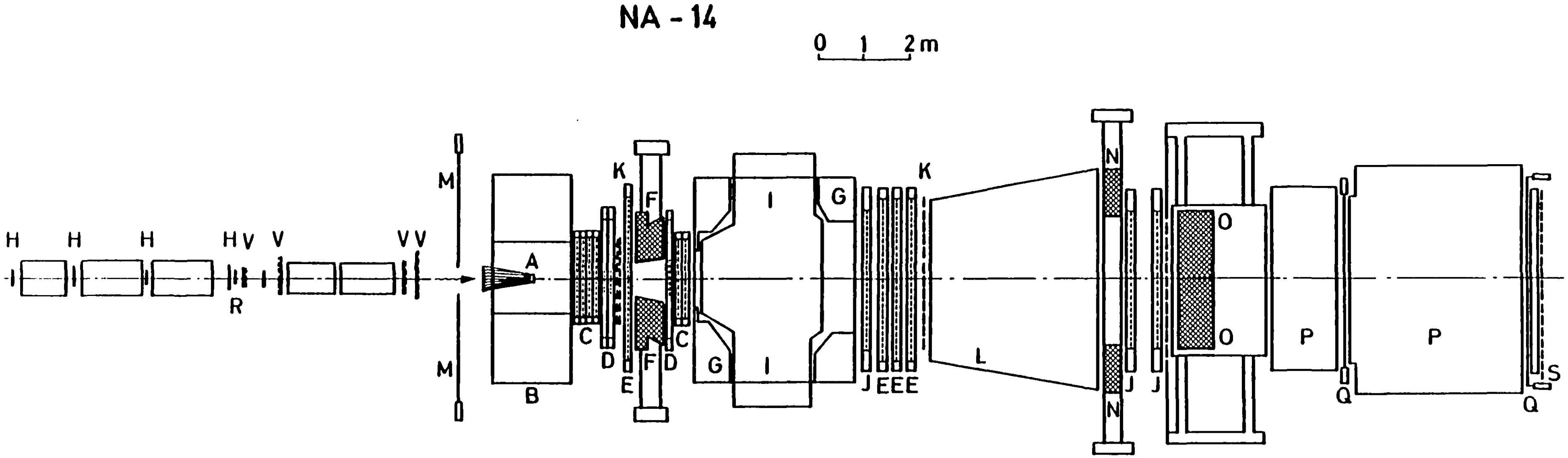

Figure caption:

H,V	tagging hodoscopes	F	"crown" lead glass calorimeter		
M	muon veto	G	Goliath Magnet		
A	active target	I,L	Čerenkov Counters	O	Olga-Penelope Calorimeter
B	AEG vertex magnet	K	trigger hodoscopes	P	iron filter
C,D,E,J	MWPC's	N	Imperial College Calorimeter	Q,S	μ hodoscopes

Figure 1.4

Three electromagnetic calorimeters provide good coverage for the detection and measurement of photons and electrons. Each comprises a two-dimensional array of scintillator hodoscopes which yield spatial information. Acceptance at large angles (150 to 300 mrad) is provided by the CROWN lead-glass calorimeter located 3 m downstream of the experimental target. OLGA, the central lead-glass detector, provides an acceptance up to 80 mrad. The region in between is covered by ILSA, the Imperial College lead-scintillator sandwich sampling calorimeter.

The spectrometer has two magnets which have vertical fields with a total integrated field strength of 4 Tm. The first of these is the AEG (1 Tm) magnet and affords the measurement of low-momentum tracks. Higher-momentum tracks are deflected in the Goliath (3 Tm) magnet. The AEG also serves to sweep away most of the background of soft (<100 MeV/c) electromagnetic pairs. This background is troublesome because, besides their emission angle, several effects give a finite vertical extension to the region of these electron-positron pairs: multiple coulomb scattering, the size and divergence of the beam and the vertical kick due to the small horizontal component of the magnetic field all contribute.

Charged particle trajectories are determined with the aid of sixty-four planes of multiwire proportional chambers arranged in three stacks. These are located in field-free regions to avoid the problems associated with spiralling soft electrons and positrons. A horizontal dead zone, corresponding to two standard deviations of the vertical Coulomb scattering of the soft electromagnetic background, is needed in the first stack. However, since this dead zone corresponds to substantial vertical transverse momentum, energetic particles in the central region have some chance of being lost. Consequently, the desensitized region in the median plane of the chambers is covered by other small fast chambers optimized for large fluxes.

A single multicell gas Cerenkov affords particle identification; the radiator is dry air, which gives a threshold of about 6 GeV/c for pions. Finally, an iron muon filter equipped with scintillator hodoscopes provides identification of, and the option of triggering on, muons.

1.4 The BEG Tagged Photon Beam

Sensitivity at the nanobarn level (the cross-section of, for example, the QED Compton process is only a few nb at values of $p_T > 2$ GeV/c for the final state photon) requires that the flux of the incident photon beam be very large. In addition, in order to reduce the background due to neutral hadrons interacting in the experimental target and producing spurious high-p_T final states, the beam has to be very pure. The Broadband Electron and Gamma beam (BEG) has been designed [22] to yield the maximum flux of high-energy photons with a very low hadronic contamination. This is realized in a multi-step process, the photons ultimately being produced by the bremsstrahlung of a beam of electrons obtained using the so-called "classical two-step method". The parameters of the BEG are summarized in table 1.1 and the beam layout is shown schematically in figure 1.5.

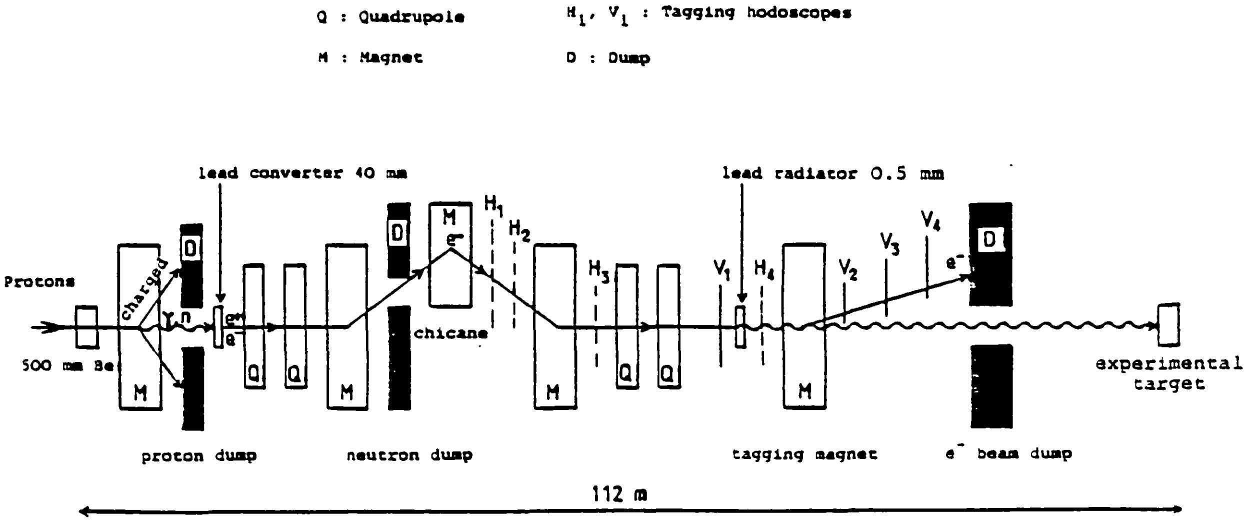

Figure 1.5

Primary Proton Beam	intensity	2×10^{12}/burst
	energy	400 GeV
Electron Beam	intensity	10^{8}/burst
	energy range	120-250 GeV
	mean energy	140 GeV
Tagged Photon Beam	intensity (with photon energy > 65 GeV)	5×10^{6}/burst
	mean energy	80 GeV
	tagging resolution	1.5 GeV
Beam Size ($\pm2\sigma$)	horizontal	±34 mm
	vertical	±22 mm
Hadronic Contamination		$< 10^{-4}$

Table 1.1

The first stage of the process is the production of an intermediate photon beam from the decay of neutral pions. The neutral pions, which decay almost instantaneously into pairs of photons, are amongst the secondary particles produced when high-energy protons from the CERN SPS interact in a 500 mm long beryllium target. The length and composition of this production target are a compromise to ensure that sufficient incident protons interact but that few photons are lost in the creation of electron-positron pairs before they can emerge from the target. Beryllium is chosen because, being an element of low atomic number, the ratio of its radiation length to its nuclear interaction length is high. About 70% of the primary protons do interact in the target. Those which do not, together with any charged secondaries, are deflected by sweeping magnets immediately downstream of the production target into the proton dump, a 4 m thick iron wall. The neutrals pass through a hole in the proton dump and the photons are made to pair produce in the next stage of the process.

Around 60% of the photons are converted into electron-positron pairs in a 4 mm thick (70% of a radiation length) lead converter placed 14 m downstream of the production target. The high-energy electrons are then focused by a quadrupole doublet on the entrance of the first magnet of the so-called "chicane". Electrons are chosen, rather than the positrons, in order to reduce the muon contamination of the beam. (The flux of μ^+ is roughly a factor of two greater than that of μ^- due to the positive charge of the primary proton beam.) The flux of electrons could be increased by increasing the thickness of the lead converter, but this would degrade their mean energy. The thickness and composition of the converter is not only a compromise between the flux and energy spectrum of the electrons produced; it is also chosen to minimize the probability that a neutral hadron will interact within it to produce a negatively-charged particle that would contaminate the electron beam. The neutral contamination at this stage is due mainly to neutrons, kaons, and to photons which did not convert into electron-positron pairs.

The chicane serves to reject low-energy electrons, which are defocused in one of the five chicane magnets, and to kill the neutral background. Neutral and positively-charged particles are dumped into a second 4 m thick iron wall, the neutron dump. The positive particles are mainly positrons, together with pions and protons resulting from the decays $K^o_S \rightarrow \pi^+\pi^-$, $\Lambda^o \rightarrow \pi^-p$ and $\bar{\Lambda}^o \rightarrow \pi^+\bar{p}$. Essentially, all electrons with a momentum greater than 120 GeV/c are transported and used, in the final stage, to produce a photon beam by bremsstrahlung.

The electron beam impinges on a 0.5 mm thick (10% of a radiation length) lead radiator in which some 10% of the electrons radiate single high-energy bremsstrahlung photons. The thickness of the radiator is chosen to maximize the probability that a single photon is produced per incident electron. (Increasing its thickness would result in a larger photon flux, but would also increase the probabiity of multiple bremsstrahlung which would degrade the energy resolution of the tagging system.) The electron beam is focused on the experimental target by a quadrupole doublet so that, because of the high energy of the radiating electrons, the photons which they emit are also directed at this target. Before reaching the experimental target, the photons pass through two collimators separated by a cleaning magnet which sweeps away any energetic charged particles. The charged particles are mainly electrons which did not radiate and negatively-charged pions and antiprotons resulting from the above-mentioned decays of neutral hadrons.

A tagging system has been built to measure both the energy of the photons and the intensity of the beam. It has been designed to operate at rates of a few 10^8 electrons incident upon the radiator per effective second of spill. The system comprises scintillator hodoscope arrays equipped with very fast photomultipliers, which are operated at low gain in order to withstand the high rates. The use of time-to-digital converters enables a figure of 2 ns to be achieved for the time resolution of an electron's flight. Four hodoscopes (H_1-H_4), each with narrow vertical fingers, measure the electron momentum in the last bend before the radiator. Likewise, four hodoscopes (V_1-V_4) with horizontal fingers are used to determine the electron momentum after the radiator from the vertical deflection in the field of the tagging magnets. In order to maximize the tagging efficiency, the hodoscopes are located remote from magnet exits to avoid the background synchrotron radiation emitted by the electron undergoing measurement. The difference between the electron energies calculated before and after bremsstrahlung gives an estimate of the energy of the photon. The energy spectrum of the photon beam, as measured by the tagging system, is shown in figure 1.6.

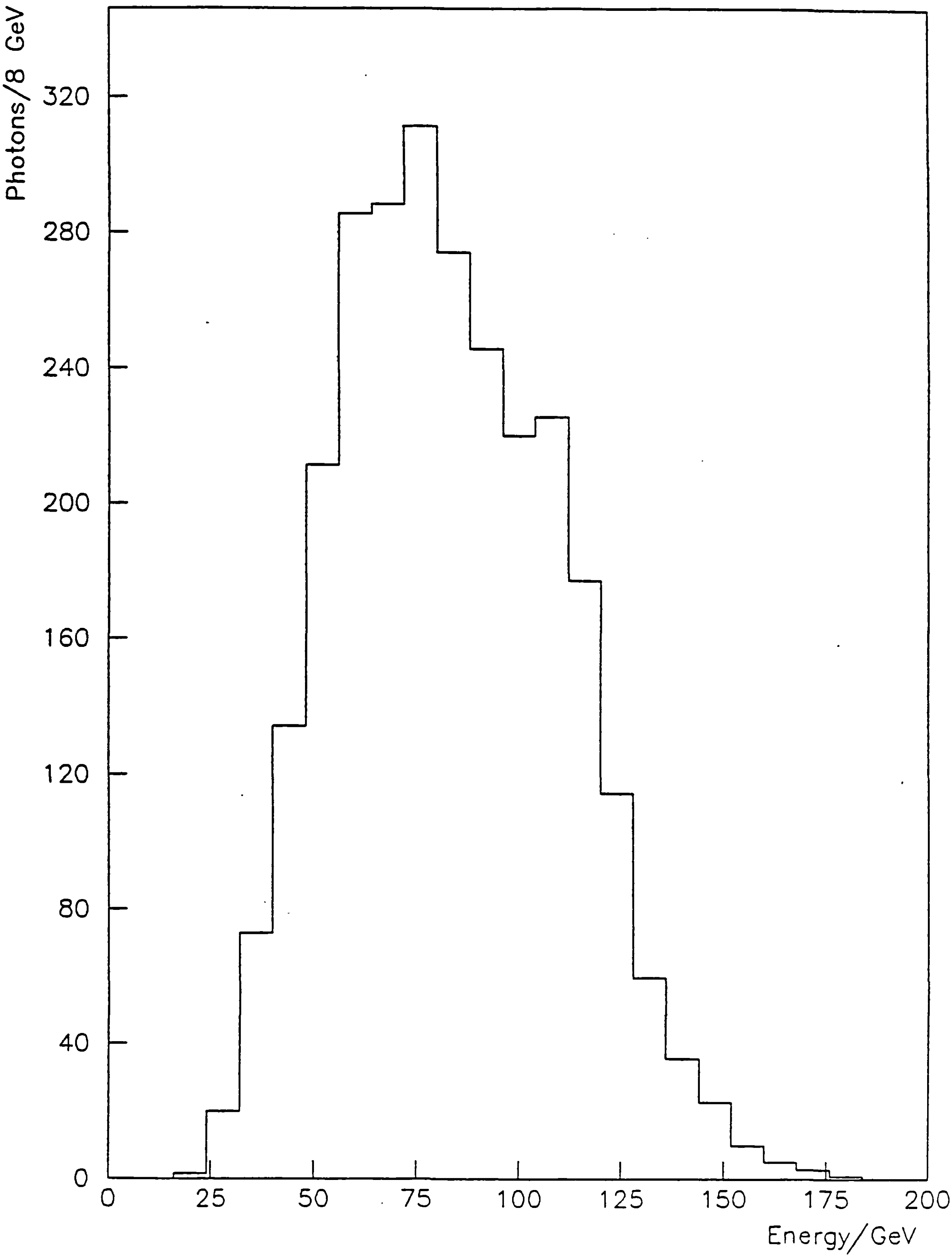
Photons/8 GeV
320
280
240
200
160
120
80
40
0
0
25
50
75
100
125
150
175
200
Energy/GeV

Figure 1.6

Chapter 2

A SURVEY OF SOME EXISTING AND PROPOSED EXPERIMENTS EMPLOYING SEMICONDUCTOR DETECTORS

2.1 Introduction

The first semiconductor detectors to be included in the apparatus of a high-energy physics experiment were thick single-element devices which acted as targets for the study of elastic scattering off nuclei [23][24]. Their role was to provide a measurement of the energy of the recoiling nucleus in order to identify the nature of the interaction, that is they served to differentiate between coherent and incoherent events.

The resolution of the recoil energy measurement is limited by uncertainties which are dependent upon the thickness of the semiconductor detector. The fact that the exact interaction point, and hence the fractions of the detector crossed by the single incoming particle and by the outgoing ones, is unknown introduces such an uncertainty. Consequently, a target comprising several thin detector layers, rather than a single thick device, was employed to select coherent events in later experiments studying diffractive multi-pion production [25][26].

The discovery of charmed particles has created a new and more exacting field of application for semiconductor detectors: the measurement of the lifetime of heavy weakly-decaying particles. This requires not only the selection of coherent events, but also the identification of the production and decay vertices with sufficient spatial resolution to enable the decay path length to be determined.

Selected experiments are reviewed in this chapter to illustrate this and other current applications of semiconductor detectors in high-energy physics. The implementation of silicon devices in the NA14 experiment is detailed in Chapter 6.

2.2 NA1

The CERN experiment NA1 [27] is run by a collaboration from Frascati, Milan, Pisa, Turin, Trieste and Westfield College, London. A particular aim of the experiment has been to study heavy states photoproduced coherently in a multi-layer silicon target. Coherent photoproduction establishes the quantum numbers of the final state and so is well-suited for the study of the fragmentation of the photon into vector mesons or into non-resonant $J^P = 1^-$ states. Notably, charmed meson pairs are amongst the allowed final states, provided that the incoming photon energy is sufficiently high.

Coherent photoproduction is particularly suitable for charged D-meson lifetime studies because almost all of the energy of the incoming photon is transferred to the charmed meson pair. The short decay path of these particles may then be stretched up to the order of a few millimetres by a large Lorentz factor. Coherent production offers a further advantage in that the recoiling nucleus is contained inside a single silicon layer. In an incoherent interaction highly-ionizing evaporative protons or recoiling nuclear fragments may traverse detector layers downstream of the interaction point and confuse the charmed meson decays. In addition, the combinatorial background in a coherent event remains confined to the decay products of the two particles under study.

The price to be paid for demanding coherent production is in the counting rate which, for photoproduction, drops by a factor of ten if diffractive events only are selected and by a further energy-dependent factor if coherence is required. Furthermore, the mutual interference between the amplitudes of the A = 28 nucleons of the silicon nucleus, due to their collective participation (by definition) in any coherent interaction, prevents the study of the production amplitude off a single nucleon. Consequently, although the coherent photoproduction of charmed mesons affords the study of their lifetime, it precludes the investigation of a specific production mechanism such as photon-gluon fusion.

The experiment recorded 1.8 million triggers in a 40 day run using a bremsstrahlung photon beam derived from a 150 GeV/c electron beam incident at an intensity of some $2{\times}10^6$ electrons/s upon a 0.1 radiation length lead radiator. It employed an "active target" comprising forty silicon junction detectors, each 300 μm thick, 100 μm apart and 14 mm in diameter.

Photon conversions give rise to a counting rate which grows along the active target and approaches 1 MHz in the final layers. To cope with the non-uniform rate, some resolution is sacrificed by reducing the 500 ns trapezoidal pulse-shaping associated with the first half of the active target to obtain triangular pulses of 100 ns duration from the last twenty detectors.

A forward spectrometer (see figure 2.1) covers a solid angle of 0.8 msr for charged particles and of 0.25 sr for photons. It is used to select $D\bar{D}$ (and $D^*\bar{D}$, $D\bar{D}^*$, $D^*\bar{D}^*$) candidates by reconstructing their masses from measurements of the momenta of the secondaries produced by their decay. The active target is surrounded by a set of veto counters for charged particles and photons in order to eliminate the majority of incoherent events and all events in which particles are produced at greater than 500 mrad. A single charged particle is allowed up to 500 mrad in order to accept events in which the pion from an excited D-meson decay goes outside the acceptance of the forward spectrometer.

The most dangerous source of background is the conversion in the active target of energetic photons from secondary neutral pions or of soft

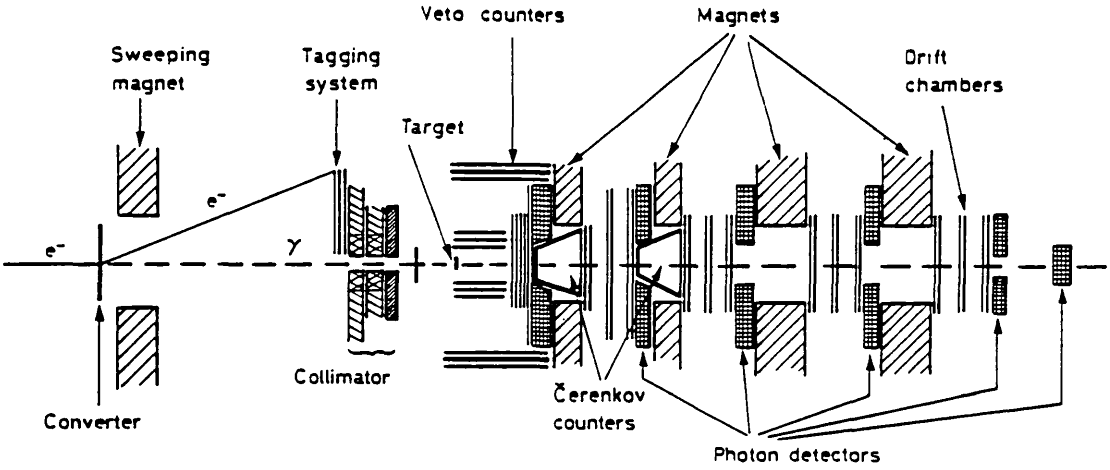

Figure 2.1

photons from double bremsstrahlung into electron-positron pairs. The production of an energetic electron-positron pair can simulate a secondary decay in the target, so all events in which an electron is identified in the forward spectrometer are rejected. A soft pair usually produces a signal spike in only one detector, hence simulating a nuclear recoil. Such events cannot easily be removed.

An off-line analysis of the signals from the silicon detectors enables incoherent events in which nuclear fragments cross more than one detector to be rejected. The active target identifies the production and decay vertices as signalled by steps in the charged particle multiplicity of the successive final states. In figure 2.2 examples of three events detected by the active target are compared with the spectrometer outcome, the signal amplitudes from the silicon detectors being expressed in units of single minimum-ionizing particles. Finally, the average Lorentz factor of the $D\bar{D}$ pair, which is known from their reconstructed energy, is used to calculate the proper lifetime corresponding to the observed decay path length (or lengths).

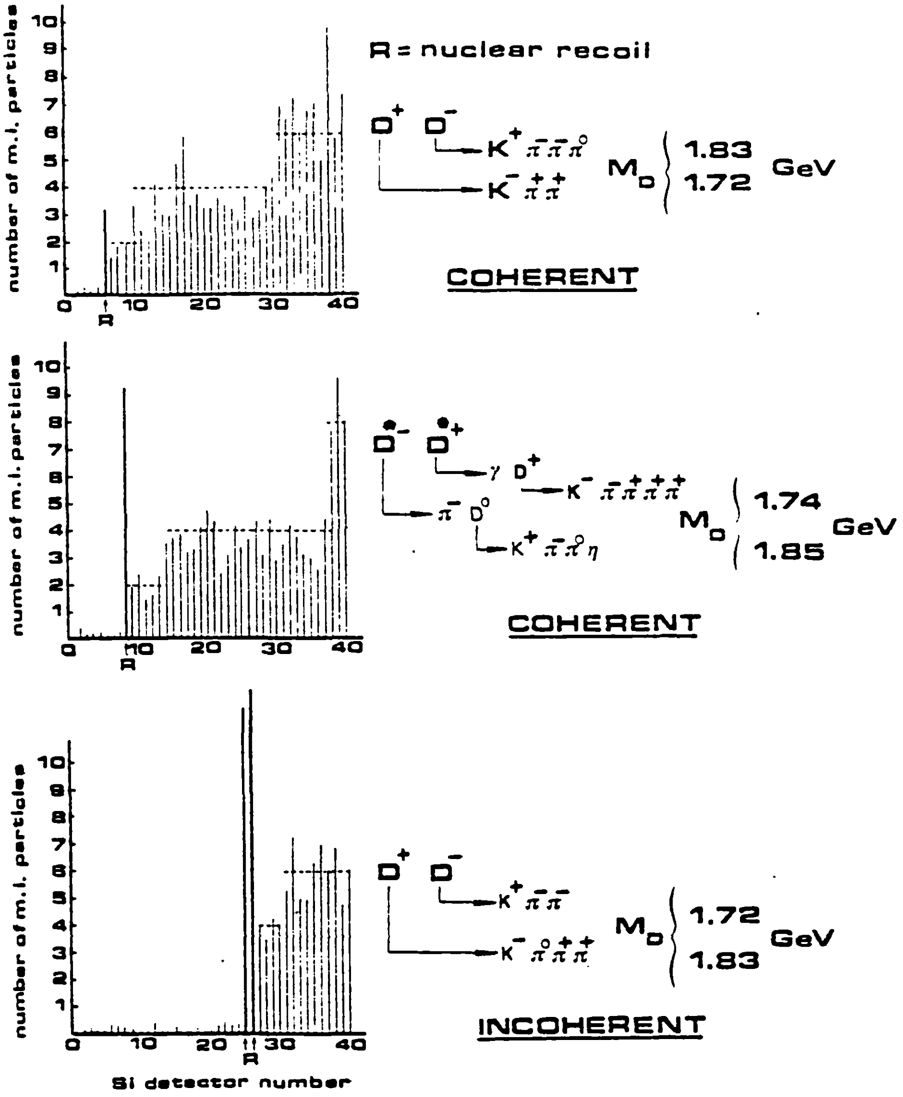

Figure 2.2

The $D^{\pm}$ lifetime has been estimated [28] from a sample of 98 decays in 86 events. The time distribution of these identified charmed decays is shown in figure 2.3. The solid line is the $D^{\pm}$ contribution, while the broken line is an overall fit to the data taking into account a D° contamination of approximately 20%. The fit yields a value for the $D^{\pm}$ lifetime of $(9.5 \, {}^{+\,3.1}_{-\,1.9}) \times 10^{-13}$ s.

It has been proposed [29][30] to extend the measurements of the NA1 experiment using an active target of finer granularity to make the lifetime

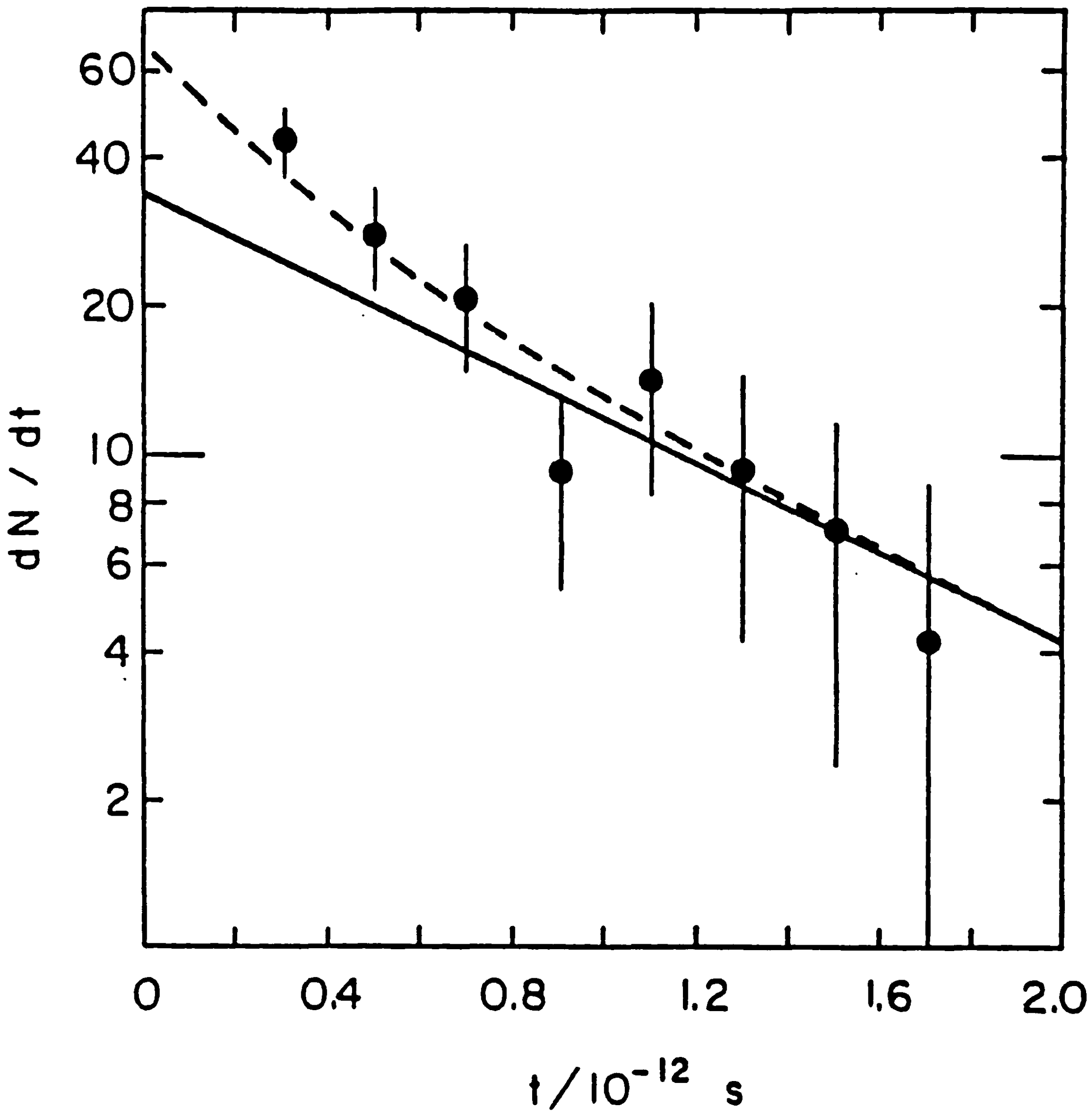

Figure 2.3

region of D°'s, F's and Λ_c's accessible. The granularity required is of the order of 100 μm and cannot be realized using silicon detectors because the noise would exceed the signal. However, it is hoped to overcome this signal-to-noise limitation using a monolithic germanium multi-electrode detector operated at liquid nitrogen temperature. Prototype devices, each composed of a single germanium crystal 5 mm long, 5 mm high and 20 mm wide, have been tested. The lower face of the crystal acts as an ohmic contact, while the longitudinal granularity is defined by fifty electrode strips 50 μm wide and 50 μm apart deposited on the upper one, as illustrated in figure 2.4.

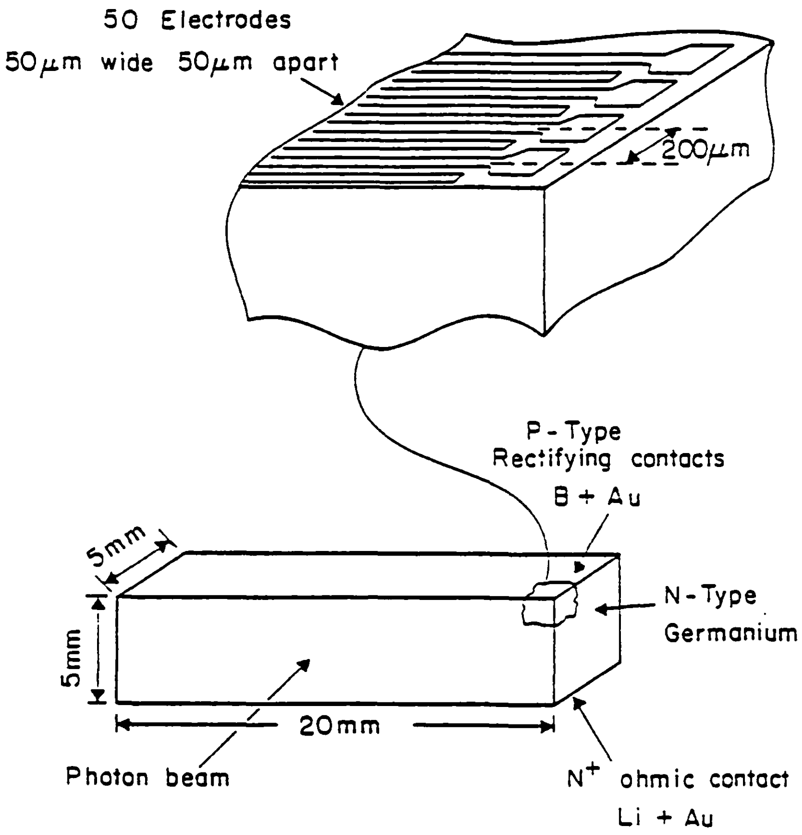

Figure 2.4

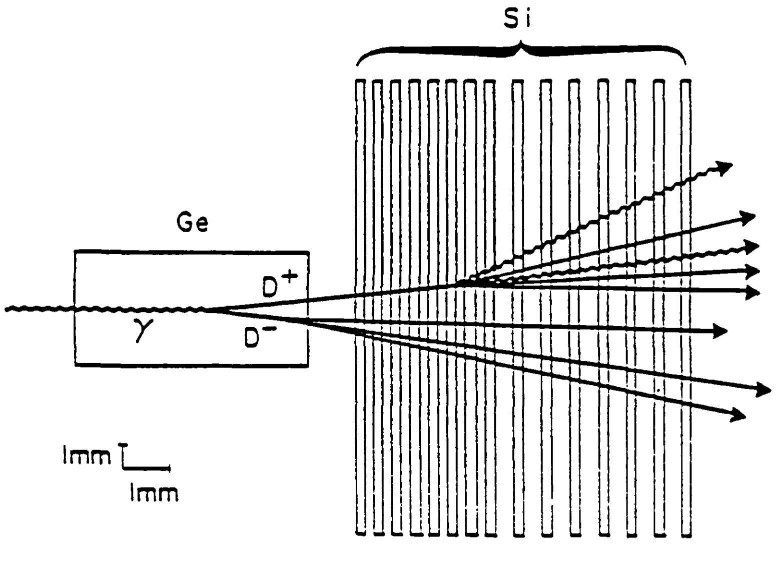

Figure 2.5

Charge carriers produced upon the passage of ionizing particles drift in the vertical field established by the electrodes, enabling the longitudinal development of the event to be examined.

Germanium is chosen in preference to silicon because its higher density and atomic number lead to greater ionization energy loss in a given detector thickness and because more charge carriers are produced in germanium for a given energy deposited by an incident particle. Overall, there is a gain in signal by a factor of about 2.5 with respect to silicon.

It is planned to install an active target comprising a monolithic germanium detector followed, in the same cryostat, by a series of fifteen silicon detectors (see figure 2.5). Each silicon device is 200 μm thick and has its active area divided into four 5×20 mm^2 sections in order to reduce the capacitance and hence the noise. The detectors are separated by 200 μm in the first half of the multi-layer stack and by 400 μm in the second. This target configuration constitutes 0.2 radiation lengths, of which 85% is concentrated in the germanium, thus ensuring that production takes place near the beginning of the target and that most of the 1.3 cm useful length is available for the detection of decay paths.

2.3 NA11

The hadronic production of charmed particles in a conventional beryllium target has been studied in the CERN experiment NA11 [31] by a collaboration from Amsterdam, Bristol, CERN, Cracow, MPI Munich and the Rutherford Laboratory. In order not to be limited to low-multiplicity charmed decays due to the high combinatorial background in the inclusive data (which show an average charged particle multiplicity of eleven), high-resolution silicon detectors have been added to measure the vertex topology. Those particles consistent with a displaced secondary vertex can then be identified and the combinatorial and non-charmed backgrounds reduced.

A detector granularity of 20 μm was required to achieve the desired spatial resolution, so the silicon detectors are "microstrip" devices with their active areas segmented into strips of 20 μm pitch. Due to the prohibitive cost of the electronics and to the fan-out problem, not every strip is read out. Instead, only every third strip in the central region and every sixth strip in the outer regions of each detector is connected. This reduces the amount of electronics associated with one detector from 1200 to a manageable 240 channels. The intermediate strips are left floating, but charge interpolation permits the passage of an energetic particle to be localized to the nearest strip because, due to the capacitance between neighbouring strips, the charge deposited by an incident particle is divided and ultimately appears on strips which are read out.

The geometry of the silicon vertex detector was decided on the basis of a Monte Carlo simulation. In the configuration chosen six microstrip detectors, each 300 μm thick and having an active area of 36×24 mm^2, are arranged in three doublets with the strips inclined at alternately ±14° to the horizontal. According to the Monte Carlo assessment, the arrangement affords a vertex resolution of 10 μm laterally and 250 μm longitudinally.

An extension of the NA11 programme is planned in an upgraded version of the existing experiment designated NA32 [32]. The apparatus (see figure 2.6) remains essentially a large aperture two-magnet spectrometer with three multicell Cerenkov counters for hadron identification, but the six microstrip devices of the vertex detector are augmented by four more to define with precision the incoming 200 GeV/c π^- beam and the beryllium target is replaced by an active one comprising a further twelve silicon detectors. The target detectors are also segmented devices and are arranged in two separate stacks. A fast microprocessor will analyse the information from the silicon detectors and will take the trigger decision on the basis of a change in charged particle multiplicity in the active target being consistent with a charmed decay.

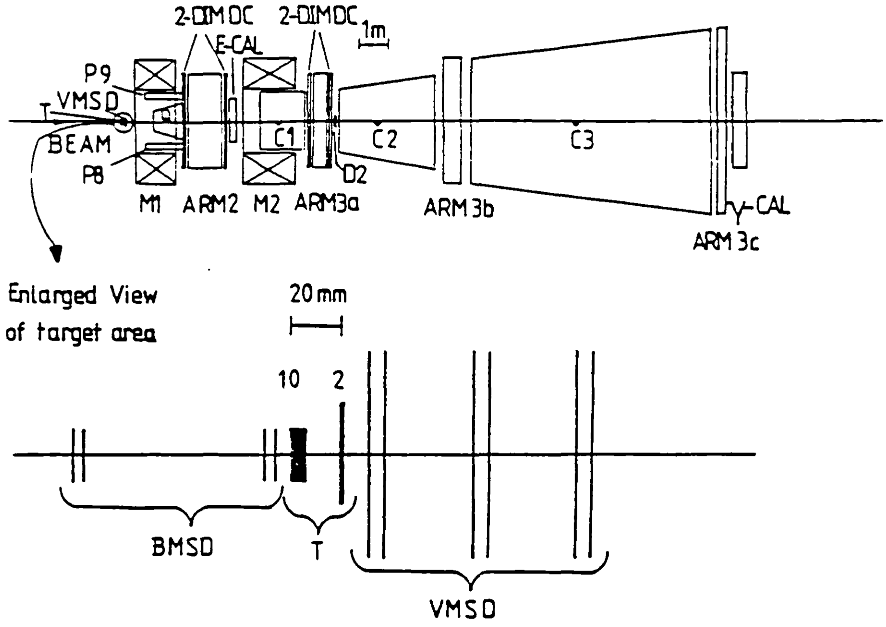

M1,M2	: Large aperture spectrometer magnets
ARM2-ARM3c	: Drift chambers
Q,C1,C2,C3	: Multicell threshold Čerenkov counters
P8,P9	: MWPCs
E-CAL	: Electron/photon calorimeter
γ-CAL	: Forward photon calorimeter
D2	: Veto counter
T	: Active silicon target (10+2 planes of strip detectors)
VMSD	: Vertex telescope (6 planes of strip detectors)
BMSD	: Beam telescope (4 planes of strip detectors)

Figure 2.6

2.4 E-653

The experiment E-653 [33] (a Kariya-FNAL-Kobe-Seoul-Nagoya-Ohio-Okayama-Oklahoma-Osaka-Ottawa-Tokyo-Toronto-Yokohama collaboration), which is currently in preparation at Fermilab, has been inspired by the success of the neutrino experiment E-531 in measuring the lifetime of weakly-decaying particles produced in an emulsion [34]. The aim of the new experiment is to study the lifetime and decay properties of charmed and beauty particles hadronically produced in a hybrid emulsion spectrometer (see figure 2.7) using protons of the highest available energy.

E-653

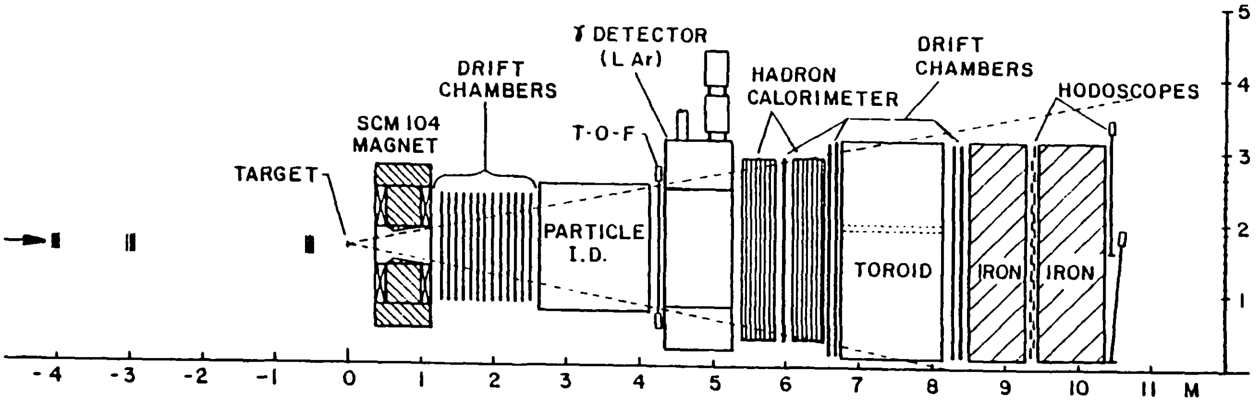

Figure 2.7

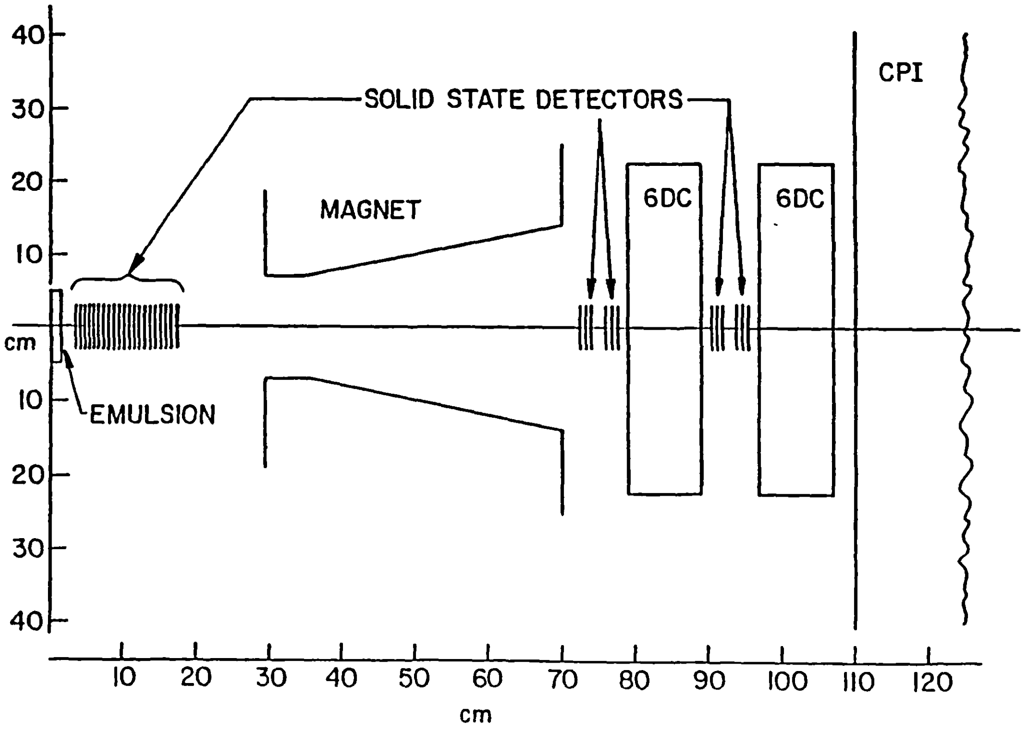

Figure 2.8

The experiment employs a high-resolution vertex detector comprising twenty-one silicon microstrip devices spaced 7 mm apart, with seven detectors measuring each of three projections inclined at 60° to each other. In the central 6 mm region of each detector, where the track density is highest, every strip is read out. Elsewhere, only every third or every tenth strip is connected, resistive charge division enabling one strip fractional resolution to be achieved by charge interpolation. Short-lived decay candidates will be identified off-line by means of the vertex detector, which is located immediately downstream of the emulsion (see figure 2.8) and which will pinpoint secondary vertices with an estimated precision of 15 μm laterally and 200 μm longitudinally. The decays will then be sought in the thin emulsion target.

Tracks within 30 mrad of the beam will be reconstructed with the aid of two pairs of silicon microstrip detector triplets located downstream of the spectrometer magnet and covering the region in which the drift chambers are inadequate. An additional silicon detector triplet 283 cm downstream of the emulsion provides a long lever arm for very stiff tracks. All of these downstream detectors are the same size as the vertex ones, viz. 300 μm thick with an active area 60 mm in diameter, and have every tenth strip read out.

Chapter 3

SEMICONDUCTOR DETECTORS

The use of a semiconductor junction device for nuclear particle detection was reported as early as 1949 [35], but it was not until the early 1960's that such detectors became practicably available and found widespread use in nuclear spectroscopy. These devices, employing a semiconductor as the detection medium, became known by the somewhat ambiguous generic name of "solid-state detectors". Only recently have they found useful application in high-energy physics experiments.

3.1 General Characteristics

The passage of an energetic charged particle through a semiconducting medium produces electron-hole pairs, the solid-state analogue of the ion pairs created in a gas-filled detector chamber, along the track of the particle. The incident particle produces energetic secondary electrons (or "delta rays") which, in turn, produce more electron-hole pairs. This cascade process continues until no electron has sufficient energy to cause further impact ionization. The total number of pairs produced is E/W, where E is the total energy deposited by the incident particle and W is the average energy required to create an electron-hole pair. The quantity W is experimentally observed to be largely independent of both the energy and type of the incident radiation. This gives a semiconductor detector a linear relationship between the amplitude of the signal resulting from the collection of the charge carriers and E (above a certain low threshold energy).

The great advantage of semiconductor detectors is the high energy resolution which they can achieve as a direct consequence of the small practical values of W. For silicon, $W = 3.62$ eV (at 300 K) [36], whereas the energy required to create an ion pair in a gaseous detection medium is typically 30 eV and that required to produce a photoelectron in a scintillator-photomultiplier combination is of the order of 300 eV. Thus the number of charge carriers produced is much greater, for a given energy deposited in the detector, in the semiconductor case. This means not only a better signal-to-noise ratio, but also that the statistical fluctuations in the number of charge carriers are smaller fractions of the total. This last point is particularly important since it is usually the degree of statistical fluctuation that determines the limiting energy resolution of a high-energy radiation detector.

The statistical fluctuations observed in semiconductors are smaller than would be expected if the formation of charge carriers were a Poisson process. Fano [37] has shown that this is because the ionization events should not be treated as completely independent. The Fano factor, F, provides the appropriate adjustment and is defined as the ratio of the observed statistical variance, ν, to the Poisson-predicted variance, which is simply the expectation number of charge carriers produced, E/W. The correct analysis considers the fluctuations in the division of energy loss between ionizing and non-ionizing processes. Without the competing energy-loss processes, all of the deposited energy would result in electron-hole production and there would be no statistical fluctuation; that is, $F = 0$. If, on the other hand, the probability of charge-carrier production were very small, Poisson statistics would indeed be expected to hold; that is, $F = 1$. The value of the Fano factor for silicon has been determined to lie in the range 0.085 to 0.137 [38]. From the definition of F it follows that the limiting energy resolution is

$$\frac{\Delta E}{E} = \frac{W\sqrt{\nu}}{E} = \sqrt{\left(\frac{FW}{E}\right)} \qquad (3.1)$$

Hence the importance of small W.

Although the value of W is attractively small for silicon, it is more than three times the band gap energy difference, E_g, between the valence and conduction bands of the solid. The threshold for a photon to create an electron-hole pair is simply E_g, but that for impact ionization is rather more due to kinematic constraints. If the electron and hole effective masses were equal, the impact ionization threshold would be roughly $1.5E_g$. This is not usually the case and in silicon the threshold is somewhat higher. As the energy of an electron approaches this threshold, energy can also be dissipated through strong coupling to the lattice vibrations of the solid. This is the mechanism of the competing energy-loss process on the basis of which William Shockley [39] has calculated W.

In addition to their good energy resolution characteristics, semiconductor detectors offer the advantages of compactness, relatively simple structure and fast response time. Their small size may, of course, limit some applications and their susceptibility to performance degradation due to radiation damage may limit others. Their greater density and stopping power compared with gas-filled detectors first gave semiconductor detectors application in total-absorption nuclear spectroscopy. However, the current popularity enjoyed by semiconductor detectors in high-energy physics applications derives from the fact that they can be made uniformly very thin and so act as sampling detectors giving a measure of the specific rate of energy loss, dE/dx (where x denotes path length).

The thickness of the silicon detectors employed in high-energy physics experiments typically varies between 200 μm and 1 mm. Figure 3.1 shows the range in silicon of several different particles as a function of their energy. For particles incident at relativistic velocities, the most-probable energy loss in silicon is some 27 to 30 keV per 100 μm traversed. (The dependence of the energy loss on thickness is non-linear for thin detectors.)

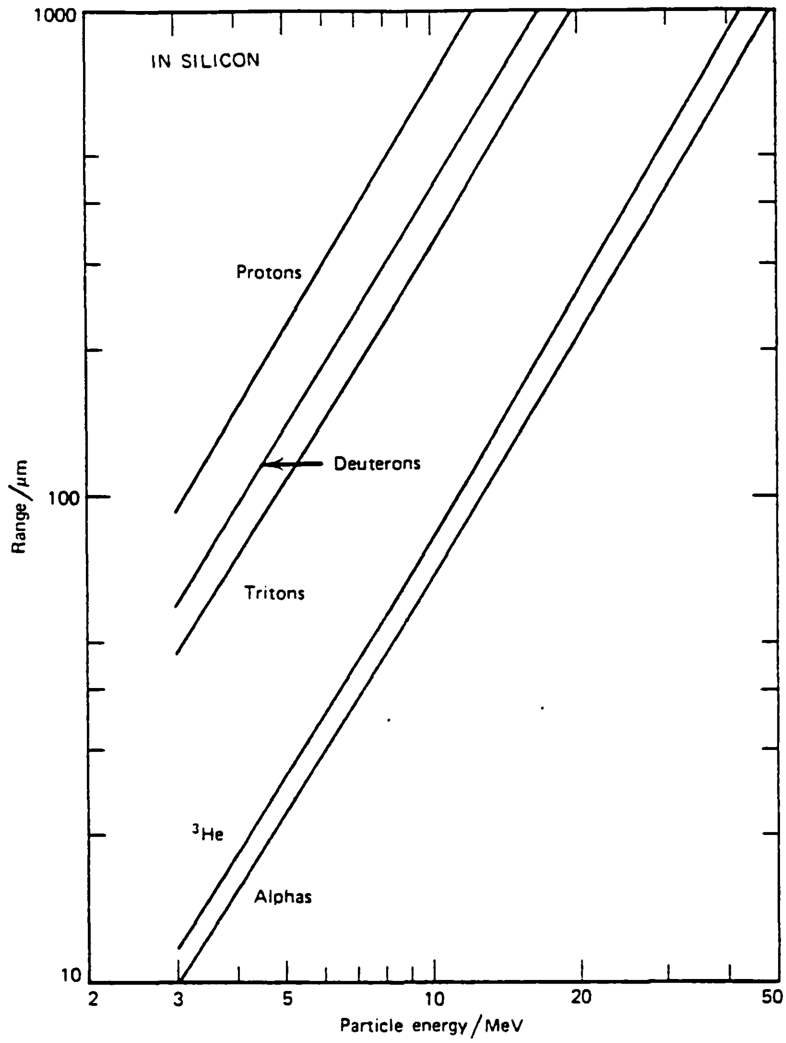

Figure 3.1 [40]

A treatment of the statistical nature of the ionization energy-loss mechanism is given in an appendix to this thesis.

3.1.1 Leakage Current

In order to create an electric field which is large enough to collect the charge carriers efficiently from a semiconductor junction detector, several hundred volts must typically be applied across the depletion layer which constitutes its active volume. The advantage of a reverse biased p-n junction is that a high field is obtained without requiring a very high resistivity material or large DC power dissipation. However, due to the finite electrical conductivity of any semiconductor, the reverse bias applied to a junction detector causes a standing "leakage" current through it.

This bulk leakage current is not just a result of the diffusion of minority charge carriers into the depletion region whence they are swept on through by the applied electric field. A further and often more significant contribution comes from the generation of charge carriers at recombination centres (see section 3.1.2) within the depletion region itself.

A second and less well-understood form of leakage current is that which flows at the surface of the device. The magnitude of such surface-generated currents is markedly dependent upon the method of construction, surface chemistry and the prevailing ambient conditions, notably humidity. Encapsulation techniques or guard rings are sometimes employed to suppress surface leakage.

The inevitable random fluctuations in the leakage current constitute a source of noise which will tend to obscure the small signal current which flows following the passage of an ionizing particle. It is essential, therefore, to minimize the leakage current and this requirement precludes the general use of non-rectifying "ohmic" contacts in semiconductor detectors. Instead, one electrode must be made "non-injecting" so that, unlike an ohmic contact, it does not permit charges of both signs to flow freely. Thin semiconductor layers which have a very high conductivity as a result of an unusually high impurity concentration are often used to make electrical contact with semiconductor detectors. These heavily doped n- and p-type layers (denoted n^+ and p^+, respectively) have a very low minority carrier concentration and, consequently, charge carriers initially removed from the bulk of the detector by the application of an electric field are not replaced from such an electrode, leading to a reduction in the steady-state leakage current which would otherwise flow.

Silicon detectors have a sufficiently low thermally-generated leakage current to allow their use at room temperature, whereas germanium detectors must normally be operated at liquid nitrogen temperature because the smaller band gap in germanium results in very many more thermally-generated electron-hole pairs. Silicon is the predominant semiconductor material used in the manufacture of high-energy radiation detectors.

3.1.2 Trapping and Recombination

In an ideal detector, all of the charge produced by a primary incident particle is collected at the electrodes and contributes to the signal. In practice, charge carrier lifetimes are not infinite and carriers may be prevented from traversing the detector through the mechanisms of trapping and recombination.

Semiconductors contain, in addition to any dopant material, very low levels of residual impurities. Some of these impurities may occupy substitutional lattice positions, producing energy levels near the middle of the band gap. They are termed "deep impurities" in the same sense that acceptor and donor impurities are "shallow" because their corresponding energy levels lie near the edges of the band gap. Their presence enhances the thermal contribution to conduction via a two- or multi-step process, by which an electron previously thermally excited from the valence band to an intermediate level may be re-excited into the conduction band. Deep impurities can act as trapping centres, immobilizing charge carriers for relatively long periods of time and thereby interrupting their contribution to the signal current. Certain lattice defects can also lead to trapping and charge carrier loss. These include point defects such as vacancies and interstitials, which tend to act as acceptor- and donor-like traps, respectively.

Some types of deep impurity are capable of capturing both electrons and holes and can therefore act as recombination centres. If a charge carrier of each type are trapped alternately, without the first one captured being released back to the band from which it came, then the two will annihilate thus returning the impurity site to its original state and leaving it capable of causing further recombination. In most semiconductor materials, recombination at such centres is much more probable than the direct recombination of electrons and holes across the full band gap.

The "trapping length" within a semiconductor is the mean distance travelled by a charge carrier before it is trapped or it recombines. For a detector to approach the ideal, the trapping length should be large compared with the physical dimensions over which the charge is collected. Equivalently, the charge collection time should be much shorter than the carrier lifetime.

If trapping effects become significant in a detector, the measured amount of energy loss is diminished and the peak of the signal distribution for a mono-energetic source would be spread towards the low-energy side. This can have a seriously deleterious effect on the energy resolution.

3.1.3 Noise

The main noise sources in a semiconductor detector are shot noise, excess noise and Johnson noise. Detector noise appears as undesired fluctuations superimposed on the signal current and is most conveniently expressed as that energy which, deposited by an ionizing particle, would produce a signal equal to the rms value of the noise. Together with the purely statistical fluctuations described by equation 3.1, detector noise determines the resolution with which the energy loss of incident particles can be measured.

Johnson noise is the least significant component of detector noise and is due to the fluctuations in the spatial distribution of the charge carriers caused by thermal diffusion. The random motion of the electrons and holes produces voltage fluctuations aross the detector, even in the absence of an applied electric field. The equivalent noise current generated is given by

$$\langle i_{Jn}^2 \rangle = 4kTG\Delta f \qquad (3.2)$$

where k is Boltzmann's constant, T is the absolute temperature and G the electrical conductivity of the device, and where Δf is the bandwidth.

Shot noise is also statistical in origin. It appears in any active device in which charge carriers are injected from an electrode and is due to fluctuations in the injection rate. In a semiconductor detector, shot noise arises from statistical fluctuations in the number of charge carriers comprising the bulk leakage current. Thus, in addition to the classic form of shot noise, which derives from fluctuations in the number of minority carriers entering the depletion region, there is a second component, "generation-recombination noise", which is due to carrier fluctuations originating at deep impurities within the depletion region itself. The equivalent noise current is proportional to the current flowing and is given by

$$\langle i_{sn}^2 \rangle = 2eI\Delta f \qquad (3.3)$$

where e is the magnitude of the electron charge and I is the bulk leakage or "dark" current.

Fluctuations in the surface leakage current lead to excess noise. The causes seem to be the recombination of electron-hole pairs in surface traps and the migration of carriers through the surface layer of the material. The noise power spectral density is roughly inversely proportional to frequency, that is

$$d\langle i_{en}^2 \rangle / df \sim 1/f \qquad (3.4)$$

Consequently, excess noise is sometimes termed "flicker noise".

3.2 Diffused Junction Detectors

One technique employed in the fabrication of semiconductor junction detectors is to diffuse a specific impurity into a semiconductor crystal at an elevated temperature. A diffused junction detector is typically produced by diffusing a high concentration of donor impurities into a p-type material, usually high-resistivity silicon. Phosphorous is commonly used as the doping agent and it is either diffused in from the gaseous phase or one side of the silicon wafer is coated with a solution of phosphorous pentoxide in glycol. After heating to around 800 °C for 30 minutes, electrodes are connected and the general arrangement is as shown in figure 3.2.

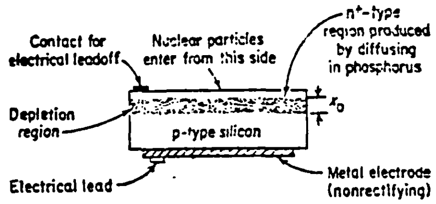

Figure 3.2

Since the surface layer is heavily doped compared with the original p-type crystal, the depletion region extends mainly into the p-side of the n^+-p junction formed. Consequently, much of the surface layer is insensitive and represents a "window" through which the incident radiation must pass before reaching the active depletion region.

Diffused p^+-n junction detectors may be produced by diffusing gallium or boron into n-type silicon.

3.3 Surface-barrier Detectors

A Schottky- or surface-barrier detector (see figure 3.3) has a very thin dead layer or "entrance window" and, in consequence, it has replaced the diffused junction detector in many applications. However, such thin entrance windows are optically transparent and allow visible photons to penetrate the active region. This sensitivity to light is a potential disadvantage of the surface-barrier detector. The somewhat tenuous nature of the surface layer also makes surface-barrier detectors prone to environmental damage and they are generally less rugged than diffused junction detectors.

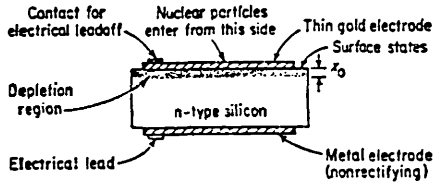

Figure 3.3

Fabrication starts with the chemical etching of a slice of n-type silicon in a solvent mixture containing nitric and hydrofluoric acid. A thin layer of silicon oxide, a p-type semiconductor, forms spontaneously upon exposure of the etched surface to the atmosphere. Electrical contact is made by the vacuum evaporation of a thin metal film, usually of gold, onto the oxide layer. This forms the non-injecting electrode. Alternatively, good results have been reported [41] when the evaporation is performed directly under conditions which promote oxidation. The oxide layer apparently plays an important role in governing the resultant properties of the surface barrier. Finally, an aluminium electrode is commonly used to form an ohmic contact with the back surface of the silicon.

Since the preparation of surface-barrier detectors does not involve any high-temperature treatment, the crystal structure is less disturbed and carrier lifetimes are not unduly reduced. As a result, generation-recombination noise is very low in surface-barrier detectors. However, due to surface leakage, the reverse-bias current is large.

A surface-barrier detector may also be produced by evaporating aluminium onto a p-type crystal to form an n-type contact.

3.4 Ion-implanted Detectors

An alternative method of introducing doping impurities at the surface of a semiconductor is to expose it to a beam of ions from an accelerator. By embedding accelerated phosphorous or boron ions, for example, it is possible to produce n^+ or p^+ layers, respectively. Mono-energetic ions from an accelerator have a well-defined range in the semiconductor, so the concentration profile of the added impurity can be closely controlled by varying either the energy or the angle of incidence of the ions during the implantation process. Radiation damage due to the ion bombardment necessitates an annealing step, but the temperature required is lower than that employed in the fabrication of a diffused junction detector. Even though their entrance windows may be made extremely thin, ion-implanted detectors tend to be more stable than surface-barrier ones and they are less sensitive to ambient conditions.

A new method of manufacturing silicon detectors has been developed [42] and is now the most popular for high-energy physics applications. A planar process, it combines the techniques of oxide passivation, photo-engraving and ion-implantation (see figure 3.4). The first step is the formation of an oxide layer and is achieved by heating the raw silicon wafer in a wet atmosphere. This oxide passivation reduces the surface leakage current. Windows are then opened in the silicon oxide by photolithographic etching and are implanted with boron to form the diode strip elements and with arsenic for the rear contact. After annealing, the detector is completed by evaporating onto it a layer of aluminium and by etching the strip and bond pad structures in further photolithographic steps.

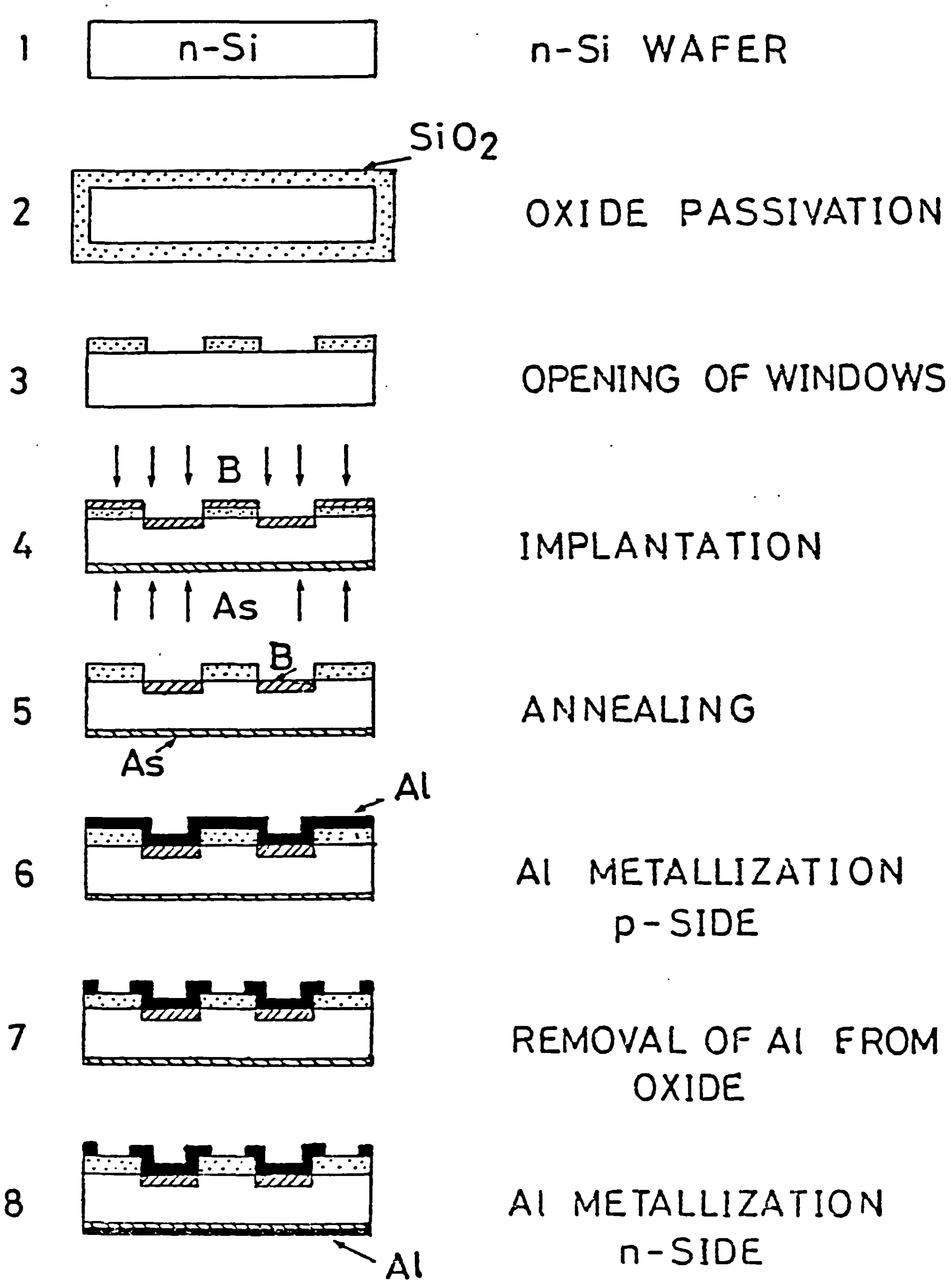

Figure 3.4

Chapter 4

DEVELOPMENT OF A POSITION-SENSITIVE SILICON DETECTOR

4.1 Preamble

In 1966 the development of a promising detector comprising several discrete detector elements on the same piece of base material was reported [43]. Structured "multi-electrode" or "strip" detectors have more recently found application in the determination of the trajectory, near the interaction region, of short-lived particles produced in high-energy interactions. Modern fabrication techniques enable "microstrip" detectors to be produced with very fine strips, affording track reconstruction to great precision. A spatial resolution of 4.5 μm, for example, has been achieved using a microstrip detector with capacitive charge division read-out [44].

Owing to the possibility of constructing a serried array of thin detector slices - an "active target" -, silicon detectors appear well-suited for the study of short-lived particles photoproduced coherently off the silicon nucleus [45][28]. The main difficulty inherent in such an approach is that a step in the measured particle multiplicity, which is the characteristic signature of a decaying particle, can also be simulated by a photon converting into an electron-positron pair. However, by employing microstrip detectors in conjunction with the active target, the track reconstruction may be improved and the problem of the background due to photon conversions alleviated. The very precise vertex determination, even at high multiplicities, afforded by such an arrangement gives the combined detector the potential for studying incoherent photoproduction in addition to the coherent photoproduction of heavy flavours.

The use of both a multi-layer silicon target and a stack of silicon microstrip detectors is foreseen in a second phase of the NA14 experiment

[46]. The combined "vertex detector" is to be installed with the aim of achieving a high event collection rate for photoproduced charmed states. To this end, a series of intensive studies has been conducted to investigate the properties of strips of various lengths and widths deposited, using different technologies, onto silicon. The energy resolution, detection efficiency, susceptibility to radiation damage at high fluence and the degree of charge division between adjacent strips were the important parameters to be determined. In addition, a clear understanding of all of the parameters of the energy-loss process is required in order to be able to interpret correctly the number of relativistic ionizing particles responsible for the observed charge collected from a given subset of the active target.

The nature of the tests performed and their findings are reported in this chapter.

4.2 Performances of Surface-barrier and Ion-implanted Silicon Detectors

A total of four microstrip detectors (see table 4.1) have been tested [47]. The pitch of the strips on each device was 200 μm, but their lengths and widths varied in order that any dependence on the strip dimensions could be established. In particular, it was suspected that, due to their increased capacitance, longer strips might degrade the noise performance of a detector.

Two of the surface-barrier devices (detectors A and B listed in table 4.1) were kindly lent to us by Erik Heijne of CERN. They were manufactured by Enertec, Strasbourg and were equipped with 30 mm long strips on the rear (aluminium) and junction (gold) side, respectively. A third surface-barrier device (detector C) was produced at Saclay with 60 mm long strips on the junction side. Detector D was manufactured by Enertec using a planar technique and had 30 mm long strips on the ion-implanted side. Detector D is shown in figure 4.1.

Detector	Construction	Surface Area/mm^2	Thickness/µm	Strip width/µm	Total Depletion Voltage/V
A	Surface-barrier	20 × 30	400 ± 5	120 ± 5	110
B	Surface-barrier	20 × 30	400 ± 5	100 ± 5	120
C	Surface-barrier	20 × 60	400 ± 5	80 ± 5	130
D	Ion-implantation	20 × 30	300 ± 5	100 ± 5	150

Table 4.1

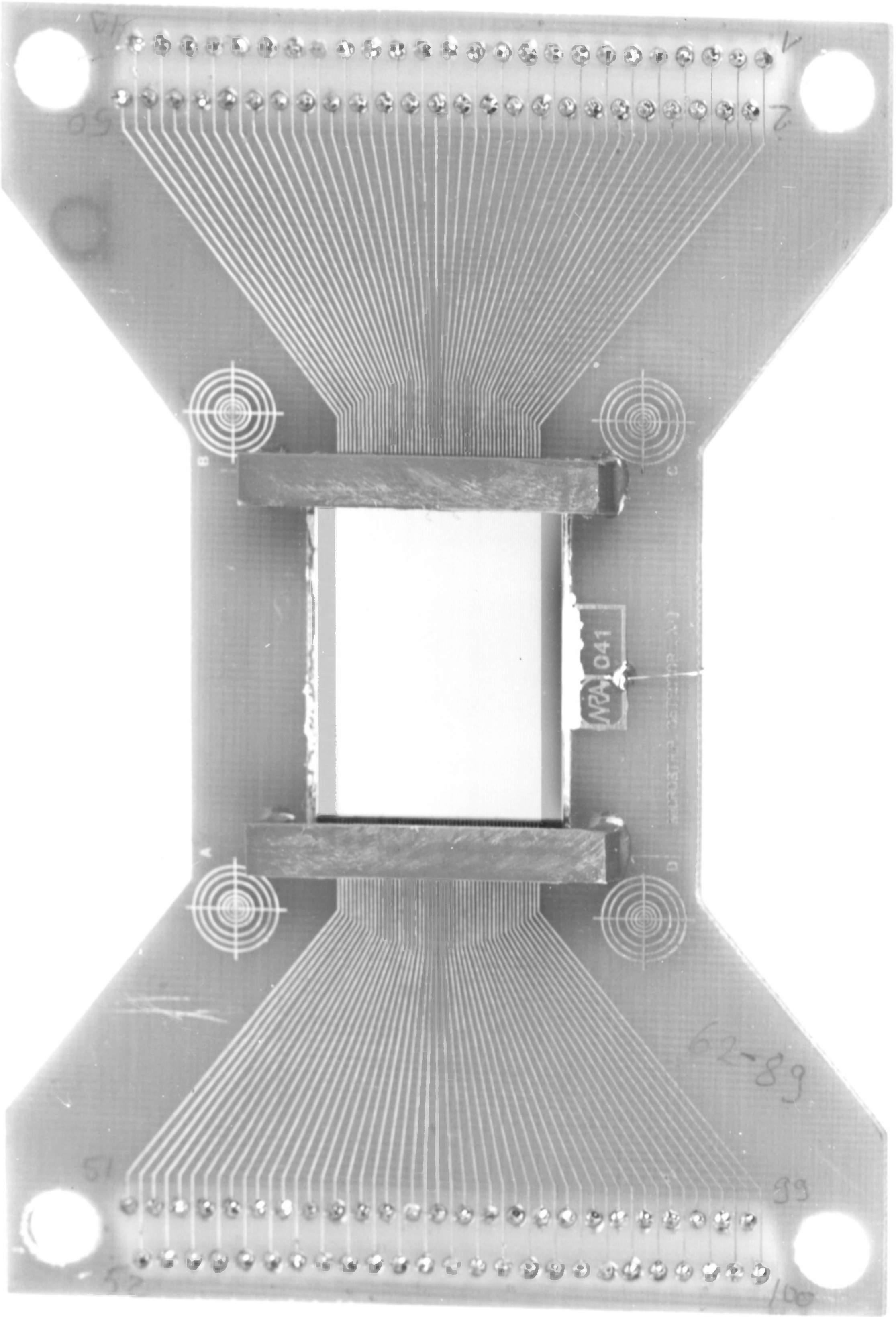
49
1
50
2
B
C
041
A
D
62-89
51
99
52
100

4.2.1 Experimental Details

The severe multiple scattering in silicon of low-energy beta radiation precludes the use of radioactive sources to test microstrip detectors, as a single source particle can produce signals on several adjacent strips. Microstrip detectors can only be tested realistically in a beam of high-energy particles, so the tests were carried out in the C13 beamline of the CERN PS using negatively-charged pions of 10 and 16 GeV/c at an intensity between 10^4 and 5×10^4 per 0.3 s burst. The experimental arrangement is sketched in figure 4.2.

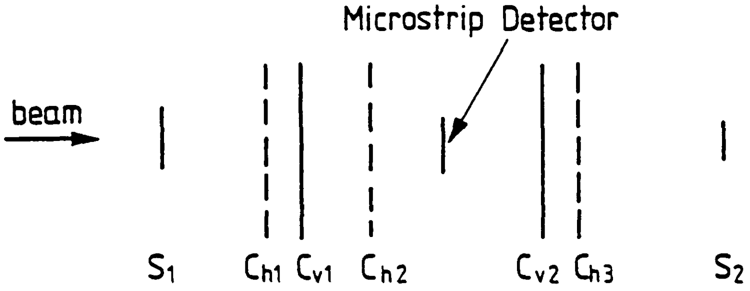

Figure 4.2

The overlap of two scintillators (S_1 and S_2) provided the geometrical acceptance, defining a 10×20 mm^2 zone on the horizontally-disposed strips of the silicon detector, which was mounted between a series of centroid wire chambers [48]. The chambers were equipped with centre-of-gravity read-out on five planes of cathode strips, three of them disposed horizontally (C_{hi}) and two vertically (C_{vi}).

The intrinsically small signal from a microstrip detector element necessitates a preamplifier as the first component of each signal channel. A preamplifier also serves to match the high impedance of the detector by presenting a low output impedance to the successive stages in the electronic chain. The preamplifiers employed have been developed by Pierre Jarron

[49][50] and were located immediately next to the detector board so as to minimize the capacitance at their input and, thus, any degradation of the signal-to-noise ratio. They are wideband current-sensitive amplifiers in order to make maximum use of the fast signal characteristics of thin silicon detectors and they employ low-noise bipolar microwave transistors, rather than field-effect ones, in order to achieve a high rate capability and low power consumption. A better immunity to crosstalk is obtained with a low input impedance current-sensitive preamplifier and, unlike with a charge- or voltage-sensitive preamplifier, no shaping filter-amplifier is needed [49]. However, the capacitance between detector strips leads to a mutual influence between preamplifiers and creates, apart from crosstalk, oscillation problems. For this reason, the preamplifiers for adjacent strips were connected at opposite ends of the detector under test. The preamplifiers had a current gain of 800 and the rise-time was about 15 ns for a signal of 40 ns duration.

The preamplified signals were sent to standard LeCroy 612AM linear amplifiers. The resulting signals, and those from the centroid chambers, were recorded by LeCroy 2249A current-integrating analogue-to-digital converters (ADC's). These ADC's were gated by a 50 ns signal derived from the trigger.

Two types of trigger were employed during data-taking. The "counter trigger" was generated by the passage of a beam particle through the microstrip detector and was defined as the coincidence of the two scintillator counters, $S_1.S_2$. This trigger was used to study the detection efficiency of each silicon device. The "strip trigger" was obtained by discriminating the amplified signal from one particular detector strip, at a threshold of three standard deviations of the noise distribution of that channel, and placing this in coincidence with the counter trigger. The strip trigger permitted the study of the energy-loss region between the noise distribution and the single particle energy-loss distribution of the trigger strip. This region is of particular interest because any charge sharing between the trigger strip and its neighbours would be indicated by signals of smaller amplitude than those due to particles "hitting" the trigger strip alone.

The trajectory of a beam particle, inside the acceptance area defined by the S_1 and S_2 counters, was reconstructed off-line using the information from the centroid chambers. C_{v1} and C_{v2} gave the track definition along the horizontal y-axis and C_{h2}, C_{h3} provided that along the vertical z-axis. The vertical resolution was determined by adding the C_{h1} information and proved to be about 110 μm.

4.2.2 Detection Efficiency

A beam particle was considered to be sensed by the silicon detector under test when either (i) the signal from a single strip was greater than three standard deviations above the mean of the pedestal noise distribution of that channel; or (ii) two (or more) adjacent strips simultaneously gave a signal greater than three standard deviations above their noise pedestals; and (iii) the difference between the z-value at the centre of the strip hit and the z-coordinate determined from the reconstructed trajectory was less than 500 μm. Whenever condition (ii) was satisfied, a clustering method was used to obtain the z-value of the "double hit".

A detector's efficiency may be defined, for a sample of events in which a particle penetrates the active volume of the detector, as simply the fraction of the events which is sensed. In this study, events were selected provided that the reconstructed pion trajectory passed through the central 8×20 mm^2 of the silicon detector and had an associated uncertainty in the vertical direction of less than 300 μm.

The ion-implanted detector, D, which showed no evidence of a charge dividing mechanism (see section 4.2.3), was found to have an efficiency of 99.1 ± 1.0 %. This measurement indicates that a particle crossing an inter-strip region will be sensed by the nearest strip, since there were no sizeable dead zones and no significant sharing of charge. The surface-barrier devices did display the double hit phenomenon. Detector C (with 60 mm long strips on the rear side) was 98.0 ± 1.0 % efficient, while the efficiency of detector A (which had 30 mm long strips on the rear side) was greater than 95%. A better estimate of this last efficiency could not be made because only the C_{hi} cathode planes were operational during data-taking.

4.2.3 Single Particle and Charge-divided Energy-loss Spectra

A "single hit" is registered when a beam particle crosses a strip or that part of the inter-strip region where no charge division occurs (see section 4.2.4), i.e. only one strip produces a signal. Such events were selected from data taken with one strip in the trigger by demanding that both strips adjacent to the trigger strip gave a signal less than three standard deviations above their noise pedestals.

The single particle energy-loss distributions so obtained are shown in figure 4.3 together with their fitted curves. The four figures, 4.3(a), (b), (c), (d), apply to detectors A, B, C and D, respectively. The distributions have each been fitted by a Landau distribution convolved with a Gaussian one and a summary of the fitted parameters is given in table 4.2. The most-probable energy loss of the Landau component has been normalized to 116 keV in the 400 μm detectors and to 84 keV in the 300 μm detector. (For detectors this thin, the energy-loss does not depend linearly on thickness.) The full width at half maximum height (FWHM) of each Landau contribution is in reasonable agreement with that expected [51], providing a posteriori justification for the energy scales assumed. The total FWHM of each

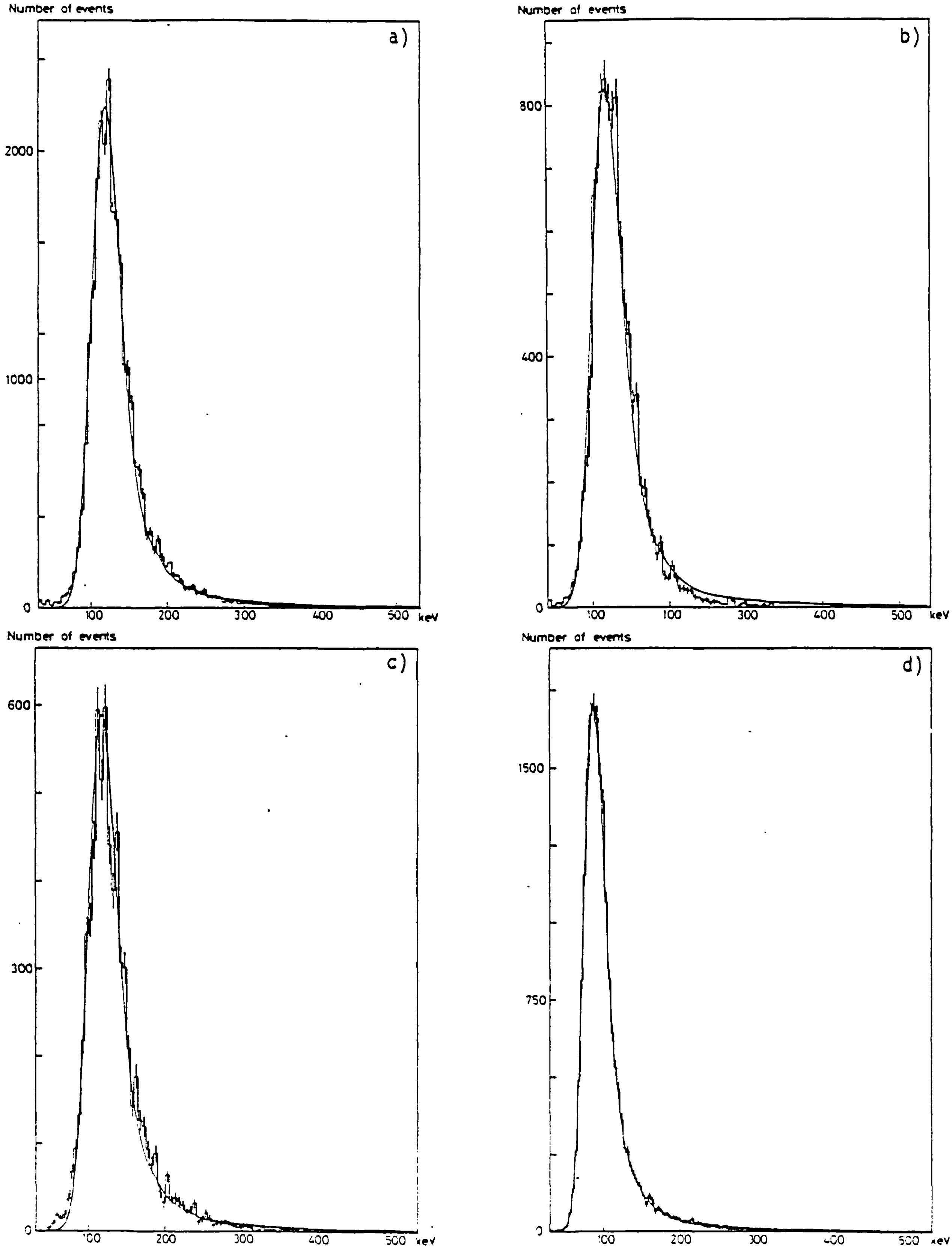
Number of events
a)
2000
1000
0
100
200
300
400
500
keV
Number of events
b)
800
400
0
100
100
300
400
500
keV
Number of events
c)
600
300
0
100
200
300
400
500
keV
Number of events
d)
1500
750
0
100
200
300
400
500
keV

Figure 4.3

Detector	Fitted Parameters		Total FWHM/keV (Noise Subtracted)	Measured Noise FWHM /keV	Beam Momentum/ GeV/c
	Landau FWHM /keV	Total Gaussian FWHM/keV			
A	26.8 ± 2.0	32.4 ± 2.0	35.4 ± 2.0	22.6 ± 1.0	10
B	27.5 ± 1.5	32.9 ± 1.5	36.1 ± 1.5	23.2 ± 0.5	10
C	26.8 ± 2.0	32.5 ± 2.0	35.0 ± 2.0	22.3 ± 1.0	10
D	20.9 ± 1.0	23.1 ± 1.0	27.9 ± 1.0	13.9 ± 0.4	16

Table 4.2

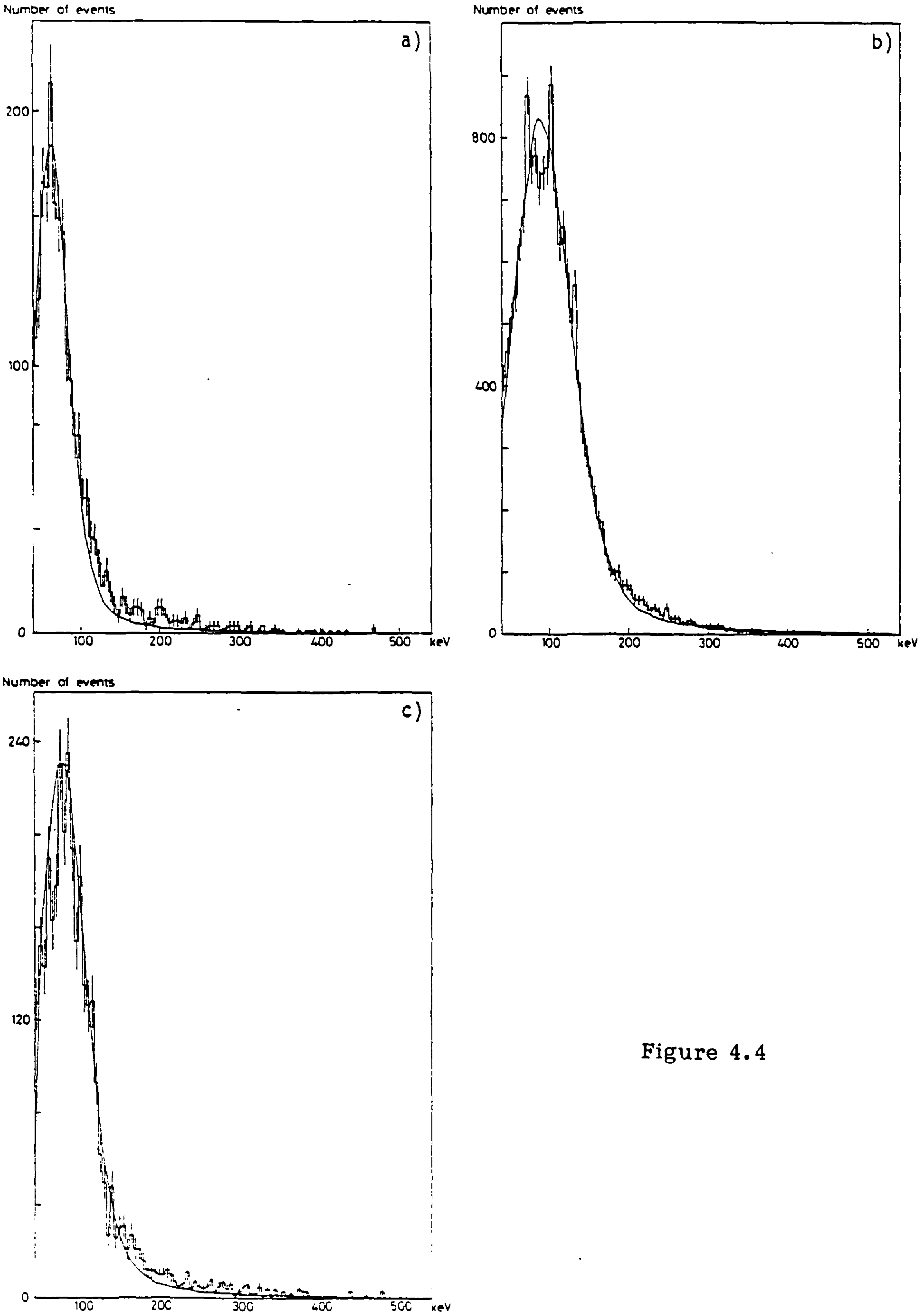
Number of events
a)
200
100
0
100
200
300
400
500
keV
Number of events
b)
800
400
0
100
200
300
400
500
keV
Number of events
c)
240
120
0
100
200
300
400
500
keV

Figure 4.4

distribution, once the noise contribution has been subtracted, cannot be explained by the Landau contribution alone and, as expected, the extra Gaussian component of the improved energy-loss (IEL) distribution must be introduced (see the appendix). The dependence of the total FWHM on detector thickness is also as predicted [51].

If, for the surface-barrier detectors, the off-line constraint imposed on the signals from the strips adjacent to the trigger strip is relaxed, then the low-energy tail of the single particle energy-loss distribution for that trigger strip becomes merged with the charge-divided distribution due to double hits. When only the double hit events were selected (by demanding that the trigger strip and one of those adjacent to it both yielded a signal > $3\sigma_{noise}$), the resulting charge-divided distribution could again be fitted by a Landau distribution convolved with a Gaussian one, but its total Gaussian content could not be explained sufficiently by the contributions due to noise and the Gaussian part of the improved energy-loss distribution. In figures 4.4(a), (b), (c) the double hit energy-loss distributions are shown for detectors A, B and C, respectively. The excess events above each fitted curve in the higher energy-loss region indicate that the double hits do not all originate simply from charge division, but that a significant proportion of them involve an extended delta ray or photon shower. Triple hits occurred in less than 0.5% of the events and may be explained by beam particles with an accompanying delta ray or converting photon.

In the limit of the $3\sigma_{noise}$ cut, no double hit events were observed for the ion implanted detector.

4.2.4 The Ratio of Double to Single Hits

The ratio, R, of the number of double to single hit events may be understood by introducing a zone, of width X_{eq}, defined as that part of the inter-strip region where a normally incident particle gives rise to charge division. If the pitch is 200 μm, then the width of the single hit zone is $200\mu m - X_{eq}$, and

$$X_{eq} = \left(\frac{R}{2+R}\right).200\ \mu m \qquad (4.1)$$

assuming a flat beam distribution. In table 4.3 experimental values of R and the corresponding values of X_{eq} are listed.

Detector	R	$X_{eq}/\mu m$	Inter-strip Width/μm
A	0.301	26	80
B	0.928	63	100
C	0.504	40	120

Table 4.3

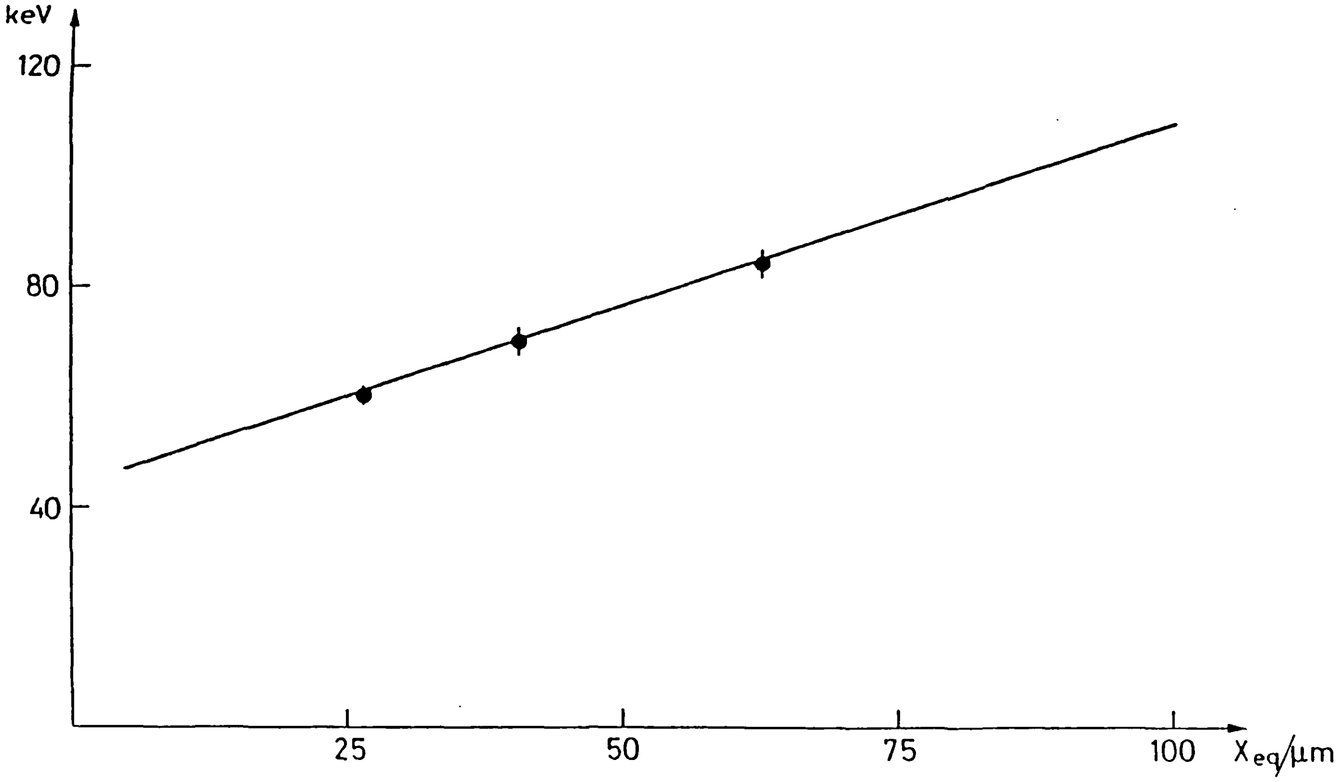

Figure 4.5

It was found that the peak position of the charge-divided distribution for each of the surface-barrier detectors was not simply half of that of the single particle distribution, but varied linearly with X_{eq} (see figure 4.5). This implies that the phenomenon of charge division involves a resistive layer at the surface of the inter-strip region.

4.2.5 Concluding Remarks

It will be seen from table 4.2 that the noise performances of all of the surface-barrier detectors were roughly the same, even though detector C was twice the length of detectors A and B. This was because the input capacitance presented to the preamplifiers by a microstrip detector is dominated by the coupling capacitance between strips and the capacitance of the fan-out printed circuit board. The main difference between detectors A and B was that detector A (with strips on the rear side) had to be totally depleted before position-sensitive signals were obtained, whereas detector B (with strips on the junction side) was already useable at 10 V reverse bias.

The noise performance of the ion-implanted detector was better than that of any of the surface-barrier ones.

The ion-implantation technique was finally chosen for the NA14 vertex detector because not only is it known to yield reproducible and stable results, but also, for incoming particles at normal incidence, it was found to produce no charge division between adjacent strips. This property is useful in the active target and in the microstrip detector stack, where only the fact that a strip has registered a hit is important.

4.3 Radiation Damage

The disruptive effect of intense high-energy radiation on the silicon lattice can lead to performance degredation in silicon detectors and, consequently, it was important to establish the limits imposed by radiation damage on the lifetime of the NA14 vertex detector.

The most common type of radiation damage takes the form of single vacancies created by the excitation of a silicon atom from its lattice position, to which it is bound with an energy of approximately 25 eV. The vacancy site, together with the atom displaced to an interstitial position, constitute a "Frenkel defect" [52] and can trap ordinary charge carriers. The vacancies are mobile above 55 K and are able to migrate through the crystal and associate with impurity centres or with other vacancies to form stable defect pairs. These point defects introduce deep energy levels in the silicon band gap, which trap charge carriers and are very effective in promoting recombination. If the defects preferentially trap one charge carrier type, then the space charge due to ionized dopant impurities may be modified and hence the depletion layer thickness altered.

When enough defects have been formed, the carrier lifetime and the charge collection efficiency are reduced significantly, so that the energy resolution of the detector is degraded due to fluctuations in the amount of signal charge that is lost. Defects also act as generation centres and lead to an enhancement of the bulk leakage current (although changes also brought about in the surface leakage may be even more significant). Correspondingly, the detector noise is increased and the energy resolution further degraded. Some annealing of the radiation damage may occur over long periods of time, but it is essentially permanent.

A study has been conducted [53] to determine the effects of radiation damage on ion-implanted silicon detectors. The general results can be expected to be equally valid for surface-barrier and thermally-diffused silicon detectors, since the physical damage mechanisms seem not to depend upon the nature of the junction. Two detectors were used, although one was not irradiated but kept merely as a control. Each detector had an active area of 10×10 mm^2 and a thickness of 300 μm, but neither was equipped with strips for position sensing. They were manufactured by Enertec, Strasbourg.

The irradiation was performed using secondary hadrons produced in a 33 mm long iridium target by a 24 GeV/c proton beam from the CERN PS. Lithium fluoride thermoluminescent detectors were used to measure the flux profile of the secondary beam and a position for the detector was chosen, on the basis of this measurement, at an angle of 15 mrad to the axis of the primary proton beam at the centre of the production target. The exposed detector was then outside the diffraction peak of the secondary beam, at a point where the intensity was 0.5% of its maximum and varied by less than ±20% across the surface of the device. The secondary beam passed through a bending magnet which imposed a lower momentum limit of 3 GeV/c on the charged particles incident upon the detector. The charged particles comprised some 70% protons, 30% pions and less than 1% kaons, mostly in the energy range 5 to 24 GeV over which their nucleon interaction cross-sections are roughly constant. Evaporative neutrons originating from the break-up of target nuclei were estimated to make up less than 1% of the flux at the detector position.

One of the silicon detectors was irradiated in a series of four exposures in which it was subjected to successive total fluences of 4.4×10^{12} cm^{-2}, 1.2×10^{13} cm^{-2}, 1.6×10^{13} cm^{-2} and 8.3×10^{13} cm^{-2}.

4.3.1 Bias Voltage and Leakage Current

Maximum signal amplitude is only obtained from a silicon detector when the reverse bias applied to it is sufficient not only to produce a depletion layer that extends from the junction to the rear contact, but also to create a field within the depletion region such that the charge collection time is shorter than the carrier lifetime. If the latter condition is not met, then the trapping and recombination of charge carriers leads to signals of lower pulse height and greater duration. This effect was observed in the irradiated detector, indicating that radiation damage had reduced the carrier lifetime to a point where a field increase was required to achieve full charge collection within the same time.

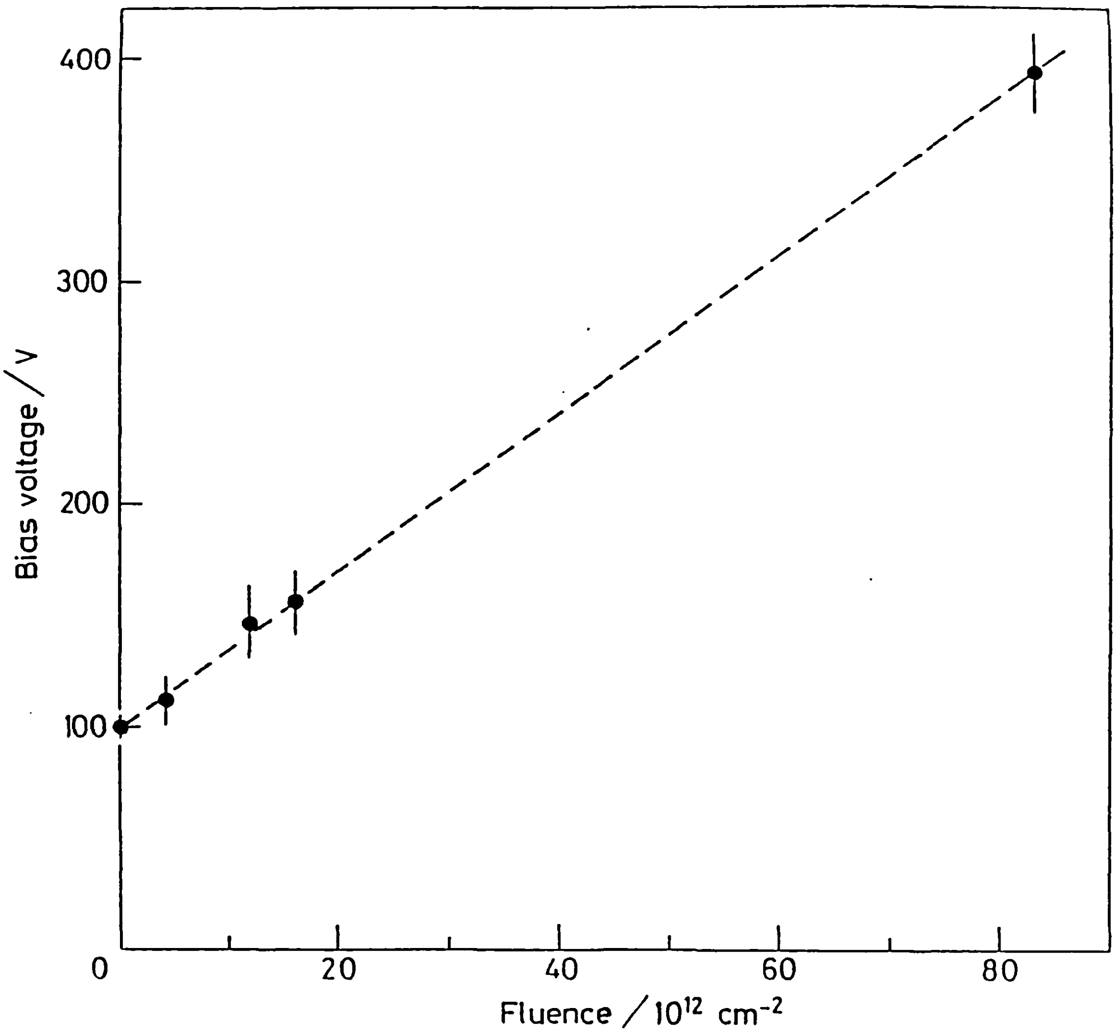

Figure 4.6

The depth of the depletion region was also affected by radiation damage. The occurrence of total depletion was determined by observing the signals produced by alpha particles impinging on the rear surface of the irradiated detector from an ^{241}Am source. The 5.48 MeV alpha particles from this source have a range of just 28 μm in silicon (see figure 3.1), so that total depletion was indicated when the pulse height they produced reached a plateau as a function of the reverse bias applied to the detector. It was found that, after each exposure, the bias voltage had to be increased before total depletion was achieved (see figure 4.6). The necessary increase remained very stable with time after irradiation and is consistent with a linear dependence on fluence.

The initial leakage current of the irradiated detector was 16 nA at a total depletion bias of 100 V. Immediately after the first exposure, this had increased by a factor of 750 to 12 μA. The leakage current fell quite rapidly with time after irradiation, but each subsequent exposure increased its magnitude.

4.3.2 Detector Performance

The response of the irradiated detector to high-energy ionizing particles was tested in the C13 beamline of the CERN PS. The momentum of the incoming pions was 10 GeV/c and their intensity of the order of 10^4 per 0.3 s burst. The overlap of two scintillators, one on each side of the silicon detector, defined the geometrical acceptance of the beam. The signal pulses from the detector were sent to a standard ORTEC-125 charge-sensitive preamplifier and thence to a modified version of an ORTEC-472 spectroscopy amplifier. The shaped output pulses, which had a rise-time of 200 ns and a duration of 600 ns at their base, were recorded by a LeCroy 2249A current-integrating ADC. The ADC was gated by a 40 ns signal derived from the coincidence of the two scintillator counters.

The irradiated detector was tested after each exposure and, using physically the same electronics, the control detector was also tested each time in order to provide a reference measurement. The applied reverse bias was always that required for total depletion.

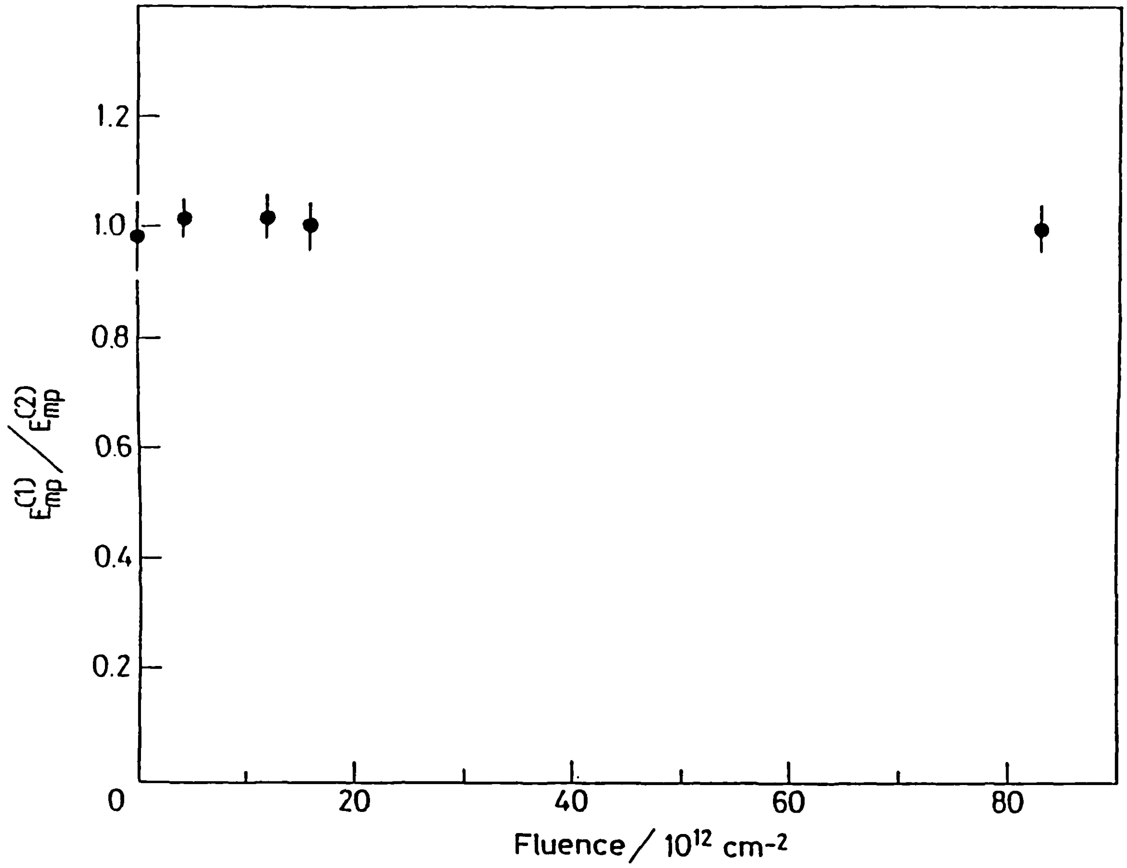

Figure 4.7

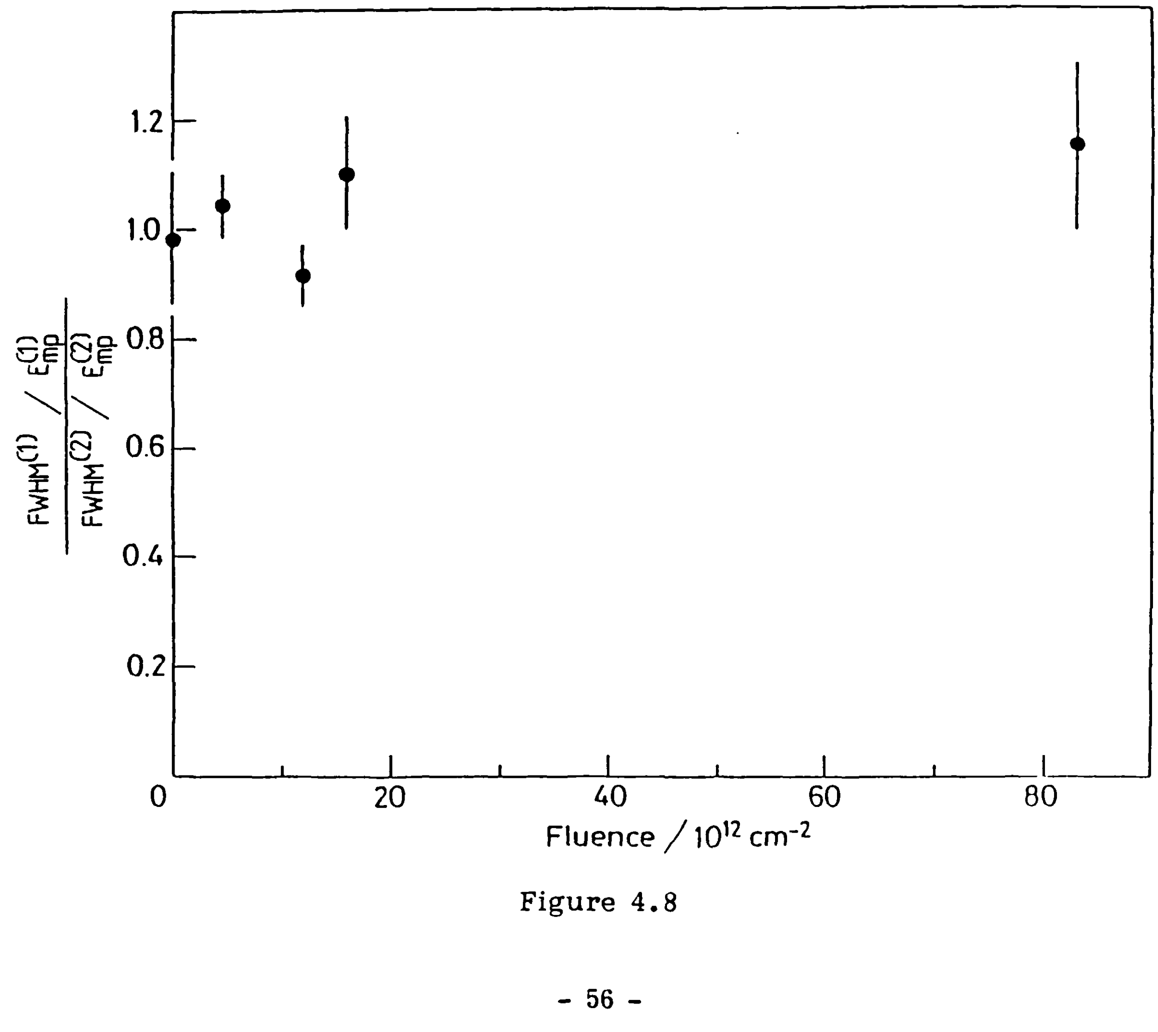

Figure 4.8

Figure 4.7 shows that the most-probable energy loss, $E_{mp}^{(1)}$, as measured in the irradiated detector is constant (within the errors) relative to that, $E_{mp}^{(2)}$, in the control detector, irrespective of the fluence. That is, the peak position of the pulse height distribution for the irradiated detector was not significantly shifted after irradiation, once the contribution due to noise had been subtracted. Likewise, figure 4.8 shows the constancy of the FWHM of the (noise-subtracted) distribution of the energy loss sensed by the irradiated detector. These two results indicate that the detector responded in the same way to the same energy loss provided that the applied reverse bias was increased sufficiently to ensure total depletion and restore full charge collection efficiency after irradiation.

Before irradiation, the pedestal noise distribution for the detector and its associated electronics was Gaussian with a FWHM of 10.5 ± 0.8 keV (assuming the most-probable energy loss according to pure Landau theory to be 84.0 keV in 300 μm of silicon). Since the leakage current was found to increase with fluence, a concomitant increase in the FWHM of the noise was anticipated. However, because the induced radioactivity of the detector housing led to a counting rate high enough to saturate the electronics chain, no measurements could be made in the test beam immediately after the detector had been irradiated. Consequently, as the leakage current after irradiation was strongly time-dependent, no quantitative conclusions can be drawn about the variation of the energy resolution with fluence. In general though, the use of fast electronics will suppress the low-frequency components of the noise and reduce the seriousness of the implications of an increase in leakage current.

4.3.3 Concluding Remarks

The results presented here establish that an ion-implanted silicon detector may be operated effectively even after its irradiation at fluences of almost 10^{14} cm^{-2}, but that the bias voltage applied to it must be increased if the charge collection efficiency is not to be impaired. The accompanying increase in the leakage current may be drastic and, due to the problem of power dissipation, could impose an ultimate limit on the packing density achievable in an active target system.

On the basis of this study, it may be inferred that none of the deleterious effects of radiation damage would appear in the NA14 vertex detector until well after 10 periods of running at 100% SPS efficiency with 10^8 electrons/s in the BEG.

4.4 Single Particle Energy Loss as a Function of Particle Energy [54][55]

The detection of charged particles by measuring their energy loss in thin silicon detectors has led to widespread study of the corresponding energy-loss spectrum [56][57][58]. This spectrum is given, to a first approximation, by the theories of Landau [59] and Vavilov [60], which are based on free electron scattering.

In order to observe the decay of short-lived particles, one must achieve high spatial resolution and be able to detect a change in charged particle multiplicity. This, in turn, implies the use of very thin silicon detectors and low-noise electronics. Under such conditions, significant deviations from the Landau and Vavilov descriptions are expected because of the importance of those interactions in which the electron binding energy cannot be neglected. The result is a broadening of the observed distribution of energy losses which cannot otherwise be explained by experimental resolution or by additional sources of noise. This effect has been observed and, in some cases, attributed to the escape of delta rays from the detector [61] [62].

The theory can by improved by using a modified cross-section to take account of the electron binding energy in long-distance collisions. This approach is outlined in the appendix and the result is quoted (equation A.13) for the special case when the Landau and Vavilov theories may be taken to coincide. Since the Landau and Vavilov energy-loss distributions are practically indistinguishable when $\beta\gamma > 1$ for particles incident on a thin (<1 mm thick) silicon detector [56], the result is a useful one. (Here, β and γ are the usual relativistic parameters and are as defined for equations A.2 and A.6, respectively.)

In order to test the validity of the improved theory, energy-loss measurements have been made for protons in the kinetic energy range 254 to 1195 MeV at Saturne in Saclay and for protons and pions between 30 and 114 GeV at the CERN SPS.

4.4.1 Experimental Details

The momentum spread of the incident particles was never more than 0.1% during the measurements performed at Saturne and never more than 1% at the SPS. A well-defined momentum is important because any momentum spread leads to a broadening of the experimental energy-loss distribution, particularly at low momenta, and thereby masks the effect due to long-distance collisions.

Two ion-implanted silicon detectors were used, each having a continuous active area of 10×10 mm^2 and a thickness of 300 ± 5 μm. Total depletion of the detectors was achieved at reverse biases of about 100 V, with corresponding leakage currents of initially 16 and 20 nA. They were manufactured from 3.2 kΩcm n-type silicon by Enertec, Strasbourg.

The signal pulses from these detectors were sent to standard ORTEC-125 charge-sensitive preamplifiers. The preamplified signals were then sent to a modified version of an ORTEC-472 spectroscopy amplifier, in the case of the more upstream of the two detectors, and to an EG&G-474 timing filter-amplifier, in the case of the downstream detector. The ORTEC amplifier produced an output pulse with a 600 ns base and a 200 ns rise-time, while the timing filter-amplifier produced a pulse with a 100 ns base and a 50 ns rise-time. The instantaneous counting rate never exceeded 3 kHz in order to avoid the problems associated with pile-up.

The spacing between the two detectors was 4 cm and their active areas were well-aligned. A scintillator with an area of 5×5 mm^2 and a thickness of 5 mm was positioned 1 cm from the downstream detector. A beam particle was defined by the coincidence of the downstream detector and this small scintillator, the former being discriminated at a suitable level above the noise and the latter reducing the jitter to only a few nanoseconds. This trigger was shaped to provide a 40 ns gate for a Lecroy 2249A current-integrating ADC, where the signal pulses from the upstream detector were recorded.

The upstream detector, together with its special-purpose electronics, had a Gaussian noise distribution with a measured standard deviation of, typically, $\sigma_{noise} = 5.0 \pm 0.4$ keV. The precise value was determined by fitting a Gaussian to the pedestal noise distribution obtained immediately prior to each data-taking run at a new beam energy.

The original calibration of the energy scale for the entire system was performed using a 30 GeV π^- beam. (The most-probable energy loss for pions has no significant dependence on pion energy when $\beta\gamma > 50$ [61], a condition easily satisfied at 30 GeV.) The value of the most-probable energy loss according to pure Landau theory was assumed to be $\Delta_{mp} = 84.0$ keV in 300 μm of silicon. Thereafter, a ruthenium beta source was used for calibration purposes, once it had been determined that the value of Δ_{mp} for relativistic electrons is 86.8 ± 2.8 keV on the same scale that yielded the canonical value of 84.0 ± 2.8 keV for the 30 GeV pions.

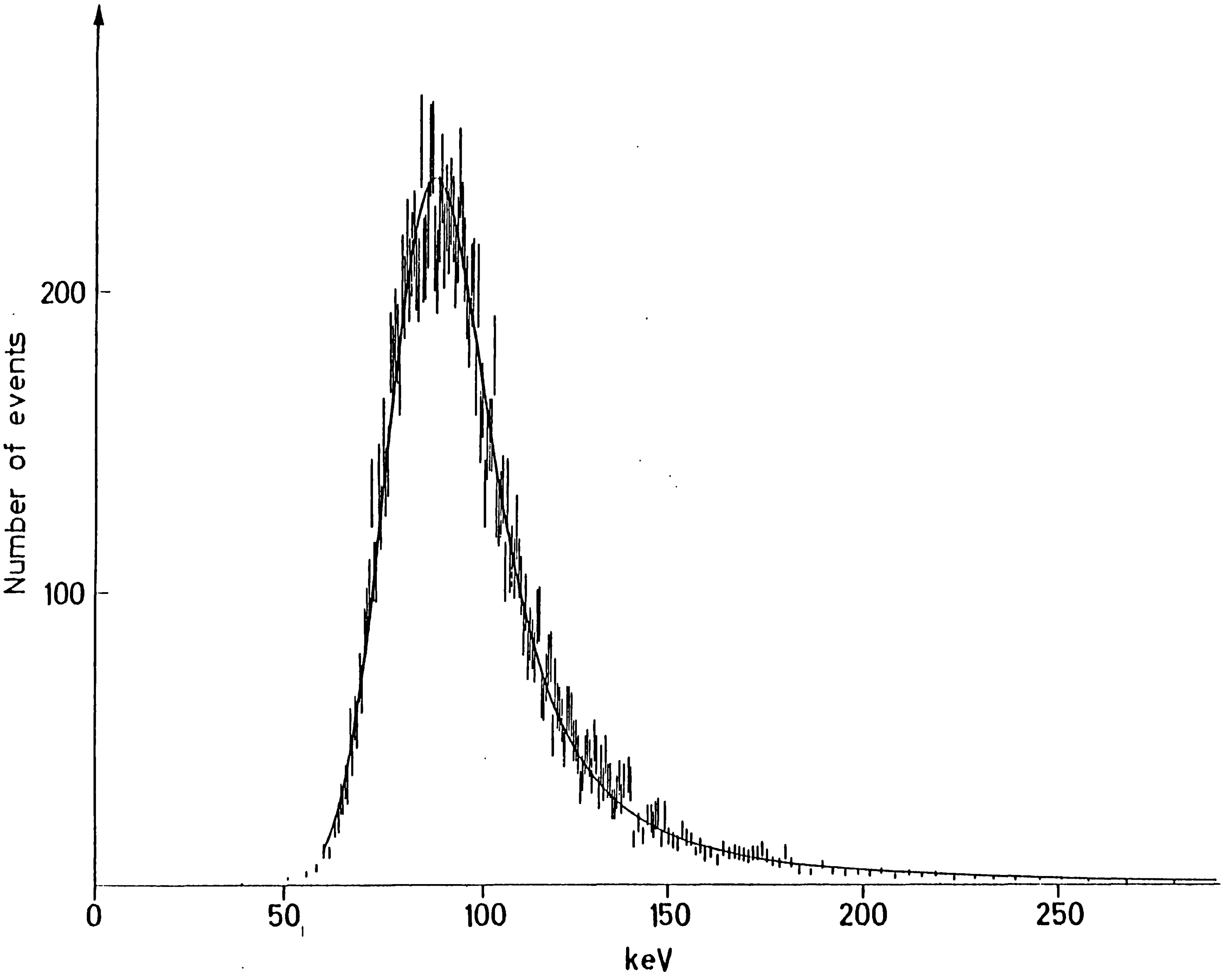

Figure 4.9

Figure 4.9 shows a calibration energy-loss spectrum and its corresponding fitted curve for relativisitic electrons from the ruthenium source. Relativistic electrons, i.e. those with a kinetic energy greater than 1 MeV, were selected by demanding that the beta particles from the source crossed both of the silicon detectors and the scintillator. This calibration was performed after each run at a new beam energy in order to monitor very closely the stability of the electronics.

4.4.2 Data Analysis and Discussion

The experimental energy-loss distributions for each kinetic energy and particle type were fitted to a Landau function convolved with a Gaussian one, as is described in section 5.1. The standard deviation of the Gaussian part combined the correction for long-distance collisions with the electronic and detector noise:

$$\sigma_{tot} = \surd(\sigma^2 + \sigma^2_{noise}) \qquad (4.2)$$

where $\sigma = \surd\delta_2$ (see the appendix).

Some deviations from the model were observed, as expected, in the high-energy tails of the lower energy distributions and were due to the neglect of escaping delta rays and to the effect of the maximum energy transfer to electrons disregarded by Landau theory. Consequently, in order to avoid any bias of the fitted parameters, the upper limit to which each experimental distribution was fitted was varied to obtain a good fit. The best fits had χ^2-probabilities of the order of 50% or better and were obtained by fitting up to $E_{cut} = \Delta_{mp} + b\Gamma$, where Γ is the FWHM of the distribution and the values of b were between 1.5 and 3.5. However, the values of the fit parameters, σ, ξ, and Δ_{mp}, at the best χ^2 did not differ, within the uncertainty of their determination, from those of the complete fit.

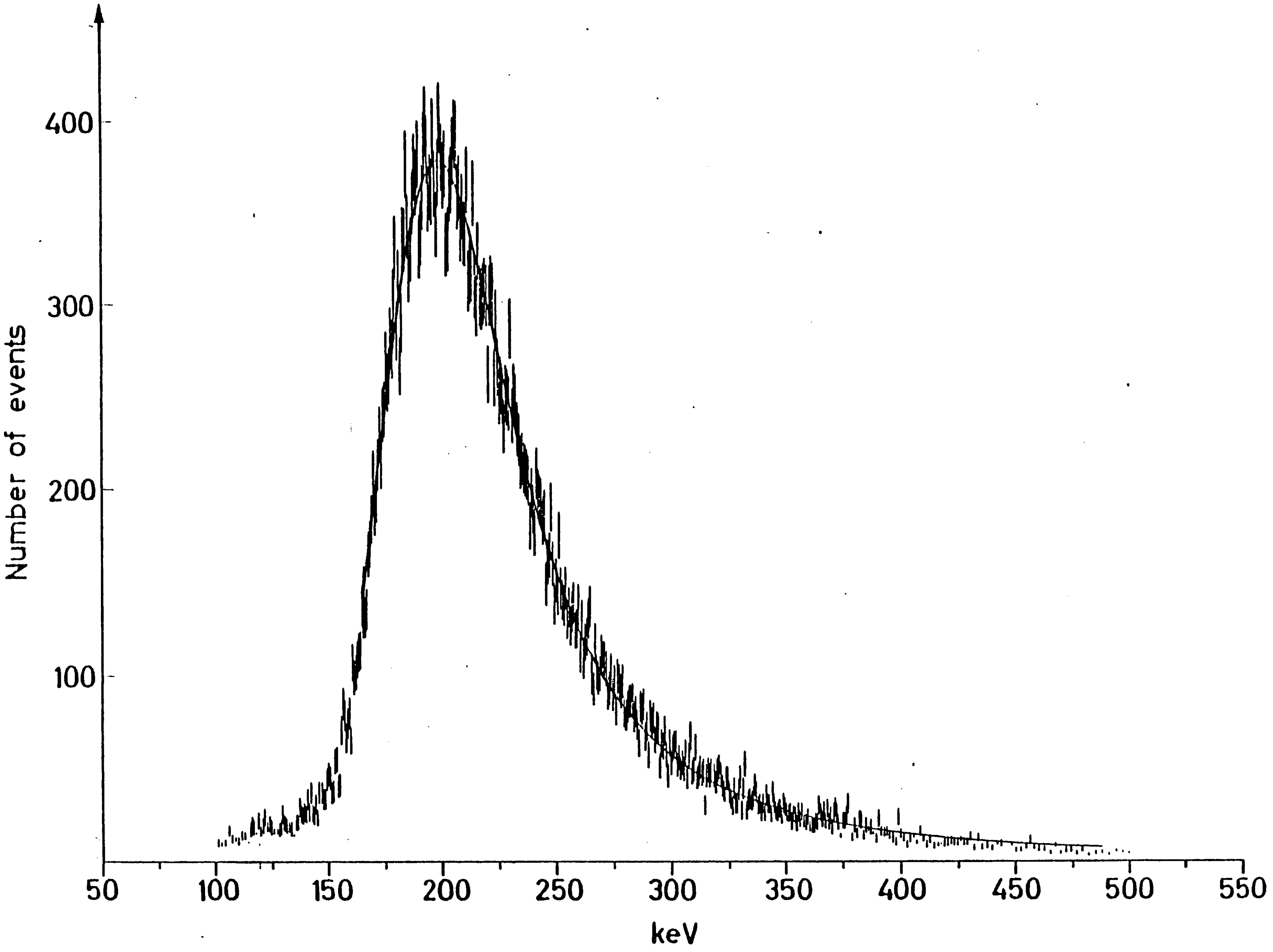
Number of events
400
300
200
100
50
100
150
200
250
300
350
400
450
500
550
keV

Figure 4.10(a)

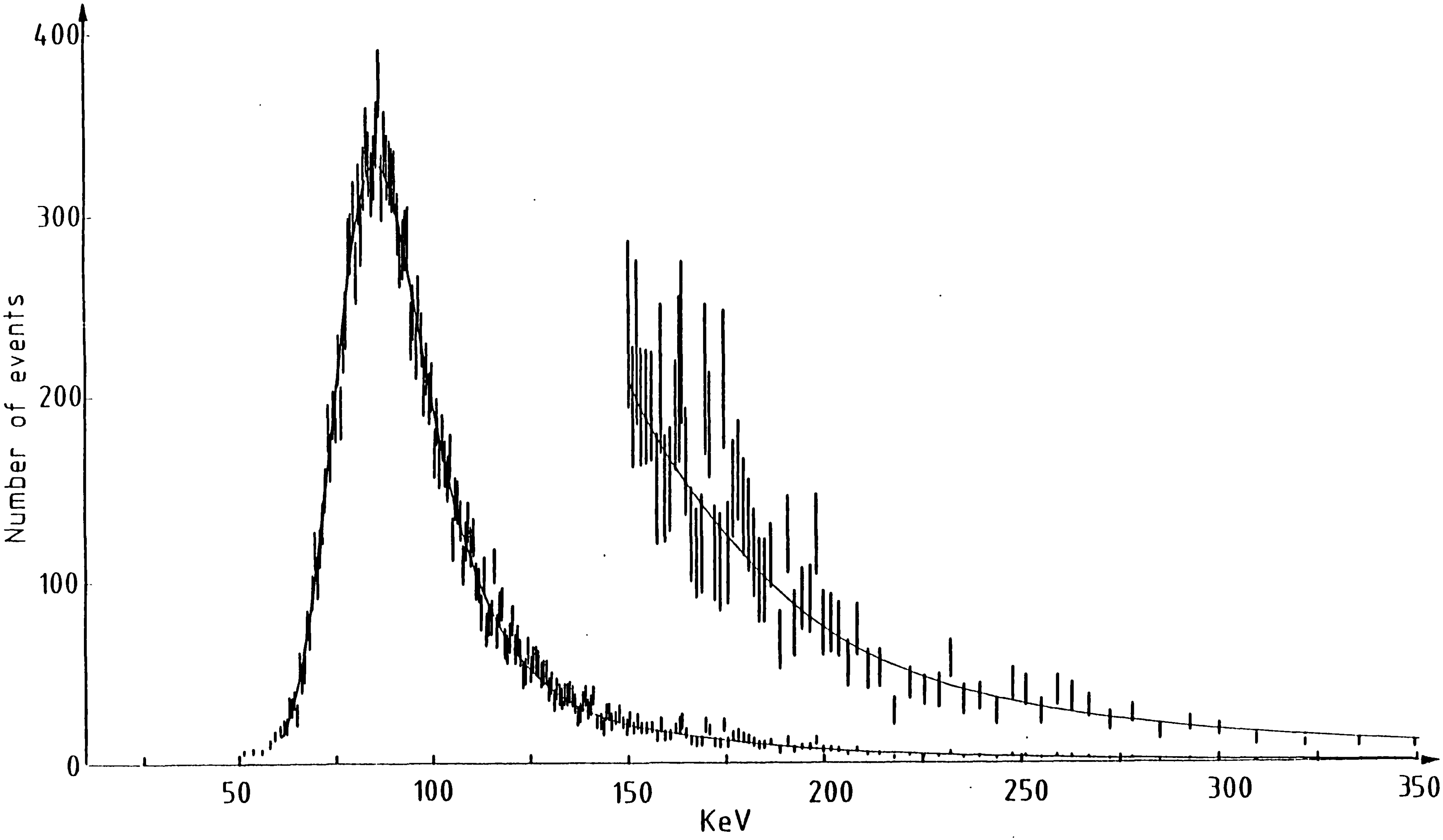
400
300
200
100
0
Number of events
50
100
150
200
250
300
350
KeV

Figure 4.10(b)

The complete fits to the experimental distributions obtained at the lowest and highest kinetic energies are shown as the continuous curves of figures 4.10(a) and (b), respectively. By eye, these are indistinguishable from the corresponding best-χ^2 fits. In figure 4.10(b) the high-energy tail of the distribution is shown with the vertical scale expanded by a factor of ten. The unequal bin widths resulting from the way in which the raw data were prepared (see section 5.1) are clearly visible.

The data taken at the SPS energies involved a contamination of about 1% from two particles simultaneously traversing the apparatus. This is consistent with the expected interaction rate in the upstream beam-defining scintillators. The resulting contribution to the fitted curves is too small to be noticeable by eye, even in figure 4.10(b). Two-particle contamination was neither expected nor observed in the other data.

Table 4.4 lists the best-χ^2 fitted values of σ, ξ and Δ_{mp} and the most-probable energy loss, E_{mp}, of the IEL distribution describing the data. The value of E_{mp} determined at the lowest kinetic energy is in agreement with the value quoted by Aitken et al. [56], once it is extrapolated to a detector thickness of 0.216 cm. The values of Δ_{mp} are in agreement with Landau theory provided the computation, which involves the Bethe-Bloch formula, takes into account the correction for the density effect. The shell correction term of the Bethe-Bloch formula is negligible over the entire kinetic energy range studied (see the appendix).

In figure 4.11 the values of the parameter σ are plotted together with the corresponding theoretical predictions for protons and pions according to Shulek et al. [63]. The errors shown take into account the uncertainty in determining the noise contribution to σ_{tot}.

The values of the parameter ξ are plotted in figure 4.12. The solid and broken lines are the curves calculated using equation A.2 for protons and

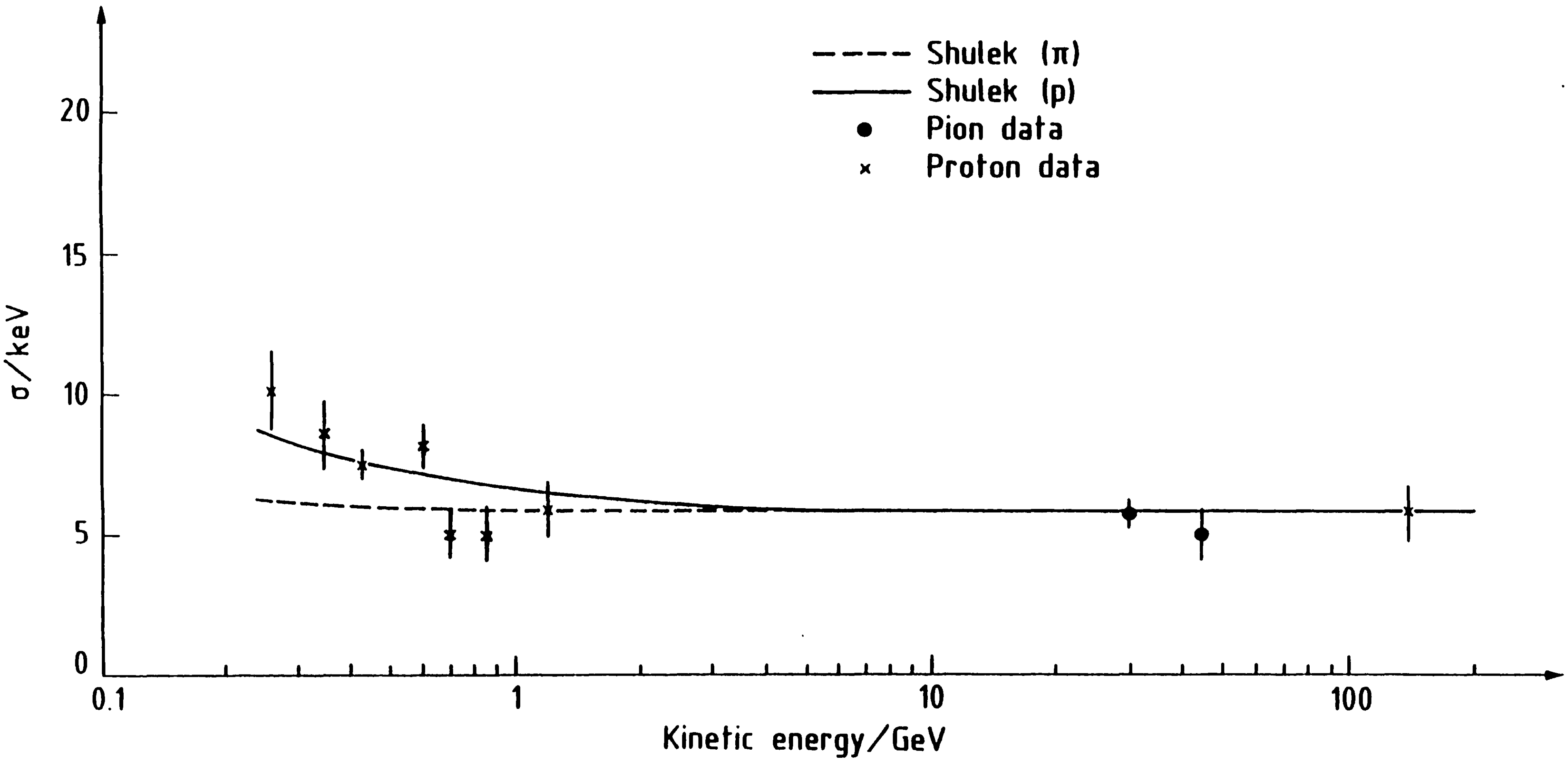
Shulek (π)
Shulek (p)
Pion data
Proton data
σ/keV
0
5
10
15
20
0.1
1
10
100
Kinetic energy/GeV

Figure 4.11

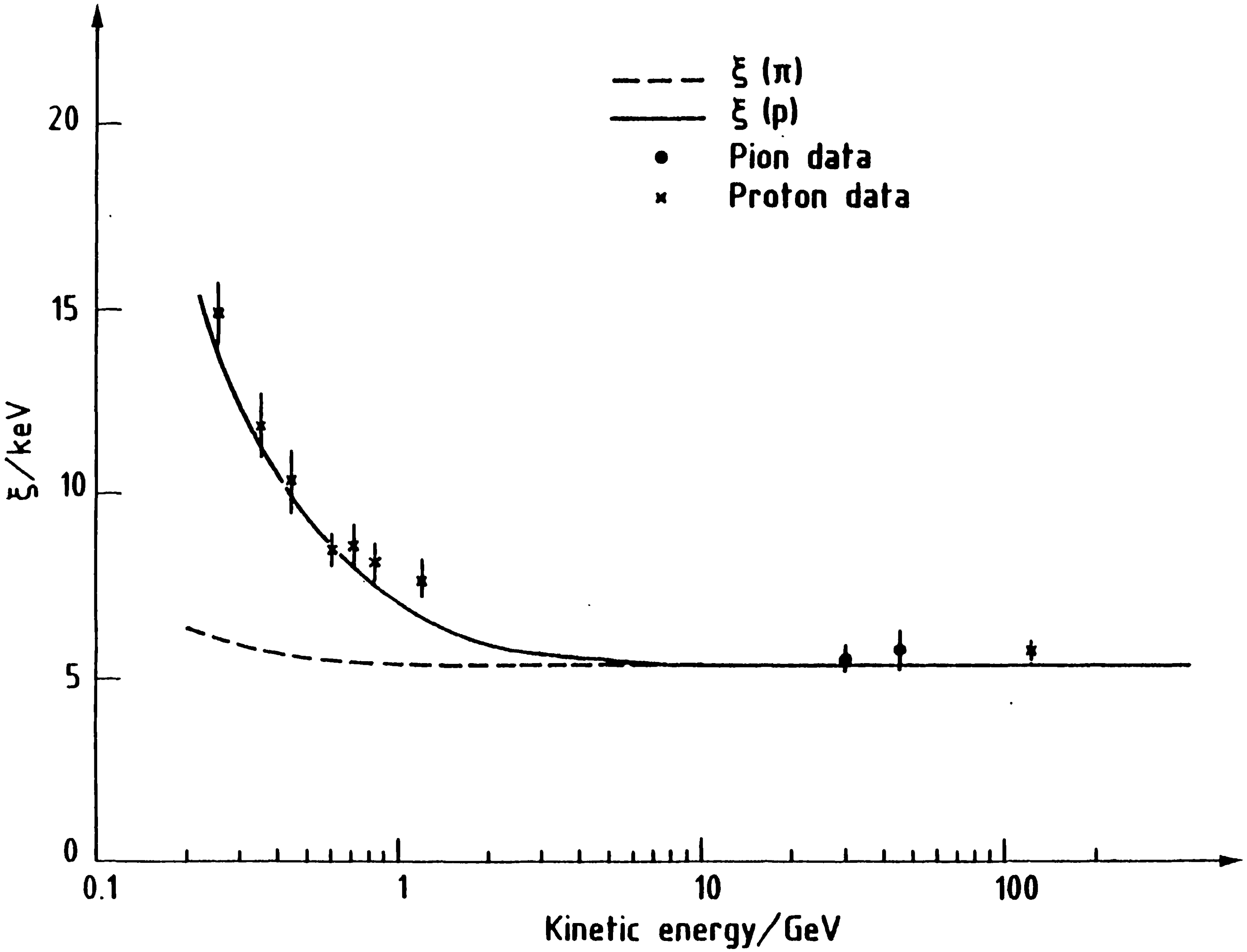
ξ (π)
ξ (p)
● Pion data
× Proton data
ξ/keV
0
5
10
15
20
0.1
1
10
100
Kinetic energy/GeV

Figure 4.12

pions, respectively, in 300 μm of silicon.

Kinetic Energy /GeV	σ/keV	ξ/keV	Δ_{mp}/keV	E_{mp}/keV
0.254	10.2 ± 1.3	15.0 ± 0.8	194.8 ± 5.8	196.2 ± 5.8
0.350	8.7 ± 1.3	11.9 ± 0.8	149.8 ± 4.5	152.3 ± 4.5
0.433	7.4 ± 0.6	10.4 ± 0.8	127.5 ± 3.8	130.8 ± 3.8
0.600	8.2 ± 0.7	8.5 ± 0.4	111.0 ± 3.4	113.5 ± 3.4
0.700	5.0 ± 0.9	8.6 ± 0.5	105.6 ± 3.2	108.1 ± 3.2
0.850	4.8 ± 0.9	8.2 ± 0.4	99.5 ± 3.0	101.2 ± 3.0
1.195	5.9 ± 1.0	7.6 ± 0.4	94.0 ± 3.0	97.2 ± 3.0
30	5.7 ± 0.5	5.5 ± 0.3	84.0 ± 2.8	85.6 ± 2.8
45	5.0 ± 0.9	5.8 ± 0.4	86.0 ± 2.8	88.8 ± 2.8
114	5.7 ± 1.0	5.6 ± 0.3	83.2 ± 2.8	85.5 ± 2.8

Table 4.4

The results of this investigation confirm that the collision-loss theories of Landau and Vavilov are inadequate for very thin absorbers. The effect of the atomic binding of electrons has been clearly observed and seems to be well-described by the IEL model, the Gaussian component of which appears compatible with the computations of Shulek et al.

4.5 Multi-particle Energy Loss [55]

The detection of a particle interaction or decay occurring inside the active target means identifying a step in charged particle multiplicity. This requires a complete knowledge of the energy-loss distributions at the multiplicities before and after the decay for all of the detector elements involved.

Consequently, in order to test the validity of the scaling laws implied by equation A.16, which enable the energy-loss distribution at any multiplicity to be derived given a knowledge of the single particle distribution, relativistic multi-particle energy-loss measurements have been made in the H3 beamline of the CERN SPS.

4.5.1 Experimental Details

Multi-particle production was achieved in a 5 mm long lead target using 115 GeV/c protons at an intensity 2×10^4 per 1.2 s burst. The experimental arrangement is sketched in figure 4.13.

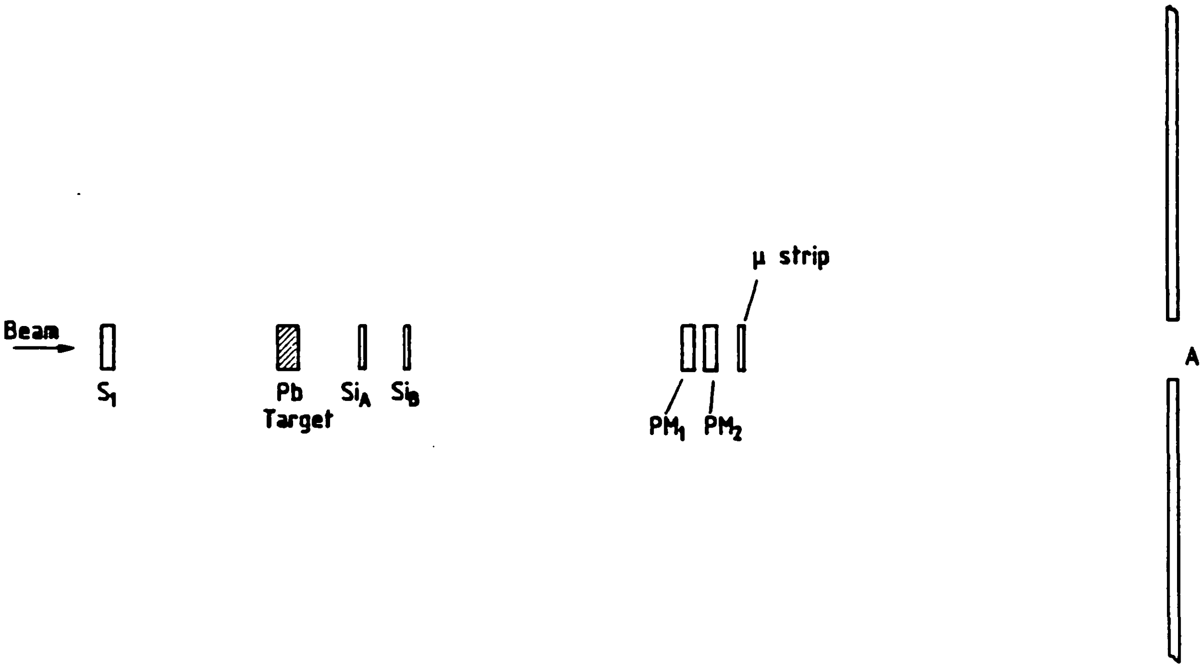

Figure 4.13

The geometrical acceptance was defined by a 16 mm diameter hole in a 40×40 cm^2 scintillator, A, located 20 cm downstream of the lead target. This scintillator was placed in anticoincidence with one upstream and two downstream ones, respectively S_1, PM_1 and PM_2, each 1×1 cm^2 in area. In this way, the acceptance was restricted to a forward cone of 40 mrad half-angle in order to reduce, to a few percent, the background of non-relativistic protons emanating from the target.1)

Two ion-implanted silicon devices, Si_A and Si_B, were mounted immediately downstream of the target. These detectors and their associated electronics have been described in section 4.4.1. In this experiment, however, the signal pulses from Si_B were discriminated at a threshold typically corresponding to the most-probable energy loss of one relativistic particle. By forming the trigger $T = S_1.PM_1.PM_2.\bar{A}.Si_B$, it could then be established when a beam particle had entered the lead target and at least one charged particle emerged in the very forward direction.

An ion-implanted microstrip detector positioned upstream of the anticoincidence scintillator was used to examine the multiplicity of the interactions occurring in the target. This device was 300 μm thick with fifty strips horizontally disposed over an active area of 10×30 mm^2. The charged particle multiplicity of an interaction was determined from the height of the pulse formed by linearly summing the discriminated signals from all of the strips. When the pulse height corresponded to a multiplicity of less than four, the event was accepted. This majority logic was gated by T, allowing events to be selected in which up to three secondary particles traversed Si_A, the detector registering the particles' energy loss. A single beam particle could be recorded, provided that it deposited sufficient energy in Si_B. A contamination from four and even five particles was also expected due to the finite spatial resolution of the microstrip detector and to a few unconnected strips.

---

1) The momentum of these slow protons is in the range 300 to 1000 MeV/c. They are produced with an angular distribution which is roughly flat up to 700 mrad about the beam direction. One such quasi-direct proton is produced, on average, per incoherent diffractive interaction. The coherent processes are contained in a slightly narrower cone about the beam direction.

4.5.2 Data Analysis and Discussion

The procedure used to fit the experimental distributions, which combined energy-loss spectra for all multiplicities up to five, is described in section 5.2. The χ^2-probabilities of the fits obtained varied between 45 and 85%.

The Gaussian contribution to the experimental distributions due to noise was determined before, during and after data-taking. The standard deviation of the pedestal noise distribution was found to be 4.3 ± 0.2 keV in each case.

By varying the discriminator threshold associated with the detector Si_B, the percentage of triggers due to single particles could be modified. In table 4.5 the fitted values of F(n) (for n = 1 to 5), σ and ξ are given for three different data samples. The energy-loss distribution for the second case listed is shown in figure 4.14 and has been fitted above 60 keV.

F(1) %	F(2) %	F(3) %	F(4) %	F(5) %	ξ /keV	σ /keV
52.2±0.6	13.5±0.4	25.5±0.6	7.8±0.5	1.0±0.4	5.9±0.4	4.9±0.6
40.9±0.5	18.6±0.5	30.5±0.6	8.7±0.6	0.8±0.5	6.1±0.6	6.6±1.7
7.6±0.4	25.2±0.8	49.3±1.3	15.6±1.1	2.3±0.9	6.2±0.5	6.6±1.2

Table 4.5

The results are in reasonable agreement with the expected values of σ = 5.76 keV (from equation A.15) and ξ = 5.35 keV (from equation A.2), although the fitted values of ξ appear to be systematically too high. A slight

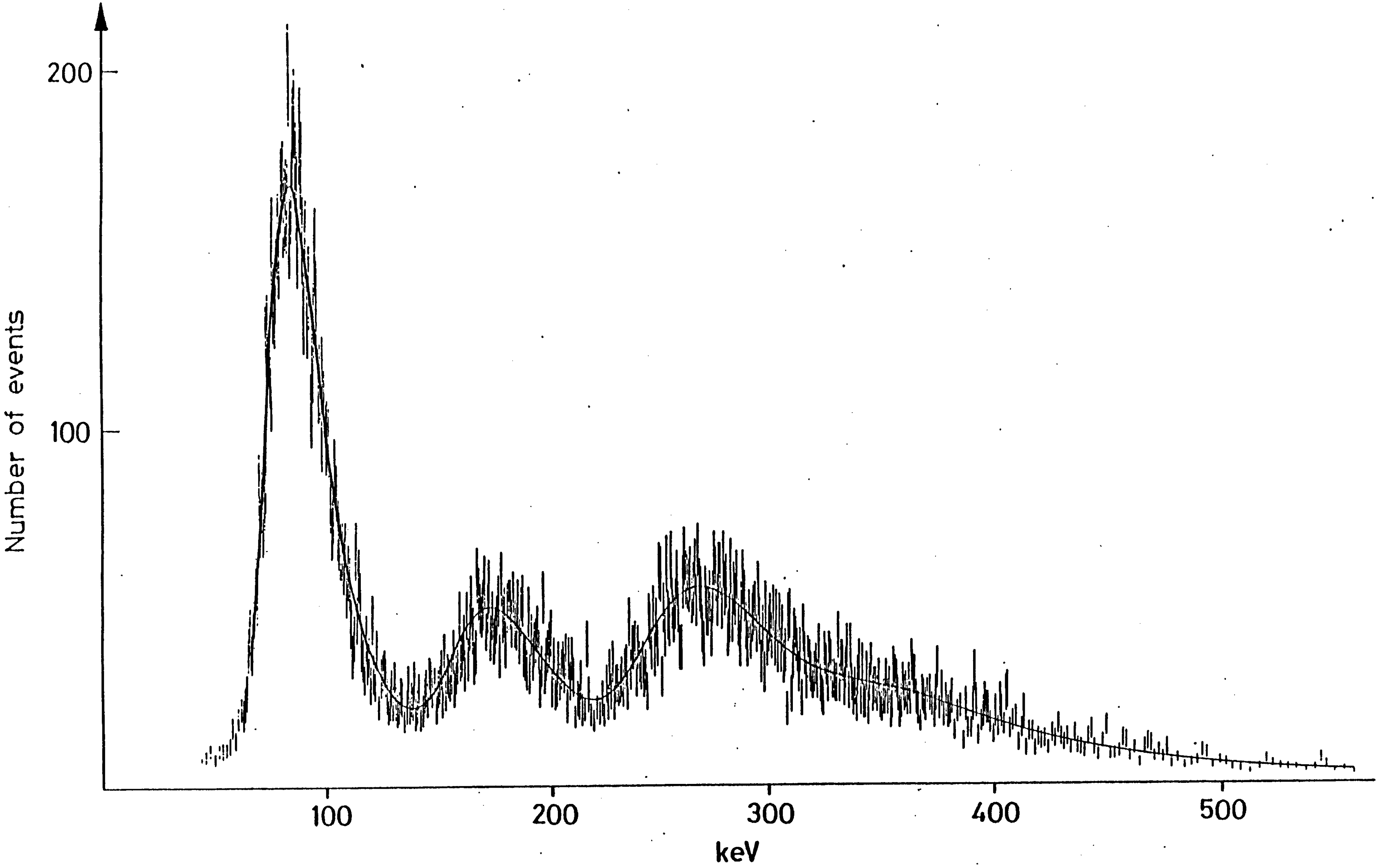

Figure 4.14

contamination of the data from non-relativistic particles may be responsible for this.

In conclusion, the energy-loss spectrum for n relativistic particles seems to be well-described by the improved energy-loss distribution $f_{IEL,n}$ of equation A.16. The parameters of this n-particle distribution may be computed by scaling up the single particle ones to those for an absorber of n times the thickness.

Chapter 5

REFINEMENT OF AN IEL FITTING ROUTINE

5.1 Single Particle Fits

The large amount and high resolution of the experimental energy-loss data (see e.g. figure 4.10) provide a very sensitive test of the theoretical model used to describe these data, but also necessitate considerable care in the fitting procedure to prevent any introduction of a numerical or statistical bias.

The null hypothesis upon which the fitting routine was based (and which was tested by the goodness of fit) was that the experimental single particle energy-loss distribution observed for a thin silicon detector derives from the convolution of a Landau probability density function with a Gaussian one. Consequently, the universal Landau function (equation A.4) had to be evaluated very often during fitting and a special subroutine [64] was prepared which calculated this function by four-point interpolation in a table of two hundred very accurate values. The table entries were calculated by Benno Schorr using Fourier series and were checked against published values [65][66] and against values obtained by contour integration.

The validity of the various approximations involved in the fitting procedure was tested using Monte Carlo data which had been generated, with known parameters, on the basis of the null hypothesis. The production of the Monte Carlo data required the development of a reliable generator of Landau-distributed random numbers [67]. Such a generator was realized by transforming uniformly-distributed random numbers according to the percentiles of the cumulative Landau distribution, the percentiles having been determined by numerical integration of our tabulated Landau function.

Fitting was achieved by the usual technique of least squares. The function minimized was

$$\chi^2(\underline{\alpha}) = \sum_i [m_i - t_i(\underline{\alpha})]^2/v_i \qquad (5.1)$$

where $\underline{\alpha}$ are the free parameters of the fit, namely σ, ξ and Δ_{mp} of the improved energy-loss (IEL) distribution (see the appendix) and a normalization factor, and where m_i and $t_i(\underline{\alpha})$ are the observed and expected contents, respectively, of the ith bin of the fitted histogram. The summation was performed over all bins of the experimental distribution (histogram). The χ^2 contribution from each bin was inversely weighted according to the statistical uncertainty of the bin contents. It is customary to take the weight, v_i, for the ith bin to be the measured number of counts, m_i, in that bin, since this is indeed the variance of a Poisson distribution of expectation value m_i.

For the test statistic given by equation 5.1 to follow a true χ^2 distribution under the null hypothesis, the contents of each bin of the histogram had to be large enough for the distribution of the number of events in that bin to be assumed Gaussian. The usual rule of thumb is that Poisson statistics become approximately Gaussian once the number of events exceeds ten. Consequently, due to the poor statistics obtained in the tail regions of an experimental distribution, it was necessary to combine some of the bins (ADC channels) of the raw data. Bins having less than the required minimum contents were joined with neighbouring ones until each new bin contained at least the minimum number of counts. The minimum bin content could be varied to ensure that it was large enough not to influence the fit and, based on the evidence of the fits to Monte Carlo data, the value finally adopted was twenty.

Strictly, $t_i(\underline{\alpha})$ is the integral, over the ith bin, of the IEL function (equation A.13) convolved with the Gaussian one due to noise and properly normalized. However, it is customary to approximate this by the value of the integrand at the centre of the bin multiplied by the bin width. This single-point computation was considered a valid approximation because more accurate integration did not significantly improve the fits to Monte Carlo data.

The convolution integral of the complete theoretical function to which the experimental data were fitted was evaluated numerically at the centre of each bin using a fixed number of evenly-spaced points covering the range ±3.5 standard deviations of the total Gaussian contribution. Fifty discrete points were used to fold the Landau and total Gaussian components together, since this number was found to be large enough not to influence the fit.

Under the null hypothesis, the expected contents of the ith bin is $t_i(\underline{\alpha})$ and, therefore, the corresponding Poisson variance is $v_i = t_i(\underline{\alpha})$. It is common practice, however, to take $v_i = m_i$, since the denominator of equation 5.1 is then independent of the fit parameters. The tacit assumption that the statistics were everywhere good enough for this approximation, viz. $m_i \approx t_i(\underline{\alpha})$, to be valid was found to be unjustified by the simple if crude expedient of averaging the error bar associated with each bin of the histogram with those on the adjacent bins. Since the bins were so narrow, this merely smoothed out statistical fluctuations which had adversely weighted the χ^2 of the fits to Monte Carlo data and a surprising improvement was observed. Having established that it was necessary, the correct variance was used despite the risk, due to the non-linearity thereby introduced, of an increase in the convergence time of the fitting routine.

5.2 Multi-particle Fits

For the multi-particle energy-loss spectra, the null hypothesis of the fitting procedure had to be modified. The theoretical function to which the multi-particle data were fitted included a contribution from each of the

n_{max} multiplicities present in the experimental distribution. This was the function used to compute $t_i(\underline{\alpha})$ of equation 5.1 and it may be written

$$T(\Delta) = \sum_{n=1}^{n_{max}} F(n) T(\Delta, n) \qquad (5.2)$$

where $T(\Delta,n)$ is the function $f_{IEL,n}(x,\Delta)$ (equation A.16) convolved with the Gaussian one due to noise and $F(n)$ is the fraction of events in which n relativistic particles traversed the detector. Putting $n_{max} = 1$ in equation 5.2 yields the function theoretically describing the experimental data for single particles.

The free parameters of the fit were $F(n)$, σ and ξ. Δ_{mp} was fixed at the canonical value for a relativistic particle traversing $x = 300$ µm of silicon, viz. 84.0 keV, and n_{max} was usually five.

The entire fitting procedure was tested using Monte Carlo data which had been generated on the basis of the modified null hypothesis. The approximations involved in fitting the single particle energy-loss spectra were found to be equally valid for the new routine.

Chapter 6

THE NA14 ACTIVE TARGET

6.1 Mechanical Details

The active target comprises thirty-one silicon detector planes, each with a useful area of 40×50.3 mm^2. These dimensions are a reflection of the constraints imposed by the technology used to refine commercially available high-resistivity silicon, which is based upon 3" diameter ingots, and by the size of the photon beam (see table 1.1). 90% of the beam falls upon the target. The detectors are 300 μm thick and are separated by 200 μm, so that the active target is 15.3 mm long and constitutes 10% of a radiation length and 3.5% of an interaction length. Each device is manufactured from a 6 kΩcm n-type silicon wafer on which p-type strips are created by ion implantation. The pitch of the strips is 2.1 mm and each has an active area 2.0 mm wide. The first thirty devices each have twenty-four vertical strips 40 mm long, while the thirty-first detector has twenty-one horizontal strips 50.3 mm in length and may be seen in figure 6.1. Figure 6.2 shows the active target as seen by a beam photon.

The need to segment each detector into strips arises from noise and counting rate considerations. The pitch is chosen such that none of the strips ever has to withstand a rate exceeding 1 MHz. Even so, the signal processing electronics must be DC coupled, the typical gate time being 70 ns. The electronic noise is dominated by the contribution from the first stage of the head amplifier. This noise grows linearly with the detector capacitance and is inversely proportional to the square root of the pulse duration. High rates necessitate a short processing time and the close proximity of the detector planes of the fine-grained target would increase unacceptably the capacitance of these detectors were they not segmented into smaller elements.

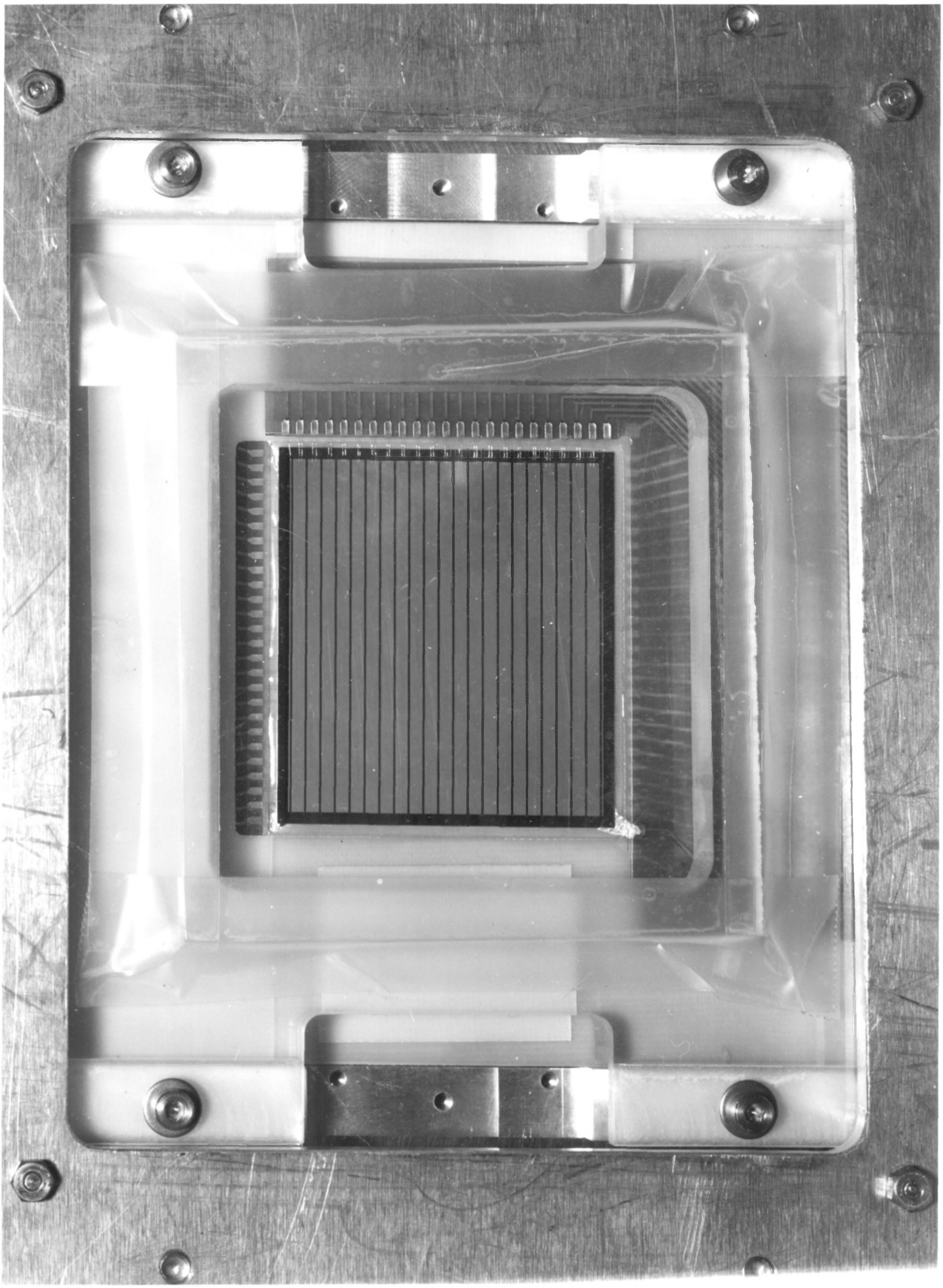

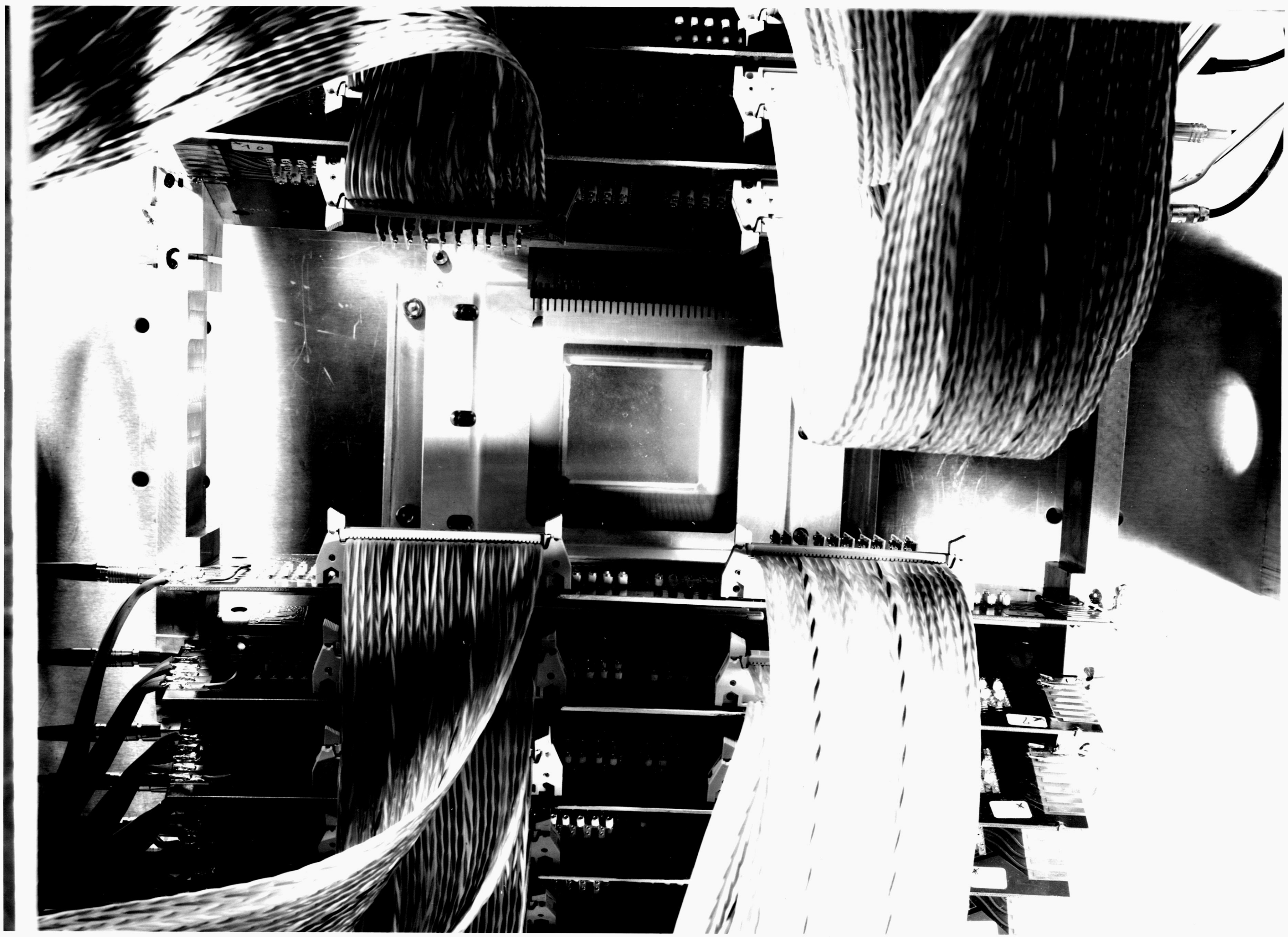

Figure 6.2

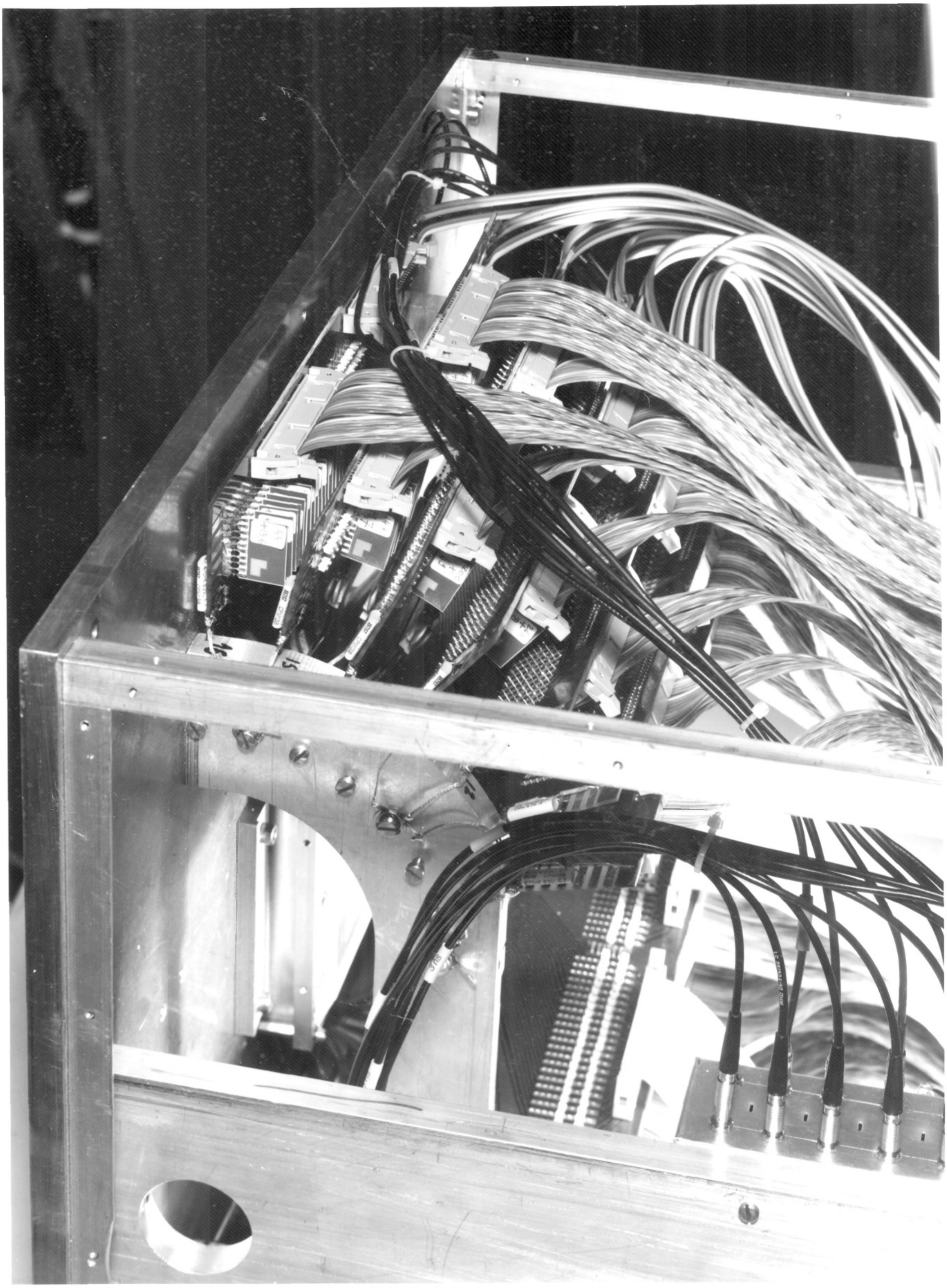

Figure 6.3

Each detector chip is glued onto a carefully-machined 500 μm thick epoxy board on which a fan-out circuit for the strips is printed. The two sides of this printed circuit board that are parallel to the strips are precision machined (to ±10 μm), allowing the boards to be positioned accurately between rigidly fixed metal guides. At one edge of each board a flexible kapton printed circuit with a standard connector affords the connection with the hybrid current-sensitive preamplifiers. The preamplifiers have been developed by the Jean Poinsignon group at Saclay and are capable of driving 90 m of twisted pair line. They are mounted on plug-in cards, some of which are clearly visible in figure 6.3.

The allowed tolerance on the detector thickness is 300 ± 15 μm from device to device, but the thickness of a given detector does not vary by more than ±5 μm. The detector planes are accurately parallel, their separation being constant at ±30 μm. Each detector has its centre positioned to ±200 μm with respect to an external reference, while the inclination of the strips is precise to ±10 mrad.

6.2 Very Preliminary Results

The silicon active target was exposed to a high-intensity photon beam during a 25 hour test run on 12 September 1982. It was installed in the AEG magnet of the NA14 spectrometer and replaced the existing experimental target, which had comprised a ^{6}Li isoscalar production target in association with a scintillator hodoscope (active "target") array. An 80 cm long tungsten beam dump was also installed for the duration of the test period. It was located immediately downstream of the active target and its purpose was to enrich the sample of prompt muons originating from charmed decays within the target over that of muons from the decay of pions and kaons. The trigger therefore demanded at least one muon in the downstream muon filter and, in addition, more than one relativistic particle had to be registered by the last detector plane of the active target. 200K events were recorded.

Regrettably, a supply failure to part of the tagging logic went unnoticed throughout data-taking and the mean energy of the resultant photon spectrum was disastrously reduced. Consequently, the data obtained are completely saturated by halo muons which traversed the apparatus in coincidence with an apparently random pretrigger. The Bethe-Heitler process $\gamma \rightarrow \mu^+\mu^-$ can be expected to dominate those events in which a pair of oppositely-charged muons are found after the beam dump. Hence figure 6.4, the summed momentum distribution of dimuons reconstructed in the spectrometer, indicates that the mean photon energy may have been lower than 40 GeV.

Valuable information was obtained, however, about the performance of the hardware associated with the active target. A complete electronic chain, comprising DC preamplifier, line receiver and LeCroy 2282B current-integrating ADC, was not available for every channel, but more than 80% of the total 741 strips were fully equipped.

The reconstruction of an event inside the active target requires a knowledge of the IEL parameters of the single particle energy-loss spectrum produced by each operational strip. These experimental distributions were obtained during calibration runs, when the target was flooded with energetic electrons and, essentially, a single strip of an upstream detector provided the trigger. Each of the "road" of strips downstream of the trigger strip should thus have also yielded a single particle signal, although energy-loss spectra could not be built up in this fashion to enable calibration fits to be made for the crossed strips of the thirty-first detector plane. The fitted IEL parameters, together with the mean and standard deviation of the pedestal noise distribution as determined from data obtained in the absence of any charged particles, constitute the calibration constants for each channel.

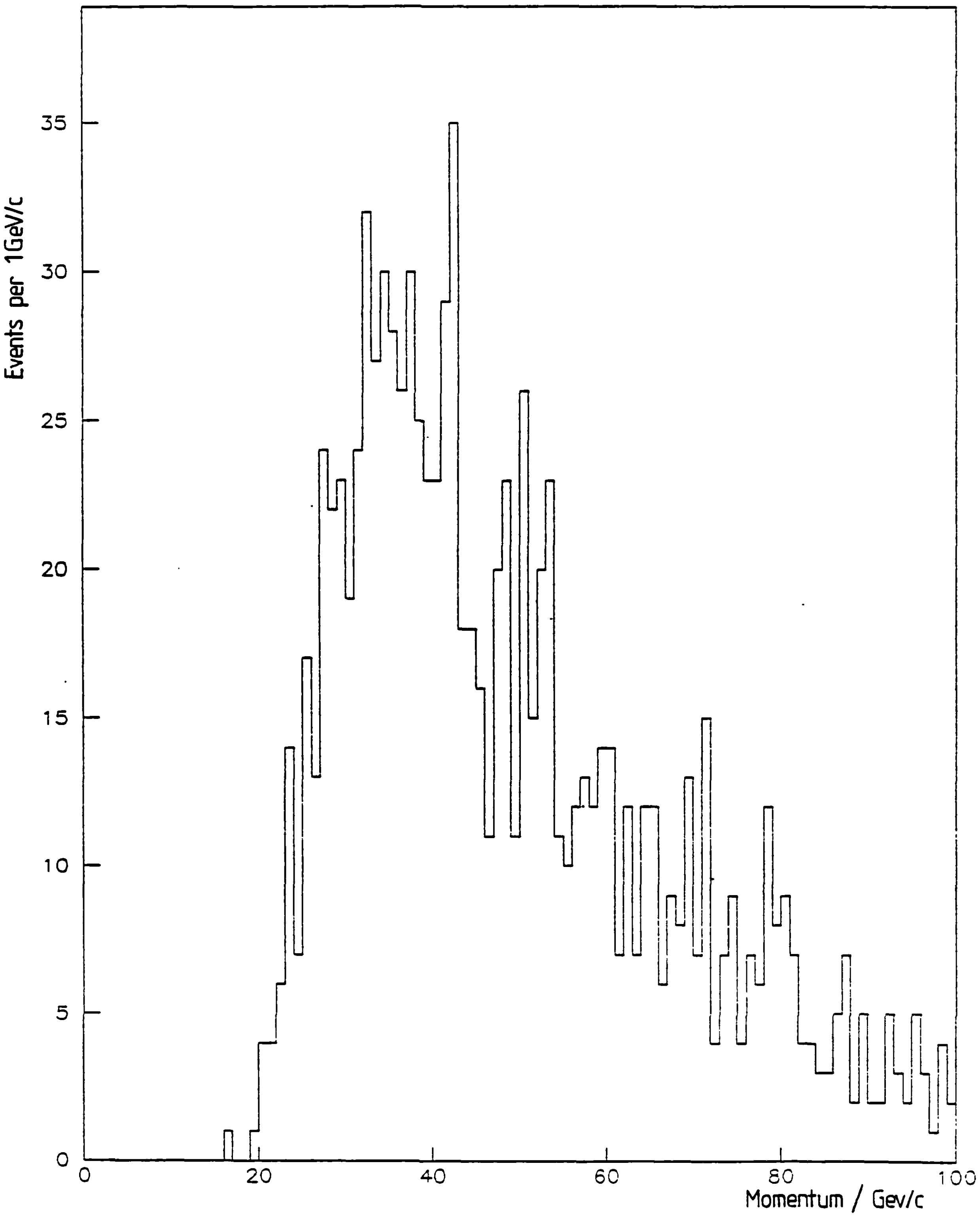
Events per 1GeV/c
35
30
25
20
15
10
5
0
0
20
40
60
80
100
Momentum / Gev/c

Figure 6.4

It was found that the shape of the calibration distributions obtained was not consistent with the familiar one of the earlier developmental work. Specifically, no values of σ or ξ could be obtained for the majority of channels despite attempts to fit only specific portions of the distributions [68]. It has been suggested that a mistimed trigger may have been responsible for the distortion of the spectra observed. In addition, it was discovered that three detector planes were not properly biased or had the bias disconnected.

The calibration constants should enable any pulse height observed for a given strip to be interpreted in terms of the most-probable number of relativistic particles crossing that strip. The missing parameters have meant that any estimate of the number of particles has had to be made on the basis of Landau theory alone and that no probability could be attached to the statement that an observed pulse height corresponds to a given multiplicity. However, setting ξ = 5.35 keV, Landau theory is sufficient to determine the number of relativistic particles to 15% or so up to a multiplicity of about four. This is the significance of the numbers displayed in the reconstructed low-multiplicity event of figure 6.5. The event itself is merely a photon conversion accompanied by two background single particle tracks, but it serves to illustrate the presence of noise spikes in some channels and how "Landau fluctuations" may belie the number of particles crossing a strip. This last point is a particularly important feature of the data because it means that the charged particle multiplicity cannot be ascertained reliably from the information from an individual strip. Early and necessarily crude Monte Carlo work indicates that, provided the multiplicity remains unchanged for at least four successive target layers, a multiplicity step of two may be located to the nearest detector plane. Clearly, this imposes an ultimate lower limit on the lifetime which may be investigated. The Monte Carlo program was written as a precursor to the maximum likelihood routine which it is

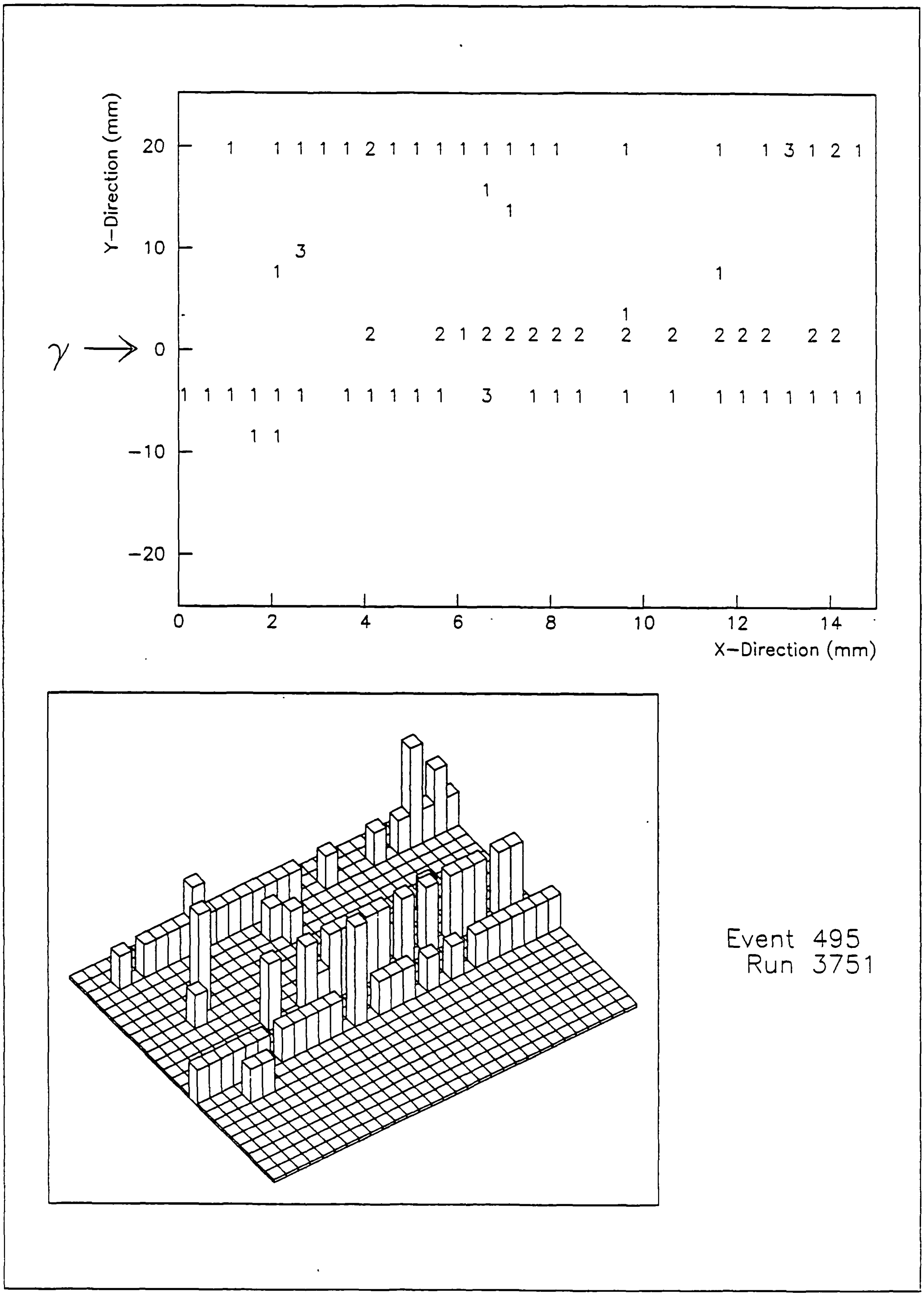
Y–Direction (mm)
20
10
0
−10
−20
0
2
4
6
8
10
12
14
X–Direction (mm)
γ →
Event 495
Run 3751

Figure 6.5

hoped will eventually be able to use all of the calibration data and take account of dead channels to provide the most-probable estimate of the position of decay vertices in candidate decay events.

The stability of the electronics was inferred from an examination of certain calibration constants as a function of time. The DC offset level, as reflected by the pedestal position, was stable to better than ±1% and the variation of σ_{noise} was never more than ±12% throughout the data-taking period. The parameter Δ_{mp} provided a handle on the overall gain, in which no significant variation was found. The FWHM of the noise was, on average, about 40 keV, although this figure is adversely weighted by some particularly noisy channels.

Since this brief beam dump test, no other data have been recorded using the active target.

6.3 Prognosis. The Microstrip Detectors

Work has been undertaken to produce six microstrip detector planes (three y-z doublets) and to equip them with a full complement of electronics by March 1984. Each device will be 350 μm thick and will have 1000 strips at 50 μm pitch over an active area of 50×50 mm^2. The strips, created on n-type silicon by ion implantation, will all be read out. The size of the printed circuit board (see figure 6.6) needed to fan out 1000 strips to a standard 0.05" connector is 39×39 cm^2, which will fit inside the AEG magnet yoke.

The final geometry of the NA14 vertex detector is to be decided on the basis of a Monte Carlo simulation, but it is currently anticipated that the distance between each y-z detector pair will be some 5 mm while that between the centres of successive doublets will be approximately 30 mm. For purely mechanical reasons the first microstrip detector plane cannot be mounted less than 20 mm from the end of the active target. The addition of a fourth (u-v)

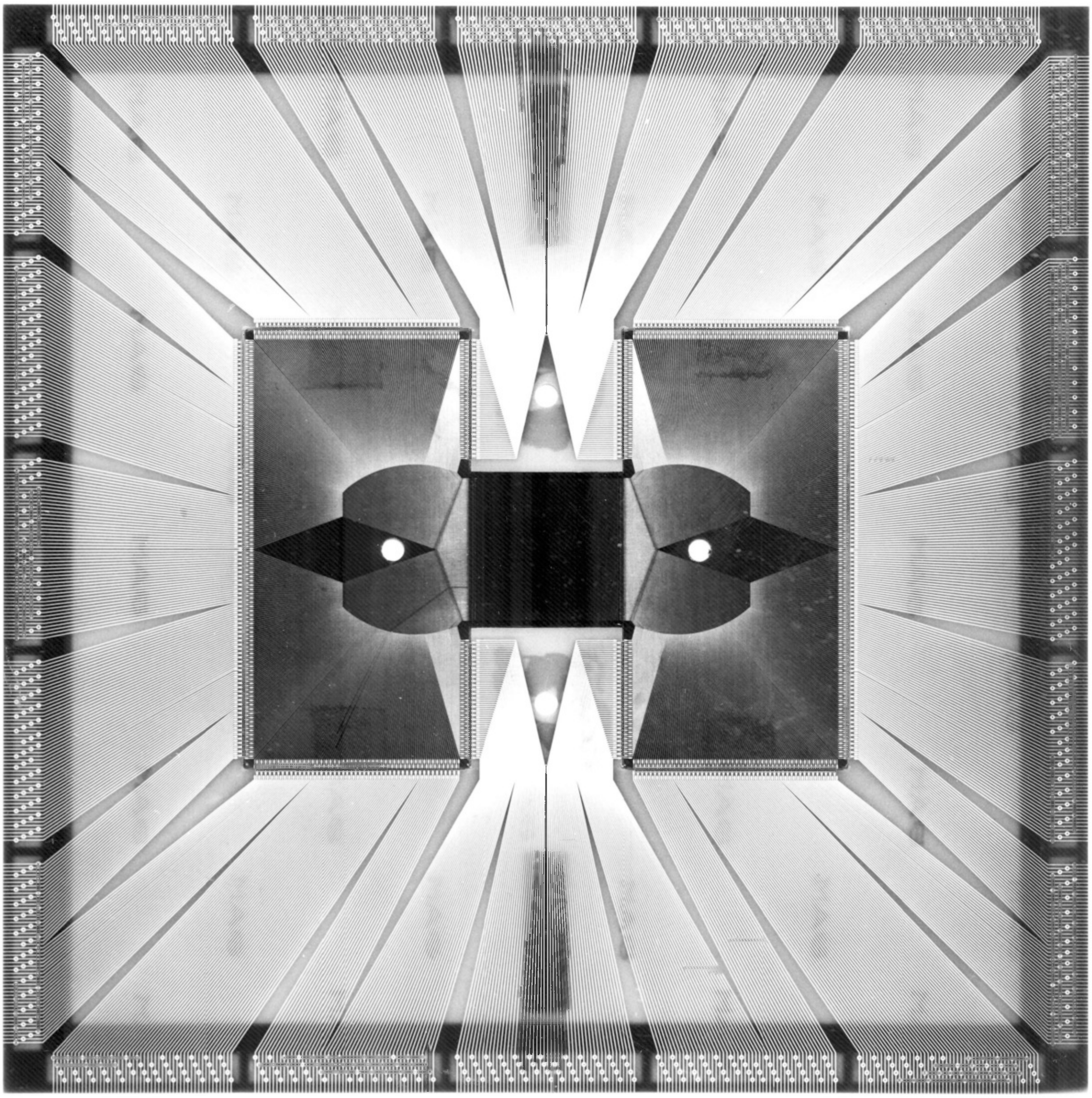

Figure 6.6

doublet is envisaged by June 1984. These detectors will have strips inclined at roughly ±30° to the vertical and will be positioned approximately 20 mm downstream of the last y-z doublet. The Monte Carlo simulation will optimize the conflicting requirements of coverage of large solid angle and good resolution of displaced secondary vertices within the active target from the extrapolation of tracks reconstructed in the microstrip detectors.

With the microstrip detectors it is intended to record only the fact that a strip has given a signal above a preset threshold (fixed at 40% of the most-probable single particle signal), i.e. that a "hit" has been registered. Consequently, as the maximum counting rate is much lower than for the active target (by a factor of at least twenty), AC coupling is perfectly suitable for this purpose.

Tests of prototype microstrip detectors have been conducted in a 3.5 GeV/c pion beam. These indicate a degree of charge sharing such that, in about 25% of events at normal incidence, a hit is also registered by one strip neighbouring that from which a signal in excess of 25% over threshold is observed. A similar definition of triple hits revealed a 3% effect. The noise performance of the electronics was particularly good, the threshold level typically being more than three standard deviations above the noise.

A tentative schedule sees the active target and six microstrip detector planes tested together for the first time (using high-energy muons) around April and May 1984. It is hoped to take the first photon data with the complete vertex detector in August of the same year.

APPENDIX

The statistical nature of the ionization energy-loss process upon the passage of a fast charged particle through a medium leads to large fluctuations in the energy loss of such a particle in an absorber which is thin compared with the total range of the particle in that medium.

This straggling of the energy loss was first studied by Landau [59], who introduced a probability density function, $f(x,\Delta)$, giving the distribution of energy losses for particles traversing an absorber of thickness x. The energy loss, Δ, results from many single losses occurring in collisions with individual atomic electrons. The collision cross-section, differential in the energy loss, may be specified by a distribution, $w(E)$, obtained from $f(x,\Delta)$ at small x:

$$w(E) = \lim_{x \to 0} \frac{f(x,E)}{x}$$

That is, $w(E)dE$ is the probability per unit path length of a single collision transferring energy in the range E to $E+dE$ to an electron in the absorbing medium. It is assumed that the total energy loss, Δ, in a path length x is small in comparison with the initial energy of the particle, so that any dependence of $w(E)$ on particle energy may be neglected. The absorber is required to be "thin" in this specific sense.

Landau derived an expression for the energy-loss distribution function by solving the transport equation

$$\frac{\partial}{\partial x} f_L(x,\Delta) = \int_0^\infty w_L(E)[f_L(x,\Delta-E) - f_L(x,\Delta)]dE \qquad (A.1)$$

Applying a Laplace transformation with respect to the independent variable Δ, he obtained

$$f_L(x,\Delta) = \frac{1}{2\pi i} \int_{-i\infty+\varepsilon}^{i\infty+\varepsilon} \exp(I_L)dp$$

where p is the Laplace transform variable, ε is an arbitrary real positive constant, and where

$$I_L = p\Delta - x\int_0^\infty w_L(E)[1-\exp(-pE)]dE$$

The general form of w(E) is not known. Landau used the classical free electron (Rutherford) differential collision probability

$$xw_L(E) = \xi / E^2$$

where

$$\xi = \frac{2\pi z^2 e^4}{m_e \beta^2 c^2} \frac{N_A Z}{A} \rho x \qquad \text{(A.2)}$$

$$= (0.1781 \text{ MeV cm}^{-1}) \frac{z^2}{\beta^2} x, \quad \text{for silicon.}$$

Here, m_e is the electron mass, N_A is Avogadro's number, βc and ze are respectively the velocity and charge of the incident particle, and Z, A and ρ are respectively the atomic number, atomic mass and density of the absorbing medium.

The Landau solution may be written

$$f_L(x,\Delta) = \frac{1}{\xi} \phi(\lambda) \qquad \text{(A.3)}$$

where

$$\phi(\lambda) = \frac{1}{2\pi i}\int_{-i\infty+\varepsilon}^{i\infty+\varepsilon} \exp(u\ln u + \lambda u)du \qquad \text{(A.4)}$$

is the "universal Landau function" of the single dimensionless variable

$$\lambda = \frac{1}{\xi}\left[\Delta-(\Delta_{mp}-\xi\lambda_o)\right] \qquad \text{(A.5)}$$

Here, Δ_{mp} is the most-probable energy loss of the Landau distribution and corresponds to $\lambda=\lambda_o$. That is, λ_o is the value of λ for which $\phi(\lambda)$ is a maximum.

Subsequently, Vavilov [60] derived a more accurate solution by taking into account the kinematic constraints on the energy transfer, E. The limits of integration in equation A.1 allow infinite energy transfer, but, for an incident particle of mass m, the maximum energy transferable in a single collision is

$$E_{max} = 2m_e\gamma^2\beta^2c^2[1 + 2\gamma(m_e/m) + (m_e/m)^2]^{-1} \qquad \text{(A.6)}$$

where $\gamma = (1-\beta^2)^{-1/2}$.

Imposing this limit, he rewrote the transport equation as

$$\frac{\partial}{\partial x} f_V(x,\Delta) = \int_0^b w_V(E)f_V(x,\Delta-E)dE - f_V(x,\Delta)\int_0^{E_{max}} w_V(E)dE$$

where

$$b = \begin{cases} \Delta & , \text{ for } \Delta < E_{max} \\ E_{max} & , \text{ for } \Delta > E_{max} \end{cases}$$

and where the differential collision probability,

$$x\, w_V(E) = \xi[1-\beta^2(\frac{E}{E_{max}})]/E^2,$$

still treats the target electron as free and, strictly, is that for spin zero incident particles. However, provided that E is small compared with the kinetic energy of the incoming particle and with m^2c^2/m_e, $w_V(E)$ adequately describes the collision probabilities for incident particles of spin a half and spin one [69]. Using a Laplace transform method, Vavilov obtained the solution

$$f_V(x,\Delta) = \frac{1}{2\pi i} \int_{-i\infty+\varepsilon}^{i\infty+\varepsilon} \exp(I_V)dp \qquad (A.7)$$

where

$$I_V = p(\Delta-\langle\Delta\rangle) - x \int_0^{E_{max}} w_V(E)[1-\exp(-pE)-pE]dE \qquad (A.8)$$

and where the mean energy loss is known from the familiar Bethe-Bloch formula

$$\langle\Delta\rangle = \xi[\ln(2m_e\gamma^2\beta^2c^2E_{max}/I_{eff}^2)-2\beta^2-\delta-U]$$

Here, δ and U are the density effect and shell correction terms, respectively, and I_{eff} is the mean ionization potential of the atomic electrons in the absorbing medium. The δ term corrects for the shielding due to the polarization of the atoms of the absorber in response to the electric field of the incident particle and has been calculated for many media by Sternheimer [70][71]. U takes account of the non-participation of the electrons in the inner shells when the velocity of the incident particle is low and it is negligible for $\beta > 0.3$ [72][73].

The Vavilov solution may be written

$$f_V(x,\Delta) = \frac{1}{\pi\xi}\,\kappa \exp\left[\kappa(1+\beta^2 C)\right] \int_0^\infty \exp(\kappa f_1)\cos(u\lambda_1 + \kappa f_2)\,du$$

where

$$f_1 = \beta^2[\ln u - \mathrm{Ci}(u)] - \cos u - u\,\mathrm{Si}(u)$$

$$f_2 = u\,[\ln u - \mathrm{Ci}(u)] + \sin u + \beta^2 \mathrm{Si}(u)$$

$$\lambda_1 = \kappa\left[\frac{1}{\xi}(\Delta - \langle\Delta\rangle) - 1 - \beta^2 + C\right] \tag{A.9}$$

and

$$\kappa = \xi / E_{max} \tag{A.10}$$

Here, Si and Ci denote the sine integral and cosine integral functions, respectively, and C is Euler's constant.

Vavilov also demonstrated that his solution coincides with the Landau distribution in the limit as $\kappa \to 0$. Indeed, the Landau parameter is readily expressed in terms of those of the Vavilov distribution:

$$\lambda = \frac{\lambda_1}{\kappa} - \ln\kappa$$

Hence, by considering the limiting case when Δ is the same according to both Landau and Vavilov theory, we may substitute from equations A.5 and A.9 to obtain an expression for the most-probable energy loss of the Landau distribution:

$$\Delta_{mp} = \langle\Delta\rangle + \xi(1+\beta^2 - C + \lambda_o + \ln\kappa) \tag{A.11}$$

Further corrections to the theory, in order to take account of the fact that the electrons in the absorbing medium are not free, have been attempted by Blunck and Leisegang [74], Bichsel [75][76], and by Shulek et al. [63].

Atomic shell structures, when considered, modify the simple description of interactions on free electrons by introducing collective motion and fine level structure.

The method for improving the calculaton is to continue the expansion of the exponent of the integrand (equation A.8) to next order in p and, in equation A.7, to replace it by $I = I_V + \delta I_V$, where

$$\delta I_V = -x \int_0^{E_{max}} [w(E)-w_V(E)][1-\exp(-pE)-pE]dE \qquad (A.12)$$

Clearly, this method requires some kind of knowledge of the true cross-section, w(E). Now, although the upper integration limit in equation A.12 is E_{max}, only low values of E - corresponding to distant collisions - provide any contribution to δI_V. For higher values of energy transfer, $w(E) \rightarrow w_V(E)$ and hence

$$\delta I_V \approx -\frac{1}{2} p^2 x \int_0^{E_{max}} [w(E) - w_V(E)]E^2 dE = -\frac{1}{2} p^2 x \delta_2$$

where δ_2 is thus defined as the difference between the second moments of w(E) and $w_V(E)$.

This method is particularly convenient when the Vavilov and Landau solutions may be taken to coincide. Using the convolution properties of Laplace transforms, it may then be shown [77] that the introduction of the correction term δI_V results is an improved energy-loss (IEL) function which is based on the Landau distribution:

$$f_{IEL}(x,\Delta) = (2\pi\delta_2)^{-1/2} \int_{-\infty}^{\infty} f_L(x,\Delta-u)\exp(-u^2/2\delta_2)du \qquad (A.13)$$

Thus, the experimentally observed energy-loss distribution may be calculated quite straightforwardly as the convolution of the Landau distribution with a Gaussian one of standard deviation $\sigma = \sqrt{\delta_2}$. This supposes that no additional effects lead to any further broadening. Bichsel has shown that the contribution to δI_V from higher moments is negligible [75] and has obtained the following expression for δ_2 [76]:

$$\delta_{2,B} = 2\xi[C_1 + C_2(2\ln(\beta\gamma) - \beta^2)] \qquad (A.14)$$

where $C_1 \to 6$ keV and $C_2 \to 0.29$ keV as $\beta \to 1$.

Shulek et al [63] propose the form

$$\delta_{2,S} = \frac{8}{3}\xi \sum_i \frac{Z_i}{Z} I_i \ln(2m_e\beta^2c^2/I_i) \qquad (A.15)$$

where Z_i is the number of electrons in the ith shell and I_i is its ionization potential. The summation is performed over the atomic shells of the absorber for which $I_i < 2m_e\beta^2c^2$. These ionization potentials have been computed by Sternheimer [70][71] and enter the calculation of the density effect correction to the mean energy loss.

The result of the convolution with the Gaussian component is a broader distribution whose peak position, E_{mp}, is slightly greater than the most-probable energy loss of pure Landau theory.

The energy-loss distribution arising from n relativistic particles simultaneously crossing an absorber of thickness x may be taken as

$$f_{IEL,n}(x,\Delta) = f_{IEL}(nx,\Delta) \qquad (A.16)$$

Hence it will be seen that this distribution is the convolution of a Gaussian of variance $\sigma_n^2 = n\sigma^2$ with a Landau distribution whose parameters are $\xi_n = n\xi$ and $\Delta_{mp,n} = n(\Delta_{mp} + \xi \ln(n))$, where $\sigma = \sqrt{\delta_2}$, ξ and Δ_{mp} are the parameters of the single relativistic particle energy-loss distribution for that absorber.

REFERENCES

[1] "Now this, O monks, is noble truth that leads to the cessation of pain: this is the noble Eightfold Way: namely, right views, right intention, right speech, right action, right living, right effort, right mindfulness, right concentration."

[2] Gell-Mann, M., Phys. Rev. 125, 1067 (1962).

[3] Barnes, V., et al., Phys. Rev. Lett. 12, 204 (1964).

[4] Gell-Mann, M., Phys. Lett. 8, 214 (1964).

[5] Zweig, G., CERN 8182/TH 401 (1964).

[6] "Three quarks for Muster Mark."

[7] Panofsky, W., in Proc. International Symposium on High Energy Physics, Vienna, 1968.

[8] Glashow, S.L., Iliopoulos, J. and Maiani, L., Phys. Rev. D2, 1285 (1970).

[9] Aubert, J.J., et al., Phys. Rev. Lett. 33, 1404 (1974).

[10] Augustin, J.E., et al., Phys. Rev. Lett. 33, 1406 (1974).

[11] Goldhaber, G., et al., Phys. Rev. Lett. 37, 255 (1976).

[12] Peruzzi, I., et al., Phys. Rev. Lett. 37, 569 (1976).

[13] Perl, M., et al., Phys. Rev. Lett. 70B, 487 (1977).

[14] Herb, S.W., et al., Phys. Rev. Lett. 39, 252 (1977).

[15] Witten, E., Nucl. Phys. B120, 189 (1977).

[16] Llewellyn-Smith, C.H., Phys. Lett. 79B, 83 (1978).

[17] Sivers, D., Townsend, J. and West, G., Phys. Rev. D13, 1234 (1976).

[18] Halzen, F. and Scott, D.M., Phys. Lett. 72B, 404 (1978).

[19] Drell, S.D. and Yan, T.M., Phys. Rev. Lett. 25, 316 (1970).

[20] Fritzsch, H. and Streng, K.H., Phys. Lett. 72B, 385 (1978).

[21] Babcock, J., Sivers, D. and Wolfram, S., Phys. Rev. D18, 162 (1978).

[22] Brianti, G. and Doble, N., CERN/SPS/EA 77-2 (1977).

[23] Lander, R.L., et al., Nucl. Instr. and Meth. 42, 261 (1966).

[24] Lander, R.L., et al., Nucl. Instr. and Meth. 67, 173 (1969).

[25] Bellini, G., et al., Nucl. Instr. and Meth. 107, 85 (1973).

[26] Bellini, G., in Proc. Topical Meeting on Multiparticle Production on Nuclei at Very High Energies, Trieste, 1977.

[27] CERN/SPSC/80-85, SPSC/M247 (1980).

[28] Albini, E., et al., Phys. Lett. 110B, 339 (1982).

[29] CERN/SPSC/81-91, SPSC/P170 (1981).

[30] CERN/SPSC/82-33, SPSC/P170/Add.1 (1982).

[31] Kemmer, J., et al., in Proc. Workshop on Silicon Detectors for High Energy Physics, Fermilab, 1981.

[32] CERN/SPSC/82-57, SPSC/P180 (1982).

[33] Kalbfleisch, G.R., in Proc. Workshop on Silicon Detectors for High Energy Physics, Fermilab, 1981.

[34] Ushida, N., et al., Phys. Rev. Lett. 45, 1049 and 1053 (1980).

[35] McKay, K.G., Phys. Rev. 76, 1537 (1949).

[36] Bertolini, G. and Coche, A., eds., Semiconductor Detectors, Amsterdam: Elsevier North Holland (1968).

[37] Fano, U., Phys. Rev. 72, 26 (1947).

[38] Zulliger, H.R. and Aitken, D.W., IEEE Trans. Nucl. Sci. NS-17(3), 187 (1970).

[39] Shockley, W., Solid State Electronics 2, 35 (1961).

[40] Skyrme, D.J., Nucl. Instr. and Meth. 57, 61 (1967).

[41] Hansen, N.J., Scott, R.G. and Henderson, D.J., Nucl. Instr. and Meth. 104, 333 (1972).

[42] Kemmer, J., Nucl. Instr. and Meth. 169, 499 (1980).

[43] Hofker, W.H., et al., IEEE Trans. Nucl. Sci. NS-13(3), 208 (1966).

[44] Hyams, B., et al., Nucl. Instr. and Meth. 205, 99 (1983).

[45] Albini, E., et al., papers contributed to the Twentieth International Conference on High-energy Physics, Madison, 1980.

[46] CERN/SPSC/82-73, SPSC/P109/Add.2 (1982).

[47] Bonamy, P., et al., CERN/NA14/81-30 (1981).

[48] Charpak, G., et al., Nucl. Instr. and Meth. 167, 455 (1979).

[49] Heijne, E.H.M., et al., Nucl. Instr. and Meth. 178, 331 (1980).

[50] D'Angelo, P., et al., Nucl. Instr. and Meth. 193, 533 (1982).

[51] Rancoita, P.G., CERN/NA14/81-9 (1981).

[52] Frenkel, J., Z. Physik 35, 652 (1926).

[53] Borgeaud, P., et al., Nucl. Instr. and Meth. 211, 363 (1983).

[54] Hancock, S., et al., Phys. Rev. A28, 615 (1983).

[55] Hancock, S., et al., accepted for publication in Nucl. Instr. and Meth. (1983).

[56] Aitken, D.W., Lakin, W.L. and Zulliger, H.R., Phys. Rev. 179, 393 (1969).

[57] Bellamy, E.M., et al., Phys. Rev. 164, 417 (1967).

[58] Maccabee, H.D., Raju, M.R. and Tobias, C.A., Phys. Rev. 165, 469 (1968).

[59] Landau, L., J. Phys. (USSR) 8, 201 (1944).

[60] Vavilov, P.V., Soviet Phys. JETP 5, 749 (1957).

[61] Esbensen, H., et al., Phys. Rev. B18, 1039 (1978).

[62] Heijne, E.H.M., et al., Nucl. Instr. and Meth. 205, 437 (1983).

[63] Shulek, P., et al., Soviet J. Nucl. Phys. 4, 400 (1967).

[64] James, F. and Hancock, S., CERN Computer Centre Program Library, G112 (1982).

[65] Schorr, B., Comp. Phys. Comm. 7, 215 (1974).

[66] Borsch-Supan, W., J. Res. Nat. Bur. Stand. 65B, 245 (1961).

[67] James, F. and Hancock, S., CERN Computer Centre Program Library, G903 (1982).

[68] Burchell, M., Hancock, S. and Noon, P., CERN/NA14/83-11 (1983).

[69] Rossi, B., High Energy Particles, Englewood Cliffs, N.J.: Prentice-Hall (1952).

[70] Sternheimer, R.M. and Peierls, R.F., Phys. Rev. B3, 3681 (1971).

[71] Sternheimer, R.M., Phys. Rev. 145, 247 (1970).

[72] Walske, M.C., Phys. Rev. 88, 1283 (1952).

[73] Walske, M.C., Phys. Rev. 101, 940 (1956).

[74] Blunck, O. and Leisegang, S., Z. Physik 128, 500 (1950).

[75] Bichsel, H., Phys. Rev. B1, 2854 (1970).

[76] Bichsel, H. and Yu, S., IEEE Trans. Nucl. Sci. NS-19(6), 172 (1972).

[77] Fano, U., Ann. Rev. Nucl. Sci. 13, 1 (1963).

Nuclear Instruments and Methods in Physics Research B1 (1984) 16–22
North-Holland, Amsterdam

ENERGY-LOSS DISTRIBUTIONS FOR SINGLE PARTICLES AND SEVERAL PARTICLES IN A THIN SILICON ABSORBER

S. HANCOCK [1], F. JAMES [2], J. MOVCHET [3], P.G. RANCOITA [4]* and L. VANROSSUM [3]

[1] *Imperial College, London, UK.*
[2] *CERN Geneva, Switzerland,*
[3] *CEN Saclay, Gif-sur-Yvette, France,*
[4] *CEN Saclay, France.*

Received 17 June 1983

The energy-loss distributions for protons, with kinetic energies between 220 and 850 MeV, and for several relativistic particles produced at incoming beam momentum of 115 GeV/c, have been measured in an ion-implanted silicon detector of 300 μm thickness. The data are well described by an improved energy-loss distribution which takes into account the long-distance collisions disregarded in both the Landau and Vavilov distributions.

1. Introduction

The energy-loss spectrum of a charged particle traversing a thin silicon detector is given, to a first approximation, by the Landau [1] and Vavilov [2] theories, which are based on Rutherford scattering on free electrons.

In very thin (< 300 μm) silicon detectors, significant deviations from the Landau–Vavilov theory are expected. These deviations have already been observed [3] for single relativistic pions and protons in the momentum range 0.7 to 115 GeV/c. As consequence, the energy-loss spectrum of n relativistic particles traversing a very thin silicon device is expected to deviate from that predicted by the Landau and Vavilov theories.

The purpose of the present investigation is to measure the energy-loss spectra of protons with kinetic energy lower than 850 MeV (where a strong β dependence is expected) and the energy-loss spectra of several relativistic particles.

2. Energy-straggling

The statistical nature of the ionization process on the passage of a fast charged particle through matter results in large fluctuations of the energy-loss in absorbers which are thin compared with particle range.

The calculation of these fluctuations was performed first by Landau [1] and subsequently Vavilov [2] provided a more accurate solution by introducing the kinematical limit on the maximum transferable energy in a single collision. The Vavilov distribution approaches the Landau spectrum for:

$$k = \xi/E_{\mathrm{m}} \to 0,$$

where

$$\xi = 0.1535(z^2 Z\rho x)/(\beta^2 A)\ \mathrm{MeV}, \tag{1}$$

z and βc are the charge and the velocity of the incoming particle, Z, A and ρ (g/cm^3) are the atomic number, atomic weight and density of the material, x is the crossed thickness of the substance in cm and $E_{\mathrm{m}} = 2m_{\mathrm{e}}c^2\beta^2\gamma^2\ [1 + 2m_{\mathrm{e}}\gamma/m + (m_{\mathrm{e}}/m)^2]^{-1}$ is the maximum transferable energy in a single collision between the incoming particle of mass m and the atomic electron of mass m_{e}. The above condition is already satisfied for $k \approx 0.06$–0.08 (see [3,4]).

The improved energy-loss distribution is given by [3,5–8]:

$$f(\epsilon, x) = 1/(\sigma\sqrt{2\pi})\int_{-\infty}^{+\infty} f_{\mathrm{L,V}}(\epsilon', x) \times \exp\left[-(\epsilon-\epsilon')^2/2\sigma^2\right]\mathrm{d}\epsilon', \tag{2}$$

where ϵ is the actual energy-loss when a thickness x of material is traversed, $f_{\mathrm{L,V}}(\epsilon, x)$ are either the Landau or the Vavilov distribution.

The standard deviation σ of the convoluting Gaussian function can be computed using the expression of Shulek et al.:

$$\sigma^2 = (8/3)\xi\sum_i I_i(Z_i/Z)\ \ln\left(2m_{\mathrm{e}}c^2\beta^2/I_i\right) = (8/3)\xi F(\beta), \tag{3}$$

---

* On leave from INFN, Milano, Italy.

where $F(\beta) = 10^{-3}(2.319 + 0.670 \ln \beta)$ MeV in Si, I_i is the ionization potential of the ith shell [9], Z_i is the number of electrons in the ith shell of the stopping material and the summation is carried out over those shells for which $I_i < 2m_ec^2\beta^2$. The $F(\beta)$ value given below has been computed assuming that all the shells satisfy this limit.

For $k < 0.06$, the energy-loss distribution sensed by a Si-detector is simply given by:

$$f_{ex}(\epsilon, x) = 1/\left(\sigma_t\sqrt{2\pi}\right)\int_{-\infty}^{+\infty} f_L(\epsilon', x) \times \exp\left(-(\epsilon-\epsilon')^2/2\sigma_t^2\right)d\epsilon', \qquad (4)$$

where $\sigma_t^2 = \sigma^2 + \sigma_{noise}^2$, and σ_{noise} is the standard deviation of the Gaussian noise distribution, introduced by the detector and its coupled electronics.

The Landau distribution is given by:

$$f_L(\epsilon, x) = (1/\xi)\phi(\lambda),$$

where the function $\phi(\lambda)$ is a universal function of the dimensionless variable λ:

$$\lambda = (1/\xi)(\epsilon - \langle\epsilon\rangle) - \beta^2 - \ln(\xi/E_m) - 1 + C$$
$$= (1/\xi)\left[\epsilon - (\epsilon_{mp} - \xi\lambda_0)\right], \qquad (5)$$

where C is the Euler constant 0.577215, λ_0 is the value for which ϕ is a maximum, $\langle\epsilon\rangle$ is the mean energy-loss, ϵ_{mp} is the most probable energy loss for the Landau distribution. The function $\phi(\lambda)$ has been tabulated by Boersch-Supan [10] and more recently by Kolbig and Schorr [11]. The full-width-at-half-maximum of the Landau distribution is $\approx 4\xi$ *.

The mean energy-loss, $\langle\epsilon\rangle$, can be computed from the Bethe–Bloch formula:

$$\langle\epsilon\rangle = \xi\left[\ln\left(2m_ec^2\beta^2\gamma^2E_m/I^2\right) - 2\beta^2 - \delta - U\right], \qquad (6)$$

where I is the mean excitation potential of the atoms of the substance ($I = 172$ eV for Si), U is a term due to the non-participation of the inner shells for very low velocities of the particle, δ is the correction due to the density effect. U is negligible for $\beta > 0.3$ [6,13,14]. The density effect has been calculated by Sternheimer [9,15,16].

Assuming $\lambda_0 = -0.225$, from eqs. (5) and (6) we get:

$$\epsilon_{mp} = \xi\left(0.198 + \beta^2 + \ln(\xi/E_m) + \langle\epsilon\rangle/\xi\right)$$
$$= \xi\left(0.891 + \ln\left[m_ec^2(10^6\,\text{eV})/I^2\right] - \beta^2 + 2\ln(\beta\gamma) + \ln(\xi) - \delta\right), \qquad (7)$$

where ξ is expressed in MeV, and $\beta\gamma = P/mc$ (P is the momentum of the incoming particle).

For relativistic heavy particles with $\beta\gamma > 30$ (namely protons with momentum > 28 GeV/c and pions with momentum > 4 GeV/c) and for Si absorber, eq. (7) may simply be written as:

$$\epsilon_{mp} = \xi[20.936 + \ln(\xi)]. \qquad (8)$$

The energy-loss distribution, $\Lambda(\epsilon, n)$, of n parallel relativistic particles sensed by a Si-detector of thickness x, is given by:

$$\Lambda(\epsilon, n) = f_{ex}(\epsilon, nx) \qquad (9)$$

namely by the convolution of a Gaussian of variance $\sigma_t^2 = \sigma_{noise}^2 + \sigma_n^2$ (where $\sigma_n = \sigma\sqrt{n}$), with a Landau distribution where $\xi_n = n\xi$ and $\epsilon_{n,mp} = n\xi(20.936 + \ln(n\xi)) = n(\epsilon_{mp} + \xi\ln(n))$. The parameters σ, ξ, and ϵ_{mp} are those computed for a single relativistic particle traversing a thickness x.

3. Energy-loss measurements for slow protons

3.1. Experimental method

In the present investigation, energy-loss has been measured for protons in the kinetic energy range between 220 and 850 MeV (see table 1), at Saturne II in Saclay. The momentum spread, $\Delta P/P$, was never more than 0.1%. A well-defined momentum is important particularly at low values, since any momentum spread broadens the energy-loss distribution and thereby masks the effect due to long-distance collisions.

An Enertec ion-implanted passivated-silicon junction detector with an active area of 1.0 cm^2 and a thickness of 300 ± 5 μm was used. Total depletion of the detector was achieved at reverse bias of about 100 V. The initial leakage current was 16 nA. The signal processing from this detector and the experimental arrangement have already been described in a previous paper [3].

The detector, together with its associated electronics, had a Gaussian noise distribution with a measured standard deviation, σ_{noise}, whose typical value was 5.0 ± 0.4 keV. The exact value was determined separately before each data taking at the different energies.

A Ru β^- source has been used for calibration purposes. It had been determined that the value of ϵ_{mp} for

Table 1
Values of ξ, σ, ϵ_{mp} and E_{mp} vs the incoming proton kinetic energy.

Kinetic energy [MeV]	ξ [keV]	σ [keV]	ϵ_{mp} [keV]	E_{mp} [keV]
220	15.8±0.8	9.7±1.2	206.8±6.2	210.2±6.2
350	11.9±0.8	8.7±1.3	149.8±4.5	152.3±4.5
600	8.5±0.4	8.2±0.7	111.0±3.4	113.5±3.4
700	8.6±0.5	5.0±0.9	105.6±3.2	108.1±3.2
850	8.2±0.4	4.8±0.9	99.5±3.0	101.2±3.0

---

* From [10] we have: fwhm = 3.98 ξ. However in a successive computation it was found [12]: fwhm = 4.02 ξ and $\lambda_0 = -0.229$ and in [11] $\lambda_0 = -0.2227829812564$.

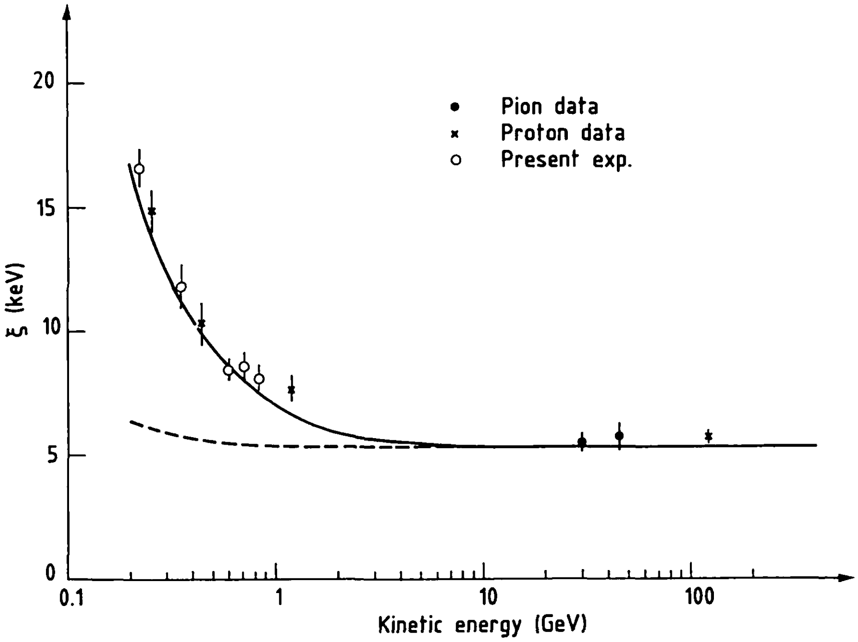

Fig. 1. Determined values of the parameter ξ. The continuous and broken curves are computed from eq. (1) for protons and pions, respectively. The general agreement between the fitted value and the predicted one indicates that the energy calibration had been correctly performed.

relativistic electrons is 86.8 ± 2.8 keV on the same scale that yields the canonical value of 84.0 ± 2.8 keV for relativistic pions, once only electrons with kinetic energy greater than 1 MeV are selected [3].

3.2. Data analysis

The experimental energy-loss distributions for each kinetic energy were fitted to the Landau probability

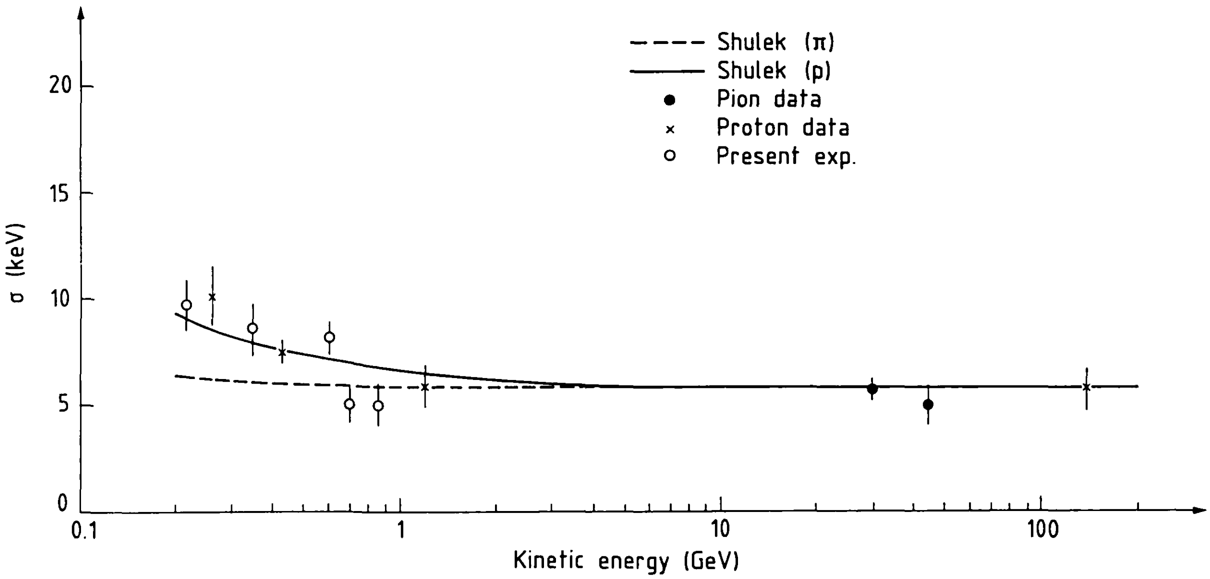

fig. 2. Determined values of σ. The continuous and broken lines are the Shulek et al. predictions for protons and pions respectively, computed from eq. (3). The pion (●) and proton (×) data are from [3]. The proton (○) data are the present experiment.

density convoluted with a Gaussian, eq. (4), with free parameters σ, ξ and ϵ_{mp}. The details of the fitting procedure and examples of energy-loss spectra have been given elsewhere [3].

Some deviations from the model are observed, as expected, in the tail, due to the neglect of escaping δ rays and the effect of the maximum energy transfer to electrons, not taken into account by the Landau distribution. In order to avoid a possible bias in the fitted parameters, we have varied the upper limit to which each experimental distribution was fitted. The best fits had χ^2-probabilities of the order of 50% or better and were obtained by fitting up to $\epsilon_{max} = \epsilon_{mp} + \alpha W$, where W is the full width at half maximum and the values of α are between 1.5 and 2.5. However, the fitted values of σ, ξ and ϵ_{mp} determined at the best χ^2 did not differ, within the error of their determination, from those of the complete fit.

In fig. 1 the fitted values of the parameter ξ are shown. The continuous line is the calculated curve for incoming protons, in 300 μm of silicon. The agreement between experiment and eq. (1) seen in fig. 1 indicates that our calibration of the energy scale for the data is correct, in average, to within 4%.

Table 1 gives a list of the fitted values of ξ, σ and the most probable energy-loss of the Landau distribution, ϵ_{mp}. The observed values of ϵ_{mp} are in general agreement, within the experimental errors, with those calculated from eq. (7) following the Landau theory, provided the values of $\langle\epsilon\rangle$ are computed using the Bethe–Block formula given in eq. (6). The most probable energy-loss, E_{mp}, of the overall straggling distribution defined by eq. (2), is about 3% higher than ϵ_{mp} due to the folding of the Gaussian distribution (table 1).

In fig. 2, we show a plot of the values obtained for the parameter σ in this experiment and for protons and pions from [3]. The lines are the corresponding theoretical predictions made by Shulek et al. [eq. (3)]. The quoted errors take into account the uncertainty in determining the noise contribution to σ_t.

4. Multiparticle production

4.1. Experimental set-up

Multiparticle energy-loss measurements have been conducted in the H_3 beam of the CERN SPS using the experimental arrangement sketched in fig. 3. The intensity of the incoming beam was 2×10^4 p/burst at a momentum of 115 GeV/c.

The geometrical acceptance (see fig. 3) is defined by 16 mm diameter hole in a scintillator A (with an area of 40×40 cm^2) mounted 20 cm downstream from the 5 mm thick lead target. This scintillator is placed in anticoincidence with one upstream and two downstream ones, respectively S_1 and PM_1 and PM_2. The half-angle of the forward acceptance cone subtended by the hole is 2.3° at the center of the target. The three latter scintillators have an area of 1×1 cm^2. The restriction of our acceptance to a forward cone of 2.3° half-angle reduces the background of non-relativistic protons * to less than a few percent.

Two ion-implanted Si-detectors of active area 1×1

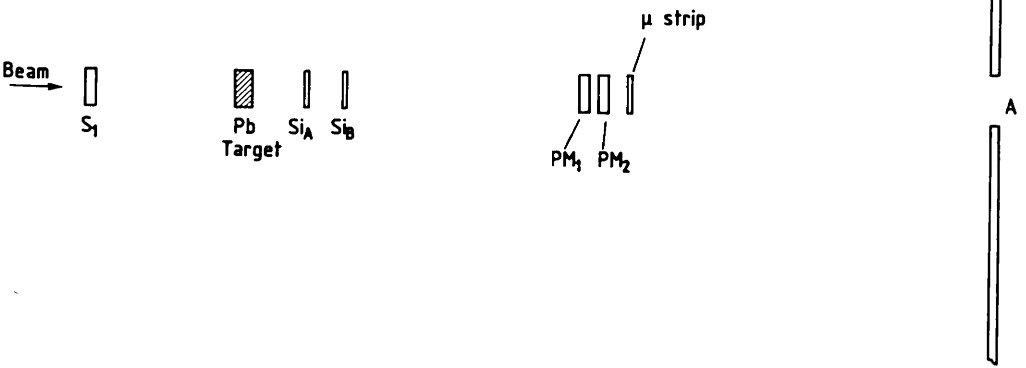

Fig. 3. Experimental lay-out for the multiparticle energy-loss measurements.

---

* The momentum range of slow protons is between 300 and 1000 MeV/c. They have a roughly flat angular distribution between 40° around the beam direction.

cm^2 and (300 ± 5) μm thickness, are located downstream from the target. Pulses from $\mathrm{Si_B}$ are accepted only when they correspond to energy-losses greater than the most probable energy-loss of a relativistic particle. A trigger defined by $\mathrm{T = S_1 \cdot PM_1 \cdot PM_2 \cdot Si_B \cdot \bar{A}}$ establishes that a beam particle enters the target and that at least one charged particle emerges in the very forward direction.

The microstrip detector is a 300 μm thick ion-implantation device with 50 strips of 200 μm pitch disposed horizontally, with an active area 1 × 3 cm^2. The multiplicity of an interaction is found by examining the height of the pulse formed by linearly summing the discriminated signals from all the strips of the microstrip detector. An output pulse, M, is produced when the input pulse height corresponds to a multiplicity lower than four. Hence T · M allows to trigger on an event in which up to three secondary particles traverse the silicon detector $\mathrm{Si_A}$. The energy-loss in the detector is recorded at different multiplicities by a 2249 A Lecroy ADC using such a trigger. The special purpose electronics associated with $\mathrm{Si_A}$ and $\mathrm{Si_B}$ have been described in [3].

The above trigger can select interactions where two or three particles are produced in forward direction. However the single beam particle can give a trigger, provided that its energy-loss is sufficiently large in $\mathrm{Si_B}$. In this way the parameters of the single particle, for eq. (9), can be fitted in the same data sample containing energy loss from two and three relativistic particles. A contamination from four- and even five-particle production is expected due to the finite 200 μm resolving distance for two particles in the microstrip detector and to a few unconnected strips.

4.2. Data analysis

Data samples were taken by using the trigger described above. The percentage of triggers due to beam particles could be modified by varying the threshold of the discriminator connected to the detector $\mathrm{Si_B}$.

The energy-loss spectra were fitted to a function

$$L(\epsilon) = \sum_{n=1,5} P(n) \Lambda(\epsilon, n), \qquad (10)$$

where $P(n)$ is the percentage of events in which n relativistic particles traverse the silicon detector $\mathrm{Si_A}$. The free parameters of the fit are $P(n)$ $[n = 1 \cdots 5]$ σ and ξ *. the value of ϵ_{mp} ** for a single relativistic particle has been assumed to be 84 keV [3]. The Gaussian noise contribution was measured before, during and after the data taking. Its value was found to be 4.3 ± 0.2 keV.

The large amount (between 12000 and 32000 pulse heights per data sample) and high resolution of data provide a very sensitive test of the energy-loss model, but also require considerable care in the fitting procedure in order not to introduce numerical and statistical biases. The details of how we detected and eliminated these biases are given in ref. 3, where the same fitting procedures were used. The entire fitting procedure has been tested by generating Monte Carlo data with known parameter values and fitting it through the same procedures. Good fits were obtained for all data samples.

Table 2 gives the fitted values of the parameters $P(n)$ $[n = 1 \cdots 5]$ ξ and σ for the three data samples with different thresholds of $\mathrm{Si_B}$. The three energy-loss spectra detected by the $\mathrm{Si_A}$ detector are shown in figs. 4(a), (b) and (c) respectively. The energy-loss distributions have been fitted between 60 and 500 keV. The χ^2-probabilities associated with the fits varied between 45 and 85%. The determined values of ξ and σ do not have any systematic dependence on the set of the $P(n)$ values. This is the expected behaviour when both the fitting procedure is correct and the energy-loss distribution is properly taken into account. The expected values for ξ [from eq. (1)] and σ [from eq. (3)] are 5.35 and 5.76 keV respectively and are in agreement with the fitted ones within the errors, although the fitted values of ξ seem to be systematically higher. For the different data samples, $P(n = 1)$ varied between 0.08 and 0.52.

When the data were fitted over a range from 50 to 400 keV, only a slight variation of the values of the fitted parameters ξ and σ was observed. In particular the parameter ξ was systematically lowered. However the χ^2-probabilities never exceeded 15% in this case.

---

* As already discussed in sect. 2, the parameters σ and ξ are those of the single relativistic particle.

** The relationship between $\epsilon_{n,\mathrm{mp}}$ (i.e. the most probable energy-loss of the Landau distribution for n-relativistic particles) and ϵ_{mp} is discussed in sect. 2.

Table 2
Fitted values of $P(n)$, ξ and σ

	$P(1)$ [%]	$P(2)$ [%]	$P(3)$ [%]	$P(4)$ [%]	$P(5)$ [%]	ξ [keV]	σ [keV]
a)	52.2 ± 0.6	13.5 ± 0.4	25.5 ± 0.6	7.8 ± 0.5	1.0 ± 0.4	5.9 ± 0.4	4.9 ± 0.6
b)	40.9 ± 0.5	18.6 ± 0.5	30.5 ± 0.6	8.7 ± 0.6	0.8 ± 0.5	6.1 ± 0.6	6.6 ± 1.7
c)	7.6 ± 0.4	25.2 ± 0.8	49.3 ± 1.3	15.6 ± 1.1	2.3 ± 0.9	6.2 ± 0.5	6.6 ± 1.2

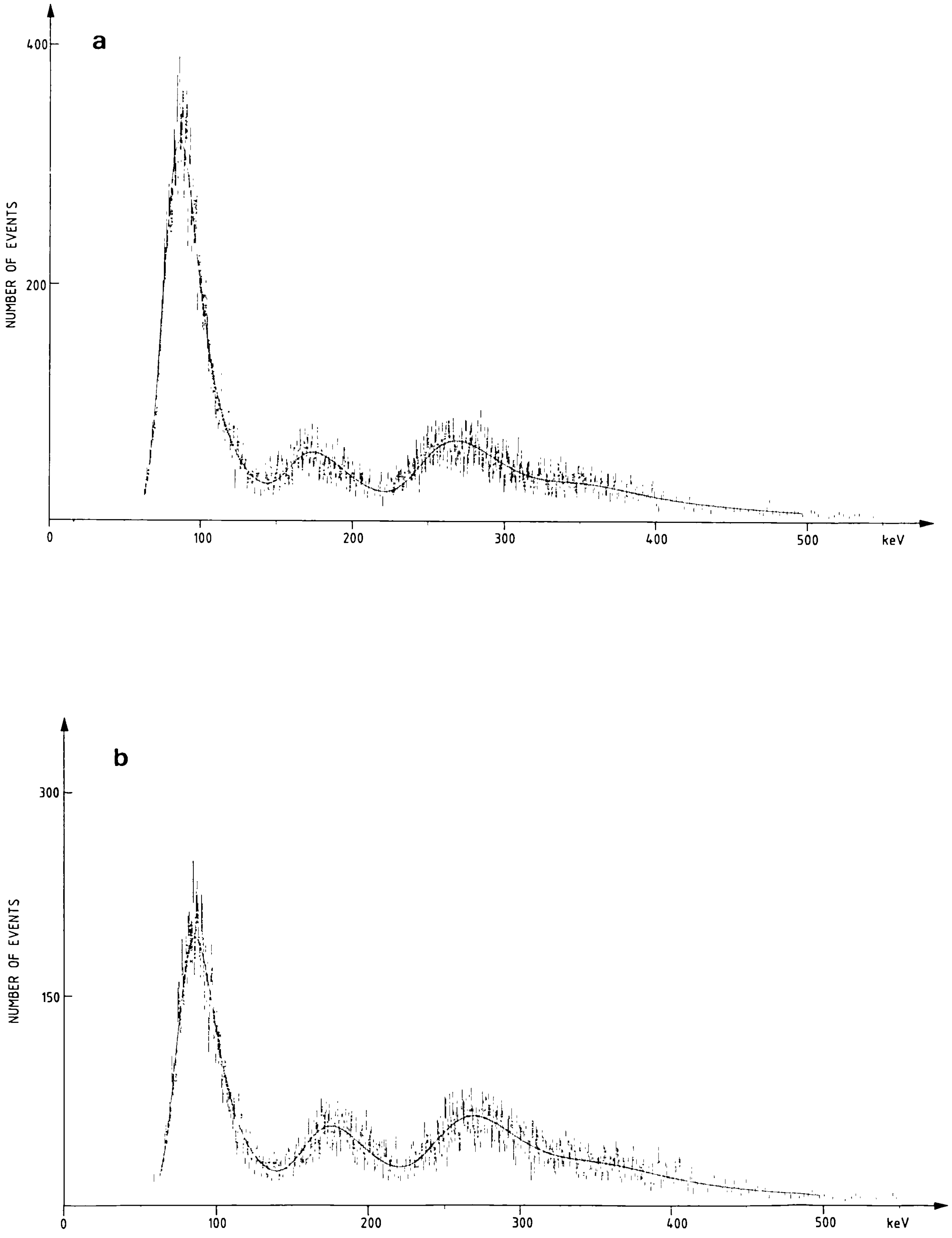
a
NUMBER OF EVENTS
400
200
0
100
200
300
400
500
keV
b
NUMBER OF EVENTS
300
150
0
100
200
300
400
500
keV

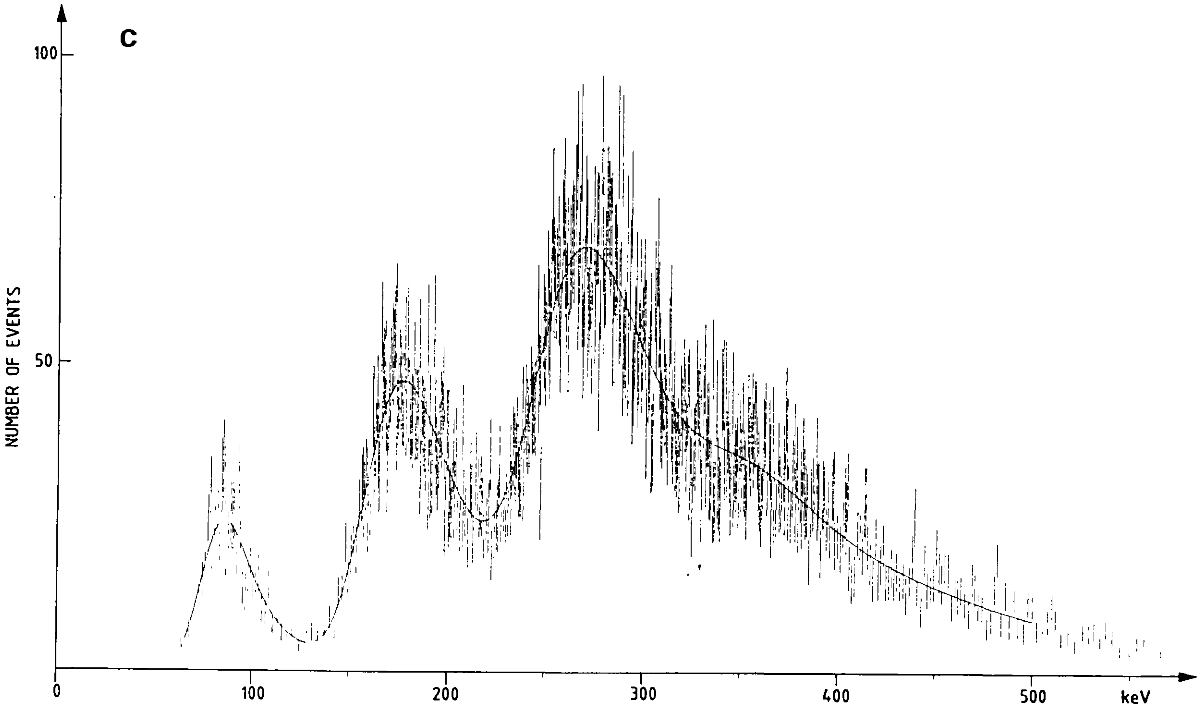

Fig. 4. Energy-loss spectra including both single and several relativistic particles. The percentages, $P(n)$, of the number of particles produced in part a), b) and c) are listed in table 2. The continuous lines are the fitted curves.

5. Conclusion

The fitted values of the parameter σ for incoming proton kinetic energies between 220 and 850 MeV agree with those found in a previous experiment in the same energy range [3]. Thus they confirm that the collision-loss theories of Landau and Vavilov have to be modified to take into account the atomic binding of electrons. For a single charged particle this effect seems to be properly accounted for by eq. (2), provided that σ is computed by the Shulek et al. formula [eq. (3)].

The energy-loss spectrum of n-relativistic and spatially separated particles, traversing a silicon detector of thickness $x = 0.03$ cm, is well described by the improved energy-loss distribution. The parameters $\epsilon_{n,\mathrm{mp}}$, ξ_n and σ_n agree with those computed by scaling the parameters of a single relativistic particle traversing a thickness nx [i.e. eq. (9)], although the fitted values of ξ here are systematically ($\approx 10\%$) higher than those obtained in the single particle data of ref. 3. This may be explained partly by uncertainties in calibration (evaluated at $\approx 6\%$ in ref. [3]), and partly by contamination of non-relativistic particles in the data samples (which causes a broadening of the spectra).

References

[1] L. Landau, J. of Phys. (U.S.S.R.) 8 (1944) 201.
[2] P.V. Vavilov, Soviet. Phys. JETP 5 (1957) 749.
[3] S. Hancock, F. James, J. Movchet, P.G. Rancoita and L. Van Rossum, Phys. Rev. A28 (1983) 615.
[4] D.W. Aitken, W.L. Lakin and H.R. Zulliger, Phys. Rev. 179 (1969) 393.
[5] U. Fano, Ann. Rev. Nucl. Sci. 13 (1963) 1.
[6] Methods of Experimental Physics, Vol 5A eds., C.L. Yuan and C.-S. Wu (Academic Press, New-York and London, 1961) ch. 1.
[7] O. Blunck and S. Leisegang, Zeit, Phys. 128 (1950) 500.
[8] P. Shulek, B.M. Golovin, L.A. Kulyukina, S.V. Medved and P. Pavlovich, Soviet J. Nucl. Phys. 4 (1967) 400.
[9] R.M. Sternheimer, Phys. Rev. 145 (1966) 247.
[10] W. Boersch-Supan, J. Res. Natl. Bur. Stand, 65B (1961) 245.
[11] K.S. Kolbig and B. Schorr, Asymptotic expansion for the Landau density and distribution functions, CERN/DD/83/5 29.3.83.
[12] V.C. Ermilova, L.P. Kotenko and G.I. Merzon, Nucl. Instr. and Meth. 145 (1977) 555.
[13] M.C. Walske, Phys. Rev. 88 (1952) 1283.
[14] M.C. Walske, Phys. Rev. 101 (1956) 940.
[15] R.M. Sternheimer, Phys. Rev. B3 (1971) 3681.
[16] R.M. Sternheimer, Phys. Rev. 117 (1960) 485.

PHYSICAL REVIEW A VOLUME 28, NUMBER 2 AUGUST 1983

Energy loss and energy straggling of protons and pions in the momentum range 0.7 to 115 GeV/c

S. Hancock
Imperial College of Science and Technology, South Kensington, London SW7 2AZ, United Kingdom

F. James
European Organization for Nuclear Research (CERN), CH-1211 Geneva 23, Switzerland

J. Movchet, P. G. Rancoita,* and L. VanRossum
Centre d'Etudes Nucléaires de Saclay, F-91190 Gif-sur-Yvette, France

(Received 21 July 1982)

The energy-loss distribution for pions and protons, with momenta between 0.7 and 115 GeV/c, has been measured in an ion-implanted silicon detector of 300 μm thickness. The data are well described by an empirical energy-loss distribution.

I. INTRODUCTION

The detection of charged particles by measuring their energy loss in thin silicon detectors has led to widespread study of the corresponding energy-loss spectrum.[1–3] This spectrum is given, to a first approximation, by the Landau[4] and Vavilov[5] theories, which are based on Rutherford scattering on free electrons.

In order to achieve high spatial resolution and to detect change in charged multiplicity due to decay of short-lived particles,[6,7] very thin (<300 μm) silicon detectors and low-noise electronics are used. Under these conditions, significant deviations from the Landau-Vavilov theory are expected because of the importance of the interactions where the atomic electron binding energy cannot be neglected.[8–10] This deviation has been observed, but not explained[11] for relativistic pions with momenta greater than 6 GeV/c.

The purpose of this experiment is to measure the energy-loss spectra of pions and protons over a large momentum range in a very thin silicon detector (300 μm), using low-noise ($\sigma \approx 4$ keV) electronics.

II. ENERGY STRAGGLING

The statistical nature of the ionization process during the passage of a fast charged particle through matter results in large fluctuations of the energy loss in absorbers which are thin compared with the particle range. The calculation of these fluctuations was first performed by Landau.[4] Subsequently Vavilov[5] refined the Landau solution to the problem by introducing the maximum allowable energy transfer in the Rutherford macroscopic cross section $\omega'(\epsilon)$:

$$\omega'(\epsilon)=\begin{cases}(\xi/\epsilon^2)(1-\beta^2\epsilon/\epsilon_m), & 0<\epsilon<\epsilon_m\\ 0, & \epsilon>\epsilon_m\end{cases} \tag{1}$$

where ϵ_m (Ref. 12) is the maximum amount of energy that can be transferred to an atomic electron in a single collision with the incident particle of mass m and velocity βc, and where ϵ is the actual energy transferred in the collision (Landau neglected the term $\beta^2\epsilon/\epsilon_m$).

The quantity ξ is given, in keV, by

$$\xi=(2\pi z^2 e^4/m_e c^2\beta^2)NZx\rho/A$$
$$=153.4(z^2/\beta^2)(Z/A)x\rho\ , \tag{2}$$

where N is the Avogadro number, m_e and e are the electron mass and charge, respectively, z is the charge of the incident particle, Z, A, and ρ are the atomic number, atomic weight, and density (g/cm^3) of the material, and where x is the distance in cm traversed through the material.

However, the effects of atomic binding of the electrons have been disregarded in both the Landau and Vavilov theories. The theories can be improved by using a modified cross section to take into account the electron binding energy.[13] The modified energy-loss distributions can be expressed as the convolution of a Gaussian function with a Landau or Vavilov distribution, respectively.[8,10,14] Thus

$$f(\Delta,x)=(1/\sigma\sqrt{2\pi})\int_{-\infty}^{+\infty}f_{L,V}(\Delta',x)\times\exp[-(\Delta-\Delta')^2/2\sigma^2]d\Delta'\ , \tag{3}$$

where $f_{L,V}(\Delta',x)$ is either the Landau or the Vavilov distribution and Δ is the actual energy loss.

The term $\delta_2=\sigma^2$ in Eq. (3) has been computed by Shulek *et al.*, who derived the following equation:

$$\delta_2=\tfrac{8}{3}\xi\sum_i l_i(Z_i/Z)\ln(2m_e c^2\beta^2/l_i)\ , \tag{4}$$

where Z_i is the number of electrons in the ith shell of the stopping material, l_i is the ionization potential of the ith shell, and the summation is performed over the shells for which $l_i<2m_e c^2\beta^2$. These ionization potentials have been computed by Sternheimer[15–17] and enter into the density effect correction to the mean energy loss. Only the tails of the actually measured spectra are expected to differ systematically from those given by Eq. (3), because δ rays produced in high-energy transfer interactions may escape from the detector.

III. EXPERIMENTAL METHOD

In the present investigation, energy loss has been measured for pions and protons in the momentum range between 0.7 and 115 GeV/c (see Table I). The momentum

TABLE I. Momentum spread of the beam either at the Centre d'Etudes Nucléaires de Saclay or at CERN.

Momentum (GeV/c)	Particle	$\Delta P/P$ (%)	Laboratory
0.736	p	$< \pm 0.1$	Saturne II-Saclay
1.000	p	$< \pm 0.1$	Saturne II-Saclay
1.916	p	$< \pm 0.1$	Saturne II-Saclay
30.0	π ($>95\%$)	$< \pm 1.0$	CERN-SPS
45.0	π ($>95\%$)	$< \pm 1.0$	CERN-SPS
115.0	p ($>95\%$)	$< \pm 1.0$	CERN-SPS

spread $\Delta P/P$ was never more than 0.1% for the measurements performed at Saturne in Saclay, and never more than 1% at the CERN Super Proton Synchrotron (SPS). A well-defined momentum is important, particularly at low values, since any momentum spread broadens the energy-loss distribution and thereby masks the effect due to long-distance collisions.

Two Enertec ion-implanted passivated-silicon junction detectors with an active area of 1.0 cm^2 and a thickness of 300 ± 5 μm were used.[18] Total depletion of the detectors was achieved at reverse biases of about 100 V. The initial leakage currents were 16 and 20 nA.

The signal pulses from these detectors were sent to standard ORTEC-125 charge preamplifiers. The preamplified signals were then sent to a modified version of an ORTEC-472 spectroscopy amplifier, in the case of the more upstream of the two detectors, and to an EG&G-474 timing filter amplifier, in the case of the downstream detector. The ORTEC amplifier produced an output pulse with a 600-nsec base and a 200-nsec rise time, while the timing filter amplifier produced a pulse with a 100-nsec base and a 50-nsec rise time. The instantaneous counting rate never exceeded 3000 events per second in order to avoid pile up.

The spacing between the two detectors was 4 cm, with their active areas well aligned. A scintillator with an area of 0.5×0.5 cm^2 and a thickness of 0.5 cm was positioned 1 cm from the downstream detector. The beam was defined by the coincidence of the downstream detector and this small scintillator, the latter generating a jitter of only a few nsec. This beam-particle trigger was shaped to provide a 40-nsec gate for a LeCroy 2249A analog-to-digital converter (ADC), where the pulse coming from the upstream detector was recorded.

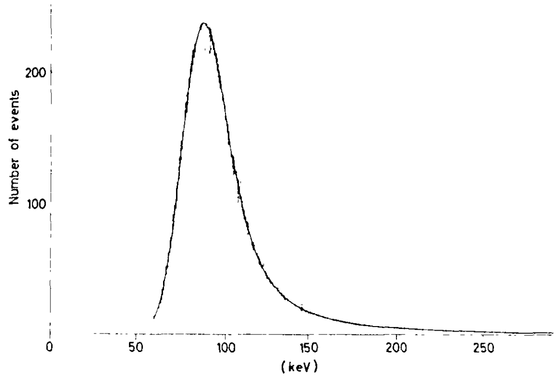

FIG. 1. Energy-loss spectrum for β^- coming from a Ru source. Kinetic energies are selected to be greater than 1 MeV. Continuous line represents the fitted Landau distribution convolved by a Gaussian function.

The upstream detector, together with its special purpose electronics, had a Gaussian noise distribution with an independently measured standard deviation σ_{noise}, whose typical value was 4.0 ± 0.4 keV. The exact value was determined separately before each data taking.

The initial calibration of the energy scale for the entire system was performed using a 30-GeV π^- beam. The most probable energy loss for pions has no significant momentum dependence for $\beta\gamma > 50$.[11] We assumed a value of 84.0 ± 2.8 keV for the most-probable energy loss (Δ_{mp} defined in Sec. IV) in 300 μm of silicon.[19] Thereafter a Ru β^- source has been used for calibration purposes once it had been determined that the value of Δ_{mp} for relativistic electrons is 86.8 ± 2.8 keV on the same scale that yields the canonical value of 84.0 ± 2.8 keV for relativistic pions.

The source was placed in front of the upstream detector and a trigger formed for electrons crossing both of the detectors and the scintillator. This way only relativistic electrons, namely, those with a kinetic energy between about 1 and 3 MeV were selected. Figure 1 shows the resulting energy-loss spectrum and the corresponding fitted curve. This calibration was performed after each measurement at a new beam momentum in order to monitor very closely the stability of the electronics.

IV. DATA ANALYSIS AND DISCUSSION

In the limit as $k=\xi/\epsilon_m\rightarrow0$, the Vavilov distribution approaches that of Landau theory. It has been shown[1] that for $k\approx0.06$ (corresponding to 65.3-MeV positive pions crossing a 0.216-cm-thick lithium-drifted silicon detector), the Vavilov and Landau spectra are practically indistinguishable.

The lowest momentum used in our investigation corresponds to $k\approx0.02$. Consequently, the observed spectra are expected to be well represented by Eq. (3), in which a Gaussian function convolves a Landau distribution. The standard deviation σ_{tot} of the Gaussian part can be defined to also take into account the detector and electronic noise with

$$\sigma_{\text{tot}}=(\delta_2+\sigma_{\text{noise}}^2)^{1/2}\ ,$$

where σ_{noise} is the standard deviation of the Gaussian noise distribution (see Sec. III).

The Landau probability density function is given by

$$f_L(\Delta,x)=(1/\xi)\phi(\lambda)\ ,$$

$$\phi(\lambda)=(1/2\pi i)\int_{c-i\infty}^{c+i\infty}\exp(u+\ln u+\lambda u)du\ ,$$

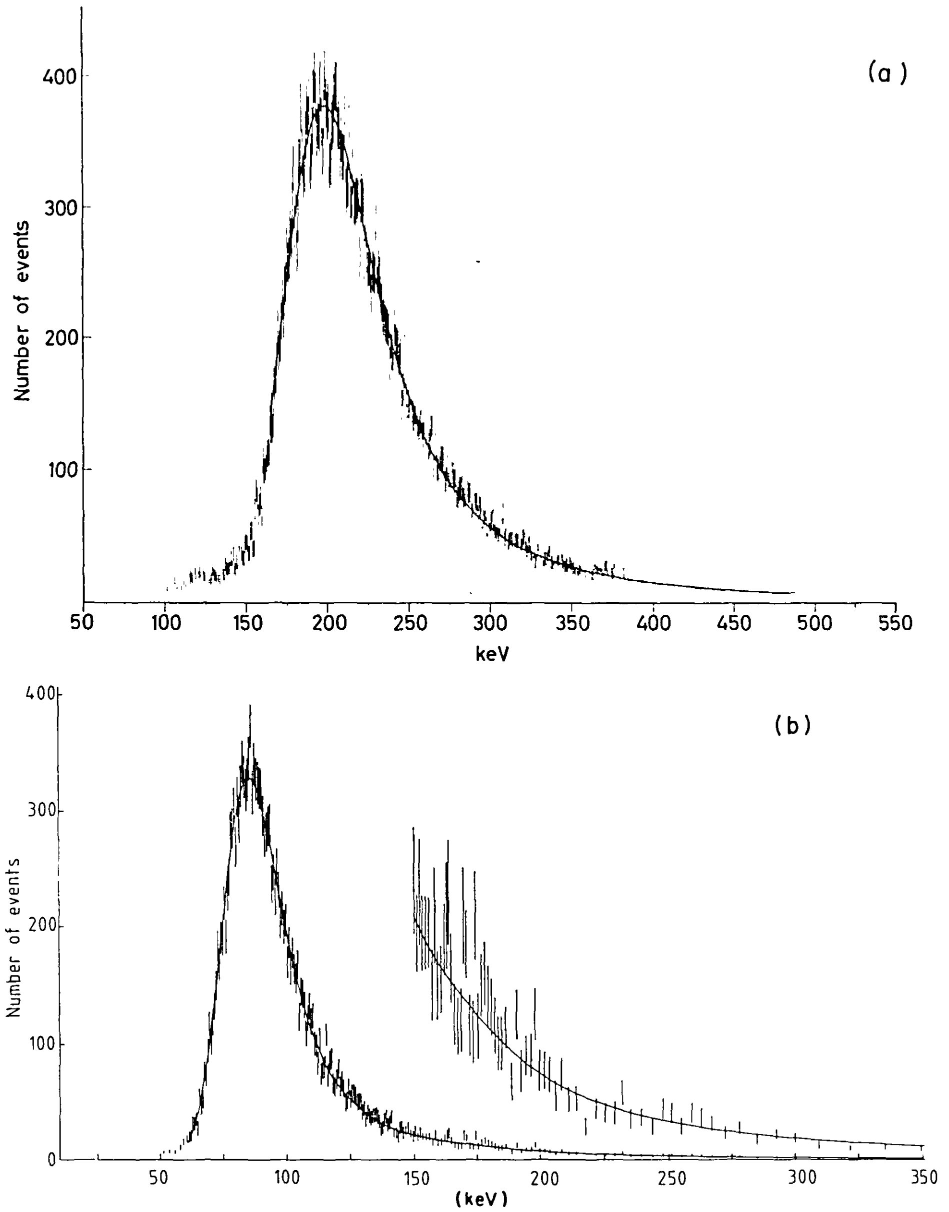

FIG. 2. (a) and (b) show the energy-loss spectra at 0.736 and 115 GeV/c of incoming proton momenta, respectively. Continuous curves are the complete fits to the experimental data. Values of ξ are 14.9 ± 0.8 and 5.5 ± 0.3, respectively (the corresponding values of the best fit are 15.0 ± 0.8 and 5.6 ± 0.3). Values of $\sigma=\sqrt{\delta_2}$ are 11.3 ± 1.4 and 5.5 ± 1.1, respectively (the corresponding values of the best fit are 10.2 ± 1.3 and 5.7 ± 1.1). In (b) the tail is also shown with the vertical scale multiplied by ten.

where

$$\lambda=(\Delta-\langle\Delta\rangle)/\xi-1-\beta^2+C-\ln(\xi/\epsilon_m)$$
$$=[\Delta-(\Delta_{\text{mp}}-\xi\lambda_0)]/\xi\ ,$$

$\langle\Delta\rangle$ is the mean energy loss, the Euler constant $C\approx0.577215$, $\lambda_0\approx-0.225$ is the value for which ϕ is a maximum, Δ_{mp} is the most-probable energy loss of the Landau distribution, i.e., $f_L(\Delta_{\text{mp}},x)=(1/\xi)\phi(\lambda_0)$, and where c is an arbitrary real positive constant.

The experimental energy-loss distributions for each momentum and type of particle were fitted to the Landau probability density convolved with a Gaussian as described above, with free parameters δ_2, ξ, and Δ_{mp}. The fitting procedure is described in the Appendix to this paper. The good fits obtained for all the data samples give us confidence in the overall appropriateness of Eq. (3) and in the values of the fitted parameters. However, some deviation from the model is observed, as expected, in the tail due mainly to the neglect of escaping δ rays. In order to avoid a possible bias in the fitted parameters, we have varied the upper limit to which each experimental distribution was fitted. The best fits had χ^2 probabilities of the order of 50% or better and were obtained by fitting up to $\Delta_{\max}=\Delta_{\text{mp}}+\alpha W$, where W is the full width at half maximum, and the values of α are between 2.5 and 3.5. However, the fitted values of δ_2, ξ, and Δ_{mp} determined at the best χ^2 did not differ, within the error of their determination, from those of the complete fit.

In Fig. 2 the energy-loss distributions for the lowest and highest proton momenta are shown. The continuous curves are the least-squares fits, with all of the tail fitted. The curves obtained by using the parameters at the best χ^2

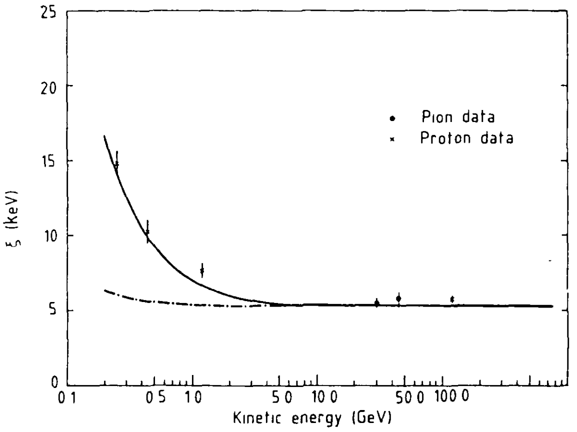

FIG. 3. Determined values of the parameter ξ. Continuous and broken curves are computed from Eq. (2) for proton and pion, respectively. General agreement between the fitted value and the predicted one indicates that both the energy calibration had been correctly performed and that the shape of the energy-straggling spectrum is well represented by the improved energy-loss distribution.

are, by eye, indistinguishable from those given in Fig. 2. In Fig. 3 the fitted values of the parameter ξ are shown. The continuous and broken lines are the calculated curves for incoming protons and pions, respectively, in 300 μm of silicon. The agreement between experiment and Eq. (2) seen in Fig. 3 indicates that our calibration of the energy scale for the data is correct to within 6%.

Table II gives a list of the fitted values of ξ, $\sigma=\sqrt{\delta_2}$, and the most-probable energy loss of the Landau distribution Δ_{mp}. The observed values of Δ_{mp} are in general agreement, within the experimental errors, with Landau theory provided $\langle \Delta \rangle$ are computed using the Bethe-Bloch formula and taking into account the correction for the density effect. The shell correction term of the Bethe-Bloch formula is negligible over the momentum range of the present investigation.[20-22] The most-probable energy loss E_{mp} of the overall straggling distribution defined by Eq. (3), is about 3% higher than Δ_{mp} due to the folding of the Gaussian distribution (Table II). There is no significant difference between E_{mp} for π^- at a momentum of 45 GeV/c ($\beta\gamma \approx 330$) and protons at 115 GeV/c ($\beta\gamma \approx 123$). Esbensen *et al.*[11] have already shown that there is no relativistic rise of the most-probable energy loss for $50<\beta\gamma<120$. The value of E_{mp} determined at the lowest momentum is in agreement with the value quoted by Aitken *et al.*,[1] once it is extrapolated to a detector thickness of 0.216 cm.

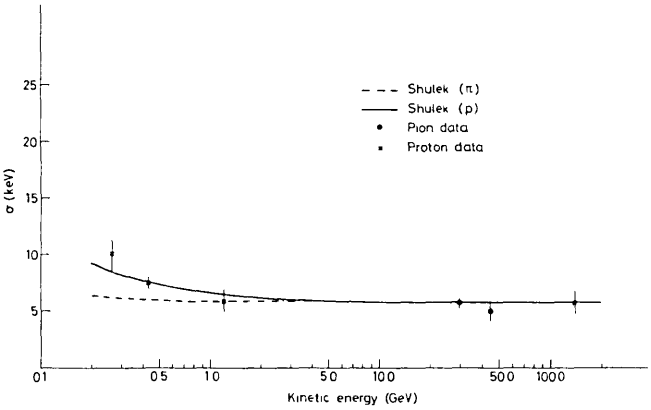

FIG. 4. Determined values of $\sigma=\sqrt{\delta_2}$. Continuous and broken lines are the Shulek *et al.* (Ref. 9) predictions for protons and pions, respectively. Pion (●) and proton (×) data are in general agreement with the Shulek *et al.* predictions.

In Fig. 4 we show a plot of the values obtained for the parameter $\sigma=\sqrt{\delta_2}$ together with the corresponding theoretical predictions made by Shulek *et al.* for protons and pions, respectively (see Sec. II). The quoted errors take into account the uncertainty in determining the noise contribution to σ_{tot} (see the Appendix). Both the pion and proton data seem to be in general agreement with the model of Shulek *et al.* As $\beta \to 1$, σ becomes a constant to within the error of its determination.

The results of the present investigation confirm the collision-loss theories of Landau and Vavilov. The effect of atomic binding of electrons has been clearly observed and seems to be well described by Eq. (3), and the standard deviation of the Gaussian contribution is compatible with the computations of Shulek *et al.*

ACKNOWLEDGMENTS

The authors wish to thank A. Penzo and the staff of Saturne II accelerator for their collaboration. Useful discussions with M. Saudinos, D. Treille, P. Borgeaud, and P. Bonamy are gratefully acknowledged. We are indebted to A. Seidman for reading the manuscript. Precise values of the Landau distribution were supplied by B. Schorr.

TABLE II. Values of ξ, $\sigma=\sqrt{\delta_2}$, Δ_{mp}, and E_{mp} vs the incoming momentum.

Momentum (GeV/c)	ξ (keV)	$\sigma=(\delta_2)^{1/2}$ (keV)	Δ_{mp} (keV)	E_{mp} (keV)
0.736	15.0±0.8	10.2±1.3	194.8±5.8	196.2±5.8
1.000	10.4±0.8	7.4±0.6	127.5±3.8	130.8±3.8
1.916	7.6±0.4	5.9±1.0	94.0±3.0	97.2±3.0
30.0	5.5±0.3	5.7±0.5	84.0±2.8	85.6±2.8
45.0	5.8±0.4	5.0±0.9	86.0±2.8	88.8±2.8
115.0	5.6±0.3	5.7±1.0	83.2±2.8	85.5±2.8

APPENDIX: FITTING PROCEDURE

The large amount (between 20000 and 30000 pulse heights per data sample) and high resolution of data provide a very sensitive test of the energy-loss model, but also require considerable care in the fitting procedure in order not to introduce numerical and statistical bias.

The parameter fitting and goodness-of-fit testing were done with the usual least-squares techniques. The function minimized was

$$\chi^2(\alpha)=\sum_i \{[t_i(\alpha)-n_i]^2/d_i^2\} , \tag{A1}$$

where α are the free parameters of the fit, namely, ξ, δ_2, and Δ_{mp}, and a normalization factor; the sum is over all histogram bins, $t_i(\alpha)$ and n_i are, respectively, the expected and observed numbers of counts in the ith bin, and d_i is the standard deviation of the numerator. The histogram bins were constructed as follows: starting from the raw data histogram (ADC channels of a width of about 0.5 keV), bins with less than a minimum number of events were joined with neighboring bins until each new bin contained at least that minimum number [the resulting unequal bin widths in the tail are clearly visible in Fig. 2(b)]. The minimum bin content could be varied to make sure that it was large enough not to influence the fit, and the value finally used was 20.

The expected number of events in the ith bin $t_i(\alpha)$ is just the integral of Eq. (3), properly normalized, over the bin. It is customary to approximate this by the value of the function at the center of the bin, multiplied by the bin width. We have used both methods and find no significant difference (due to the extremely narrow bins in the peak region).

As the universal Landau function is evaluated very often during the fitting, a special subroutine was prepared which calculated this function using four-point interpolation in a table of 200 very accurate values calculated by Fourier series and checked against both published values[23,24] and those calculated by contour integration. The convolution with the Gaussian was done numerically using usually 20 points to evaluate the convolution integral for each data bin, but his number could be varied to make sure that it was large enough not to influence the fit.

The variance d_i^2 is usually taken as the observed number of events n_i, since this is indeed the variance of a Poisson distribution of mean n_i. However, under the null hypothesis, the expected value is $t_i(\alpha)$, not n_i. We find significant (although small) differences between fits done using the two techniques. An intermediate method is to use the average number of events observed over three bins, which gives essentially the same fits as using the expected number of events. This intermediate method has the advantage that the denominator in each term is constant (independent of the fit parameters) so there is no tendency to try to reduce the χ^2 by making the variances larger.

Finally, the entire fitting procedure has been tested by generating Monte Carlo data with known parameter values and fitting it through the same procedures. In order to do this we have developed a very accurate Landau-distributed random number generator [this generator, as well as our Landau density function, are available from the CERN Program Library as GENLAN (G903) and FUNLAN (G112)]. The Monte Carlo procedure helped us to choose the best fitting procedure and verified that our method did not introduce any significant bias in the fitted parameter values. The parameter errors given in Table II result from combining the statistical error calculated from our fits with a systematic error, largely calibration uncertainty (which is the dominant one) and the error in measuring σ_{noise}.

Good fits were obtained for all data samples, apart from a slight depression of the tail for reasons described above. The data taken at the SPS energies (see Table I) required adding about 1% contamination from two particles simultaneously traversing the silicon, which is consistent with the expected interaction probability in the upstream beam-defining scintillators. The effect is included in the curve shown in Fig. 2(b), but the resulting contribution (between 150 and 250 keV) is too small to be noticed by the eye. Two-particle contamination was neither expected nor observed for the other data.

---

[*] On leave from Istituto Nazionale di Fisica Nucleare, Milano, Italy.

[1] D. W. Aitken, W. L. Lakin, and H. R. Zulliger, Phys. Rev. 179, 393 (1969).

[2] E. M. Bellamy, R. Hofstadter, and L. Lakin, Phys. Rev. 164, 417 (1967).

[3] H. D. Maccabee, M. R. Raju, and C. A. Tobias, Phys. Rev. 165, 469 (1968). The thinner detector used in this experiment was 0.108 g/cm^3 Si. However, their quoted Gaussian resolution had $\sigma\approx 15$ keV (to be compared with 4.0±0.4 keV of the present investigation).

[4] L. Landau, J. Phys. (Moscow) 8, 201 (1944).

[5] P. V. Vavilov, Zh. Eksp. Teor, Fiz. 32, 920 (1957) [Sov. Phys.—JETP 5, 749 (1957)].

[6] E. Albini *et al.*, Phys. Lett. 110B, 339 (1982).

[7] P. G. Rancoita, European Organization for Nuclear Research Report No. CERN-NA14/81/31 (unpublished).

[8] O. Blunck and S. Leisegang, Z. Phys. 128, 500 (1950).

[9] P. Shulek, B. M. Golovin, L. A. Kulyukina, S. V. Medved', and P. Pavlovich, Yad. Fiz. 4, 564 (1966) [Sov. J. Nucl. Phys. 4, 400 (1967)].

[10] U. Fano, Annu. Rev. Nucl. Sci. 13, 201 (1963).

[11] H. Esbensen *et al.*, Phys. Rev. B 18, 1039 (1978).

[12] ϵ_m is given by

$$\epsilon_m=2m_ec^2\beta^2\gamma^2[1+(2\gamma m_e/m)+(m_e/m)^2]^{-1} .$$

[13] The Landau theory was first improved by Blunck and Leisegang (Ref. 8). Shulek *et al.*[9] have used the same approach to modify the Vavilov function.

[14] H. Bichsel and P. Saxon, Phys. Rev. A 11, 1286 (1975).

[15] R. M. Sternheimer, Phys. Rev. 145, 247 (1966).

[16] R. M. Sternheimer, Phys. Rev. B 3, 3681 (1971).

[17] R. M. Sternheimer, Phys. Rev. 117, 484 (1960).

[18] Detectors of this type, intended for operation at room temperature, are made of n-type silicon of 3200 Ω cm resistivity.

[19] J. Bak (private communication). In an extension of the experiment described in Ref. 11, the peak position of a relativistic particle crossing a 300-μm silicon detector has been observed

to be in agreement with the value of ~83.75 keV for the most-probable energy loss of the Landau distribution. The accuracy of the measurement was estimated to be of the order of 3%.

[20] *Methods of Experimental Physics Vol. 5A,* edited by C. L. Yuan and C.-S. Wu (Academic, New York and London, 1961), Chap. 1.

[21] M. C. Walske, Phys. Rev. 88, 1283 (1952).

[22] M. C. Walske, Phys. Rev. 101, 940 (1956).

[23] B. Schörr, Comput. Phys. Commun. 7, 215 (1974).

[24] W. Börsch-Supan, J. Res. Natl. Bur. Stand. Sect. B 65, 245 (1961).